

INFORMATION TO USERS

This manuscript has been reproduced from the microfilm master. UMI films the text directly from the original or copy submitted. Thus, some thesis and dissertation copies are in typewriter face, while others may be from any type of computer printer.

The quality of this reproduction is dependent upon the quality of the copy submitted. Broken or indistinct print, colored or poor quality illustrations and photographs, print bleedthrough, substandard margins, and improper alignment can adversely affect reproduction.

In the unlikely event that the author did not send UMI a complete manuscript and there are missing pages, these will be noted. Also, if unauthorized copyright material had to be removed, a note will indicate the deletion.

Oversize materials (e.g., maps, drawings, charts) are reproduced by sectioning the original, beginning at the upper left-hand corner and continuing from left to right in equal sections with small overlaps. Each original is also photographed in one exposure and is included in reduced form at the back of the book.

Photographs included in the original manuscript have been reproduced xerographically in this copy. Higher quality 6" x 9" black and white photographic prints are available for any photographs or illustrations appearing in this copy for an additional charge. Contact UMI directly to order.

UMI

A Bell & Howell Information Company
300 North Zeeb Road, Ann Arbor, MI 48106-1346 USA
313/761-4700 800/521-0600



Real-Time Feedback for Etch Rate and Sidewall Profile Control in Reactive Ion Etching

by

Brian Andrew Rashap

A dissertation submitted in partial fulfillment
of the requirements for the degree of
Doctor of Philosophy
(Electrical Engineering: Systems)
in The University of Michigan
1995

Doctoral Committee:

Associate Professor James S. Freudenberg, Chair
Professor Jessy W. Grizzle
Professor Pramod P. Khargonekar
Associate Professor Fred L. Terry, Jr.
Research Scientist Michael E. Elta

UMI Number: 9610223

**UMI Microform 9610223
Copyright 1996, by UMI Company. All rights reserved.**

**This microform edition is protected against unauthorized
copying under Title 17, United States Code.**

UMI
300 North Zeeb Road
Ann Arbor, MI 48103



To my mother, father and brother
for their unconditional support of
all of my endeavors.

ACKNOWLEDGEMENTS

This dissertation would not have been possible without the assistance of many people.

I apologize in advance if I inadvertently forgot to mention anyone.

I would like to begin by thanking my advisor, Professor Jim Freudenberg. Jim was the perfect advisor for me, *i.e.*, most of the time he left me alone so that I could get work done, but he was always available when I needed his guidance. I am really going miss stopping by his office for our late night chats.

I would like to especially thank my dissertation committee: Professors Jessy Grizzle, Pramod Khargonekar, Fred Terry, and Dr. Michael Elta. I could not have asked for a better group of individuals to guide me over the years. They have been great teachers, both inside and outside of the class room, and great friends. I would also like to thank Dr. Martin Giles for his guidance in developing models and simulations for the etching process.

There are a number of people without whose help this research would not have been possible. I would like to thank Keith, Jim and Terry for all their assistance in wafer processing and equipment maintenance. I would especially like to thank Jeff for serving unofficially as my cleanroom mentor. Jeff has taught me most of what I know about running and maintaining semiconductor processing equipment. His guidance has been as valuable to me as that of my dissertation committee. I would also like to thank Don, Chuck, Hugh, Laura, Liz, and Jon for all they have done in maintaining the computers that I have

relied on during this research.

I have been very lucky to have the opportunity to work with a group of talented students during my years at the University of Michigan. I want to thank Courtney, Tyrone B., Tyrone V., Pete H., Pete K., Oliver, Anna, Meera, Manish, Steve T., Bill and Al for being great friends and research partners over the past few years. A special thanks to everyone who helped to proof read this dissertation. Your comments and suggestions have been invaluable. I wish you all the best of luck as you finish up your graduate studies.

One person who has made my last year here very special has been Steve R. I have really enjoyed teaching Steve many of the research skills that I have learned over the years. It makes it easier to leave knowing that I am leaving the Mule in such capable hands. I wish Steve all the best in continuing this research where I have left off.

I would like to thank the Semiconductor Research Corporation (SRC), the DeVlieg Foundation and the National Aeronautics and Space Administration (NASA) for the financial support that made my graduate education possible.

I would have not made it though 22 years of school without the love and support of my family. My mother and father have done so much for me, I wouldn't know where to begin to thank them. I love you both more than anything. Thanks for everything. I would also like to thank by brother whose love and support has always meant a lot to me. In addition, I would like to thank Mom and Dad O'Rourke for providing me with the love and support of a second family. And I can't begin to thank my wife, Krista, for everything that she has done for me. Her love and friendship have kept me going through the hardest of times.

The one person that I am going to miss most in leaving Michigan is Jon Friedman. Jon has been my best friend and so much more over the past 5 years. Michigan would just not have been the same without him.

TABLE OF CONTENTS

DEDICATION	ii
ACKNOWLEDGEMENTS	iii
LIST OF FIGURES	vii
LIST OF TABLES	x
LIST OF APPENDICES	xi
CHAPTERS	
1 Introduction	1
1.1 Microelectronic Fabrication	2
1.1.1 Lithography	3
1.1.2 Etching	3
1.2 Reactive Ion Etching	7
1.2.1 Plasma Properties	7
1.2.2 Etch Mechanisms	12
1.2.3 Sidewall Passivation	17
1.3 Applications of Feedback Control to Semiconductor Fabrication Processes	19
1.4 Outline of the Dissertation	22
2 Experimental Apparatus	23
2.1 Precision Etch 8300 Hexode RIE	23
2.1.1 Actuators	25
2.1.2 Sensors	26
2.1.3 Fluorine Concentration Estimate	27
2.1.4 Etch Rate Measurement	35
2.2 Data Acquisition and Control Platform	40
2.2.1 LabVIEW Data Acquisition and Control System	41
2.2.2 Signal Preconditioning	43
3 Dynamic Modeling of the Plasma Generation Process	49
3.1 Control-Oriented Decomposition and Control Strategy	49
3.2 System Identification of the Plasma Generation Process	53
3.2.1 Conductance Through the Throttle Valve	54
3.2.2 Dynamic Model	57

3.3	Model Validation	74
4	Etch Rate Control and Disturbance Rejection	77
4.1	Plasma Generation Process Controller	77
4.1.1	Controller Design	78
4.1.2	Implementation	92
4.2	Disturbance Rejection Experiments	92
4.2.1	Description of Experiments	94
4.2.2	Experimental Results	96
4.3	Comparison of Vbias/[F] vs. Vbias/Pressure Control	103
5	Sidewall Profile Control Strategy	106
5.1	Sidewall Control Strategy	106
5.2	Process Chemistry	108
5.3	Plasma Generation Process Model	110
5.4	Plasma Controller	112
5.4.1	Anti-Windup Design	114
5.4.2	Implementation	125
5.5	Etch Study	128
5.5.1	Wafer Preparation	128
5.5.2	Controlled Etch	131
5.5.3	String Model Simulation	132
5.5.4	Determining Etch Rate from the SEM Image	136
5.6	Implementation of the Sidewall Profile Control Strategy	136
6	Conclusion	139
6.1	Summary of Work	140
6.2	Future Directions	141
6.2.1	Long Term Etch Study	142
6.2.2	Implementation of Sidewall Profile Control Strategy	142
6.2.3	Additional Plasma Sensors	143
6.2.4	Other Etch Chemistries	144
6.2.5	High Density Plasma Sources	144
	APPENDICES	146
	BIBLIOGRAPHY	175

LIST OF FIGURES

Figure

1.1	The lithographic process.	4
1.2	Anisotropic and isotropic etching of small linewidths.	5
1.3	Step coverage over vertical and sloped sidewalls.	6
1.4	Typical parallel plate reactive ion etcher.	8
1.5	Schematic of an rf discharge circuit.	11
1.6	Voltage waveforms in rf discharge.	11
1.7	Potential distribution in an asymmetric parallel plate reactor.	13
1.8	Etch species and product.	13
1.9	Directional etch produced by ion bombardment.	16
1.10	Etch rate with and without ion bombardment	17
1.11	Sidewall passivation through polymerization.	18
1.12	Boundary between polymerization and etching as influenced by F/C ratio	19
2.1	Precision Etch 8300 hexode reactive ion etcher.	24
2.2	Atomic energy levels and emission wavelengths for F and Ar atoms.	29
2.3	Dilution of actinometer.	32
2.4	Actinometry system.	33
2.5	Optical spectrum of a CF ₄ / Ar plasma.	34
2.6	Stack of thin film materials	36
2.7	Reflectometry system.	38
2.8	Sample reflectometry signal.	39
2.9	Calculated etch rates.	40
2.10	Techware and LabVIEW wiring configuration.	41
2.11	Data acquisition timing diagram.	43
2.12	Example of LabVIEW code for data acquisition.	44
2.13	LabVIEW Control Setup Panel.	44
2.14	LabVIEW Monitor Panel.	45
2.15	Implementation of a lowpass filter.	47
2.16	Improved lowpass filter.	48
3.1	Conceptual decomposition of the RIE process.	51
3.2	Feedback control strategy for the reactive ion etching process.	52
3.3	Pressure response during conductance experiment.	55
3.4	dPrs/dt vs. pressure during conductance experiment.	55
3.5	Pressure response during volume experiment with a Ar flow of 14 sccm.	56

3.6	Flow through the throttle valve vs. pressure and throttle position.	58
3.7	V_{bias} data from power step experiment.	61
3.8	Fluorine concentration data power step experiment.	61
3.9	Noise reduction due to averaging of [F] signal.	62
3.10	Delay in response of V_{bias} to a step in power.	64
3.11	Step response: Power to V_{bias}	65
3.12	Bode plot: Power to V_{bias}	65
3.13	Delay in response of fluorine concentration to a step in power.	66
3.14	Step response: Power to fluorine concentration.	67
3.15	Bode plot: Power to fluorine concentration.	68
3.16	Delay in response of V_{bias} to a step in throttle position.	69
3.17	Detailed view of the delay in response of V_{bias} to a step in throttle position.	69
3.18	Time response: Throttle position to V_{bias}	70
3.19	Bode plot: Throttle position to V_{bias}	70
3.20	Delay in response of fluorine concentration to a step in throttle position. . .	71
3.21	Detailed view delay in response of fluorine concentration to a step in throttle position.	72
3.22	Bode plot: Throttle position to fluorine concentration.	73
3.23	Time response: Throttle position to fluorine concentration.	73
3.24	PRBS applied in model validation experiment.	75
3.25	Comparison of actual and simulated V_{bias} response to simultaneous PRBS inputs.	75
3.26	Comparison of actual and simulated fluorine concentration response to simultaneous PRBS inputs.	76
4.1	Phase lag from the Padé approximations of time delay.	79
4.2	Simulink block diagram: plasma generation process model.	79
4.3	State feedback diagram.	82
4.4	Simulated response of closed loop system to a step in V_{bias}	84
4.5	Simulated response of actuators to a step in V_{bias}	85
4.6	Simulated response of closed loop system to a step in fluorine concentration.	85
4.7	Simulated response of actuators to a step in fluorine concentration.	86
4.8	LQG/LTR closed loop system.	88
4.9	Controller gains from V_{bias}	91
4.10	Controller gains from fluorine concentration.	91
4.11	Simulink block diagram: controller structure.	93
4.12	Loading effect.	95
4.13	Wall disturbance experiment.	96
4.14	Response of plasma characteristics during standard practice etch.	98
4.15	Response of plasma characteristics during closed-loop etch.	99
4.16	Corresponding actuator responses during closed-loop etch.	100
4.17	Etch rate with plasma setpoints matching steady-state conditions from standard practice baseline etch.	100
4.18	Loading experiment.	101
4.19	Oxygen disturbance experiment.	102

4.20	Power disturbance experiment.	103
4.21	Comparison of the effects of the various disturbances.	104
4.22	Comparison of controlling pressure, V_{bias} /pressure, and $V_{bias}/[F]$	105
5.1	Sidewall control strategy.	107
5.2	Sidewall profile resulting from an etch with settings of 20 mTorr, 5 %O ₂ , 30 sccm total flow, and 1000 W power.	111
5.3	Sidewall profile resulting from an etch with settings of 10 mTorr, 1 %O ₂ , 30 sccm total flow, and 1200 W power.	111
5.4	Delay in response of pressure to change in throttle position.	113
5.5	Simulated response of closed loop system to step in V_{bias}	115
5.6	Simulated response of actuators to step in V_{bias}	116
5.7	Simulated response of closed loop system to step in pressure.	117
5.8	Simulated response of actuators to step in pressure.	118
5.9	Simulated response of closed loop system to step in fluorine concentration. .	119
5.10	Simulated response of actuators to step in fluorine concentration.	120
5.11	Bode plots of controller from V_{bias} to equipment inputs.	121
5.12	Bode plots of controller from pressure to equipment inputs.	122
5.13	Bode plots of controller from fluorine concentration to equipment inputs. .	123
5.14	Controller with anti-windup logic.	124
5.15	Simulated response of %O ₂ to fluorine disturbance for controller with and without anti-windup logic.	126
5.16	Controller structure with anti-windup.	127
5.17	The lift-off process.	129
5.18	Polymer formation under a chromium mask.	130
5.19	Wafer after nickel deposition.	132
5.20	Plasma characteristics during feedback control of the plasma generation process.	133
5.21	Corresponding actuator responses during feedback control.	134
5.22	SEM image of resulting sidewall profile.	135
5.23	Isotropic and anisotropic etch rate components.	135
5.24	Comparison of extracted edge profile with string model simulation	137
A.1	Cartesian and pixel coordinate systems.	157
A.2	Edge profile	158

LIST OF TABLES

Table

1.1	Etch chemistries.	10
3.1	Operating point for the plasma generation process model.	59
3.2	Transfer functions from power to V_{bias}	63
3.3	Transfer functions from power to fluorine concentration.	66
3.4	Transfer functions from throttle position to V_{bias}	68
3.5	Transfer functions from throttle position to fluorine concentration.	71
5.1	Operating point for CF_4/O_2 plasma	112
5.2	Software saturation limits.	125

LIST OF APPENDICES

APPENDIX

A	M-files Used in This Research	147
B	Surface Evolution Simulation	167

CHAPTER 1

Introduction

Microelectronic devices are finding wide applications in many diverse areas of life; from high-end engineering workstations to washing machines, integrated circuits are found everywhere. The desire to achieve better performance and more functionality has led to a continuous increase in the device density on these chips. This has most often been accomplished by reducing the feature size of the individual devices. Commercial devices are presently fabricated with feature sizes on the order of $0.35\text{ }\mu\text{m}$, while much smaller devices are under development in research laboratories. As critical dimensions shrink, better process control becomes important for a number of the fabrication steps. Tighter process control requirements will accelerate the adoption of *in situ* control methods and metrology [96]. Reactive ion etching (RIE) is one area in which real-time process control will become increasingly important [82].

The focus of this dissertation is to explore how real-time feedback control may be used to improve the reactive ion etching process. In particular, the goals of this research were to 1) configure a plasma etch tool to allow real-time feedback control, 2) develop control-oriented models of the etching process, 3) develop control algorithms based on these models, and 4) show that the application of real-time feedback control can improve the quality of

the etch process. In this introduction, I will provide a brief overview of microelectronic fabrication processes. This will be followed by a detailed discussion of the reactive ion etching process. The application of real-time control techniques to a variety of fabrication processes will then be described. I will conclude with a brief outline of the chapters of this dissertation.

1.1 Microelectronic Fabrication

Integrated circuits are fabricated on thin (~ 0.5 mm) disks of crystalline silicon known as wafers. These wafers are currently as large as 200 mm (8 inches) in diameter, and even larger wafers are planned for the near future. Each wafer may contain as many as 100 integrated circuit chips, with each chip containing over 3 million devices. Each of these devices needs to be uniformly fabricated with very small defect densities.

The fabrication process is often broken down into a number of mask levels; there are over twenty of these mask levels in the fabrication of a modern microprocessor. At each level several unit process steps are performed. These steps can be loosely arranged into three categories: film growth/deposition, doping, and pattern transfer. A complete description of the unit process steps can be found in [66, 101, 108] and the integration of these steps to fabricate working devices can be found in [101, 107]. The etching process is part of pattern transfer, so I will concentrate on describing this category.

Pattern transfer can be broken down into two process steps. In a process known as lithography, the desired geometric pattern is transferred from a mask to the mask layer on the wafer surface. Then, during the etch process, material is removed from areas left exposed by the mask layer. My research focused on applying real-time feedback control to the latter of these steps.

1.1.1 Lithography

The most commonly used material for the masking layer is a photosensitive polymer known as photoresist. Other materials (such as oxides, nitrides, and metals) are also used as masking layers, though photoresist is still used to define patterns in them. The lithographic process for photoresist is shown in Figure 1.1. First, the photoresist is spin-coated onto the wafer substrate and baked dry. The desired pattern for the mask level is then projected onto the photoresist. This is commonly done using ultraviolet light, though x-rays and electron beams are used in some applications. There are two types of photoresist, positive and negative. Positive photoresist contains an inhibitor component that prevents dissolution in a solvent [66]. During exposure, this inhibitor is chemically transformed and the resist becomes soluble. The resist is then developed using a solvent to dissolve the exposed regions. In the case of negative resist, the absorption of photons leads to crosslinking of the polymers [66]. During development, the crosslinked regions are not dissolved and the negative of the mask pattern is formed in the resist.

1.1.2 Etching

After the pattern has been transferred to the mask layer, the material left unprotected by the mask is removed. This process is known as etching. My research focused on the etching of polycrystalline silicon (polysilicon).

The etching process must be controlled to only remove the desired material layer, leaving the underlying layer essentially untouched. There are a number of characteristics that determine the quality of the etching process. These include, but are not limited to:

Etch Rate The rate of removal of material.

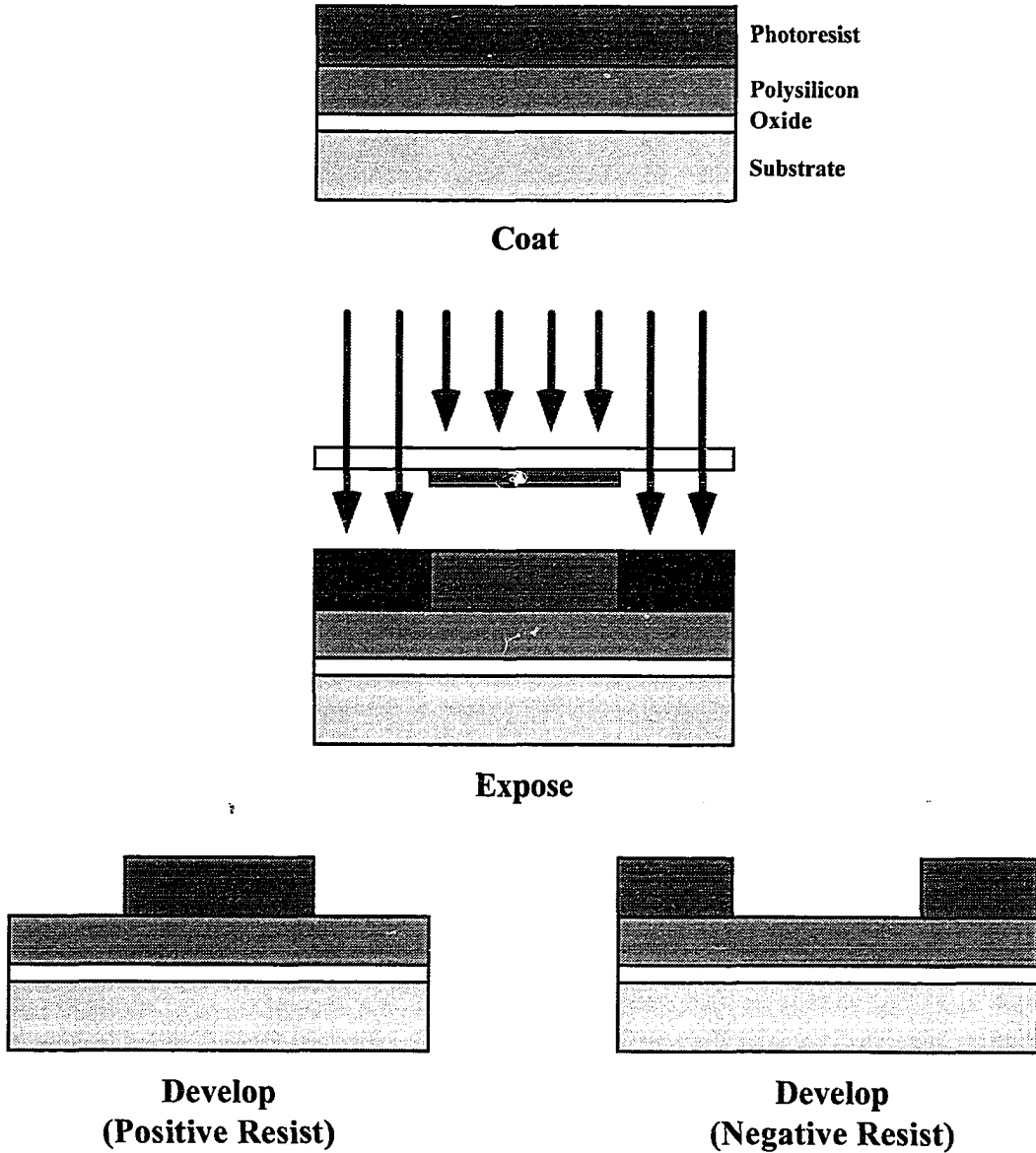


Figure 1.1: The lithographic process.

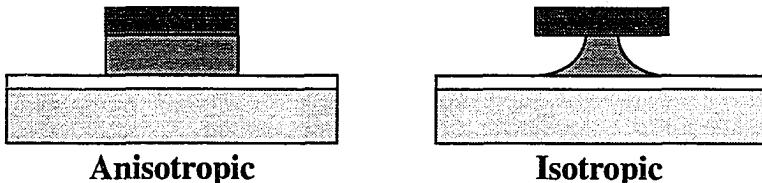


Figure 1.2: Anisotropic and isotropic etching of small linewidths.

Selectivity The etch rate ratio between the layer being etched and other layers, such as the photoresist or the underlying film.

Anisotropy The dependence of etch rate on direction. This usually refers to greater vertical than horizontal etch rate.

Uniformity The variation of the etch across the entire wafer or between multiple wafers in batch reactors.

Surface Damage Damage to the surface caused by the etch.

A useful etch process has a number of requirements on these characteristics [108]. In order to achieve high throughput, the etch rate should be rapid. Additionally, in many recipes the etch time is predetermined; therefore, the etch rate needs to have little variation from run to run. In order to preserve the integrity of the masked pattern, the etch needs to be highly selective with respect to the masking layer; otherwise mask erosion will lead to changes in critical dimensions. Selectivity to the underlying layer is also necessary, as it is important not to remove a significant amount of material from this layer. This is especially important in the etching of polysilicon where the gate oxide below the polysilicon can be as thin as 100 Å or less. The etch needs to be highly uniform so that the same amount of material is removed across the entire wafer. The degree of anisotropy is important in order to achieve an acceptable sidewall profile. Sidewall profiles need to be vertical when etching

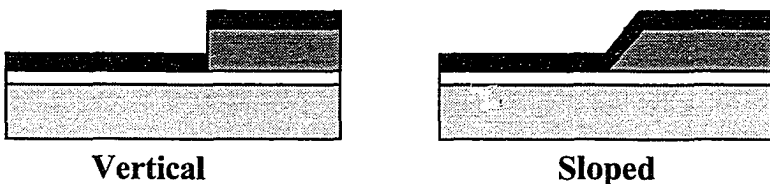


Figure 1.3: Step coverage over vertical and sloped sidewalls.

small linewidths; otherwise there will be a loss in the integrity of the transferred pattern, as shown in Figure 1.2. However, as is shown in Figure 1.3, sloped sidewalls are necessary when step coverage by subsequent materials is required. Finally, the electrical properties of the material below that layer being etched must be undamaged.

One of the early techniques for removing materials is known as wet etching. In wet etching the wafers are dipped into a liquid solution, such as hydrofluoric acid (HF), which chemically reacts with the exposed surface. Through the appropriate choice of chemistry, it is possible to get very high selectivity to both the mask and underlying layer. However, wet etching is isotropic¹; *i.e.*, material is physically removed in a direction normal to the surface. As depicted in Figure 1.2, when the critical dimensions are of the same size as the thickness of the layer being etched, isotropic etching can lead to significant changes in the desired linewidths. In this case, it is desirable to have a controlled degree of anisotropy in the etch.

As linewidths became smaller, an alternative technique known as dry etching emerged. In this technique, wafers are etched by being exposed to a low temperature plasma, as opposed to a liquid etchant. Dry etching can be broken down into a number of different regimes: plasma etching, sputter etching, and reactive ion etching. In plasma etching, neutral radicals generated in the plasma chemically react with the wafer surface to remove

¹There are situations where the orientation of the crystal can lead to an anisotropic wet etch, but these are beyond the scope of this introduction.

material. This process tends to be highly isotropic in nature. In sputter etching (or a related technique known as ion milling²), material is physical removed by high energy ion bombardment [43]; this provides highly anisotropic etching but unacceptable selectivities and surface damage. In between these two extremes is reactive ion etching, where the etch is both chemical and physical in nature. By the appropriate choice of conditions, trade-offs between anisotropy, selectivity, and surface damage can be made. Today, reactive ion etching is the main etch process used in integrated circuit production.

1.2 Reactive Ion Etching

In reactive ion etching, material is removed through the interaction of neutral radicals and ions from the plasma with the wafer surface. In this section, I will first present an overview of the plasmas used for reactive ion etching. This will be followed by a discussion of the various etch mechanisms.

1.2.1 Plasma Properties

A plasma is a collection of free charged particles moving in random directions; on average a plasma is electrically neutral and thus exhibits no net charge [68]. Plasmas used for semiconductor fabrication are, in general, weakly ionized, electrically driven, and not in thermal equilibrium. Overviews of plasmas used for microelectronic processing can be found in [16, 45, 68, 108].

In reactive ion etching, the plasmas are generated in a vacuum chamber at pressures between 5 and 100 mTorr. A typical parallel plate reactive ion etcher is shown in Figure 1.4. A mixture of gases enters the chamber through a showerhead in the upper electrode. Chamber

²Ion milling is similar to sputter etching except that ions are not generated in a plasma but from an ion source in a high vacuum environment.

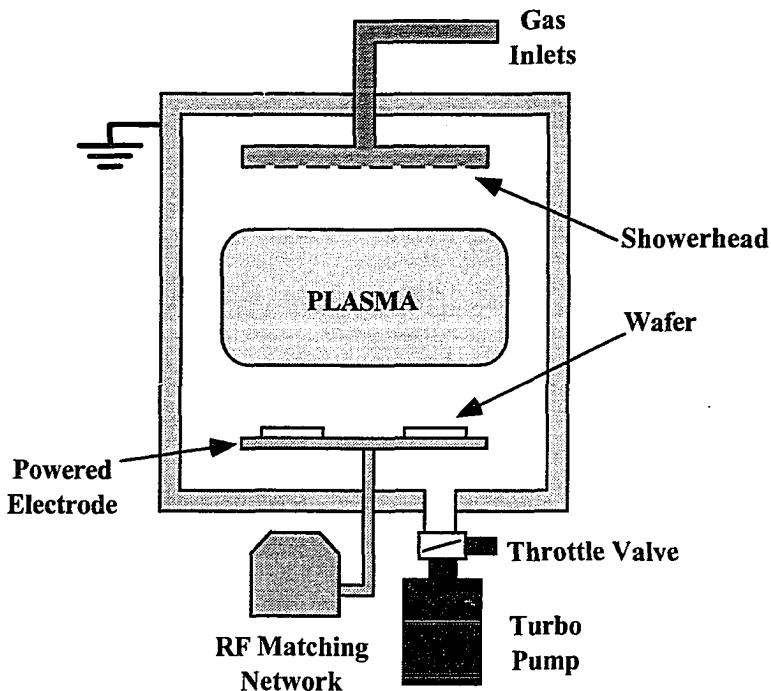


Figure 1.4: Typical parallel plate reactive ion etcher.

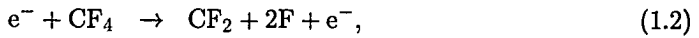
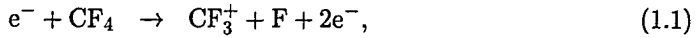
pressure is controlled by a throttle or sliding valve which regulates the exhaust of process gases by a high vacuum pump. A high frequency³ rf generator is capacitively coupled to the lower electrode, while the showerhead and chamber walls are grounded. The application of a large electric field across the electrodes results in ionization of the feed gas and generation of the plasma.

The electric field causes free electrons in the chamber to accelerate to high energies ($\sim 2\text{eV}$) and these electrons collide with various species in the gas, thereby inducing a number of reactions. The most important of these collisions in sustaining the plasma is electron impact ionization in which the primary electron removes an electron from the atom, producing a positive ion and two electrons [16]. These two electrons are accelerated

³Typically 13.56 MHz, a frequency which has been allotted by the Federal Communications Commission for industrial, scientific, and medical use [101].

by the field and produce additional collisions, often causing more ionizations. It is this chain reaction that sustains the plasma. If the colliding electron does not have sufficient energy to ionize the atom, it still may excite a bound electron to a higher energy level. When this electron relaxes down to a lower energy state, the atom emits a photon. It is this process that gives a plasma its characteristic glow and why plasmas are often referred to as *glow discharges*. Electrons may also collide with molecules and break the bonds between atoms. This dissociation process results in atoms and molecules, both neutral and ionized. Typically, on the order of 10% of the feed gas is dissociated [42]. Even with all of these various collision processes, the ionization for plasmas used in RIE is typically between 10^{-6} and 10^{-4} ; hence, these plasmas are made up mostly of neutral molecules.

The feed gas mixture used to produce the plasma depends on the material being etched. The chemistries used to etch various materials are shown in Table 1.1. In this research, real-time control was applied to CF_4 and CF_4/O_2 etching of polysilicon. A large number of reactions occur in these plasmas; many of which are listed in [12, 27]. The dominant reactions include [91]



The acceleration of the electrons by the rf field not only causes dissociation and ionization of the gas species, but also induces a bias on the electrode. This can be seen by assuming that the plasma potential is near zero, with respect to ground, and considering the model of

Material	Plasma Chemistries
Si	CF ₄ , CF ₄ /O ₂ , Cl ₂ , SF ₆ /O ₂ /Cl ₂ , NF ₃ , CCl ₄ , Br ₂
SiO ₂	CF ₄ , CF ₄ /H ₂ , CHF ₃ /O ₂
SiN ₃	CF ₄ /O ₂ /H ₂ , CHF ₃
Silicides	O ₂ , CF ₄ /O ₂ , SF ₆ /O ₂
Al	BCl ₃ , BCl ₃ /Cl ₂ , CCl ₄ /Cl ₂ /BCl ₃ , SiCl ₄ /Cl ₂

Table 1.1: Etch chemistries.

the rf discharge circuit shown in Figure 1.5. In this figure, V_a is the voltage of the generator, V_b is the voltage of the powered electrode, V_1 is the potential between the plasma and the powered electrode, V_2 is the potential between the plasma and the grounded electrode, and A_1 and A_2 are the surface areas of the powered and grounded electrodes, respectively. In order to sustain the discharge, ion current to the electrode must balance the electron current. Because the electrons are much lighter than the ions ($m_e \approx 10^{-4}m_i$), they require a much smaller field to conduct a given current. In order to balance the electron and ion fluxes, a negative dc bias develops on the powered electrode [52]. Therefore, as shown in Figure 1.6, V_b is positive for only a small portion of the rf cycle. The thickness across which this dc voltage develops is known as the sheath. The presence of the bias voltage leads to almost continuous bombardment of the wafer by the ions. At the same time, due to their small mass, electrons are rapidly accelerated away from the electrode. Therefore, the electron density in the sheath is drastically reduced. The electrons that are present in the sheath can gain higher energy from the field than those in the bulk plasma. When these electrons collide with atoms in the sheath, they are more likely to cause ionization, rather than excitation events [108]. This leads to less photon emission from relaxation of excited

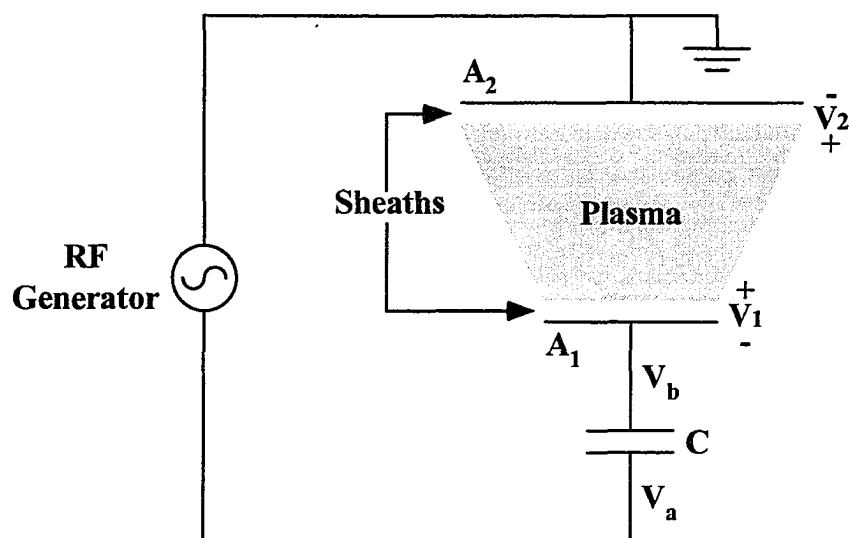


Figure 1.5: Schematic of an rf discharge circuit.

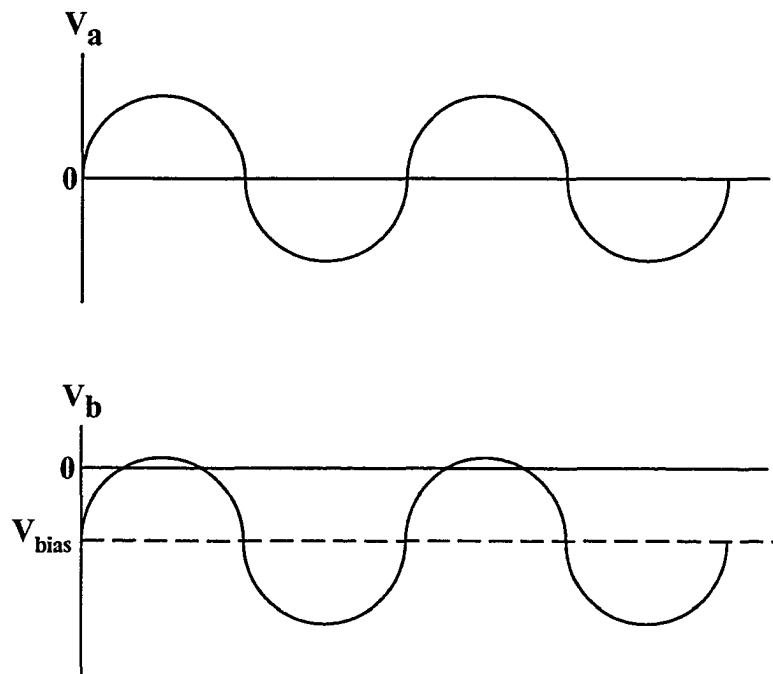


Figure 1.6: Voltage waveforms in rf discharge.

atoms than in the bulk; therefore, the sheaths are darker than the rest of the discharge and are also referred to as dark spaces. Complete details of this phenomenon can be found in [16].

A sheath also develops between the plasma and the grounded electrode leading to a positive plasma potential (V_2). If it is assumed that the ions traverse the dark space without collision then the voltages between each electrode and the plasma are related by [63]

$$\left(\frac{V_1}{V_2}\right) = \left(\frac{A_2}{A_1}\right)^4. \quad (1.6)$$

However, in practice most experiments have shown that

$$\left(\frac{V_1}{V_2}\right) \approx \left(\frac{A_2}{A_1}\right)^q, \quad (1.7)$$

with $q \leq 2.5$. It is thought that this difference is because the sheaths are not completely collisionless [16]. At process conditions used in this research the mean free path of the ions was on the order of 4 mm and the sheath thickness was measured to be approximately 13 mm. Therefore, ions collide rarely while traversing the dark space and the above relationship approximately holds. In RIE, the chamber walls are part of the grounded electrode; hence, the grounded electrode generally has a much larger surface area than has the powered electrode. This leads to a large bias between the plasma and the powered electrode (V_1), and a small one with respect to ground (V_2). The resulting potential distribution is similar to that shown in Figure 1.7. In this figure, the dc bias voltage refers to the bias of the powered electrode with respect to ground.

1.2.2 Etch Mechanisms

Reactive ion etching is actually a misleading name for the process [21]. A more descriptive name would be *ion enhanced etching*. In the RIE process, the surface is exposed

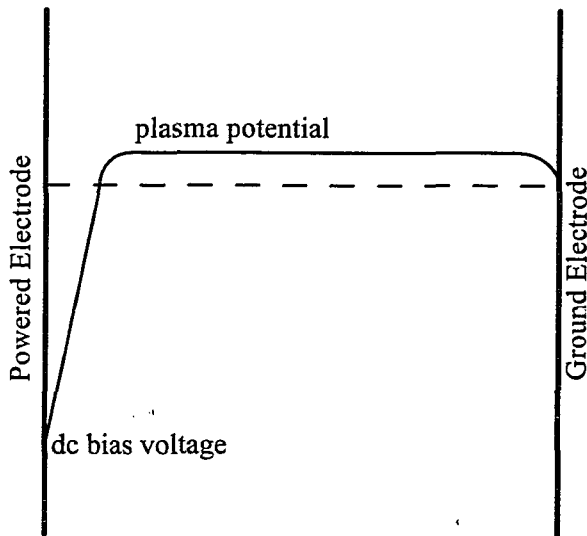


Figure 1.7: Potential distribution in an asymmetric parallel plate reactor.

to both thermal radicals and high energy ions. In the case of silicon etching performed in a tetrafluoromethane (CF_4) plasma, the neutral radicals are fluorine atoms and the ions are mainly CF_3^+ . Reactions at the surface lead to the formation of SiF_4 which desorbs, removing silicon from the surface (Figure 1.8).

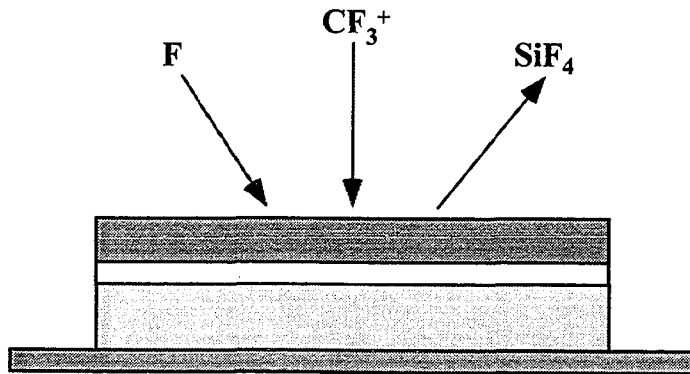
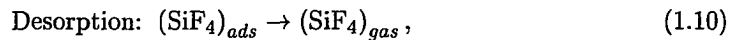
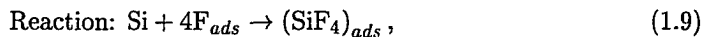


Figure 1.8: Etch species and product.

Role of neutral radicals

A number of steps must occur for etching to take place at the wafer surface. First, the radicals must diffuse to the wafer and adsorb onto the surface. The radicals then react with the surface material to form a volatile reaction product. Etching is complete when these reaction products desorb into the gas phase and diffuse away from the wafer surface. In the case of fluorine etching of silicon, these steps are



where the subscript *gas* denotes species in the gas phase and *ads* denotes species adsorbed onto the silicon surface. All of these steps are necessary for etching to proceed and any of them can limit the etch rate.

The adsorption step can be rate limited by the supply of fluorine at the surface. Therefore, the flux of fluorine radicals is an important parameter in controlling the etch. In general, the flux of a neutral species is given by [16]

$$\Gamma_x = \frac{n_x \bar{c}_x}{4} \text{ per unit area,} \quad (1.11)$$

where n_x is the concentration and \bar{c}_x is the mean speed of species x . The mean speed is given by

$$\bar{c}_x = \left(\frac{8kT}{\pi m_x} \right)^{\frac{1}{2}}, \quad (1.12)$$

where T is the temperature of species x , m_x is the mass of species x , and k is Boltzmann's constant. From this equation, it can be seen that the flux of fluorine radicals is proportional

to their concentration in the plasma. This fact was important to the development of the control strategy.

Role of the Ions

The role of the ions is not to react with the surface but to enhance reactions involving silicon and fluorine on the surface. In capacitively coupled plasmas, such as those used in reactive ion etching, the etch yield (silicon atoms etched per incident ion) is typically around 8 [103]. The major etch product is SiF_4 ; therefore, the removal of 8 silicon atoms requires 32 fluorine radicals. This is much more than can be provided by a single CF_3^+ ion. The main effect of the ions is therefore to enhance the chemical etching process.

There have been several mechanisms proposed to explain the effect of ion bombardment [73]. These include chemically enhanced physical sputtering [75], surface damage enhanced reaction rates [35], and ion assisted gas-surface chemistry. The latter is generally accepted for the case of fluorine etching of silicon [103]. It is believed that the energy supplied by ions impacting the surface increases the surface mobility, and thus enhances the formation and desorption of volatile products.

Ion bombardment can also change the nature of the reactions on the surface. Molecules of SiF_x will not spontaneously react to form volatile SiF_4 ; thus atomic fluorine is necessary for etching to occur [106]. However, ion bombardment will indeed cause this reaction to occur. In addition, while SiF_2 is normally strongly bound to the surface, ion collisions can leave this molecule in a weakly bound state [106]. Hence, the SiF_2 can then thermally desorb after the collision.

The degree to which the ions enhance the etch rate is a function of their incident energy. The etch yield for an ion increases with both the ion energy and the flux ratio between

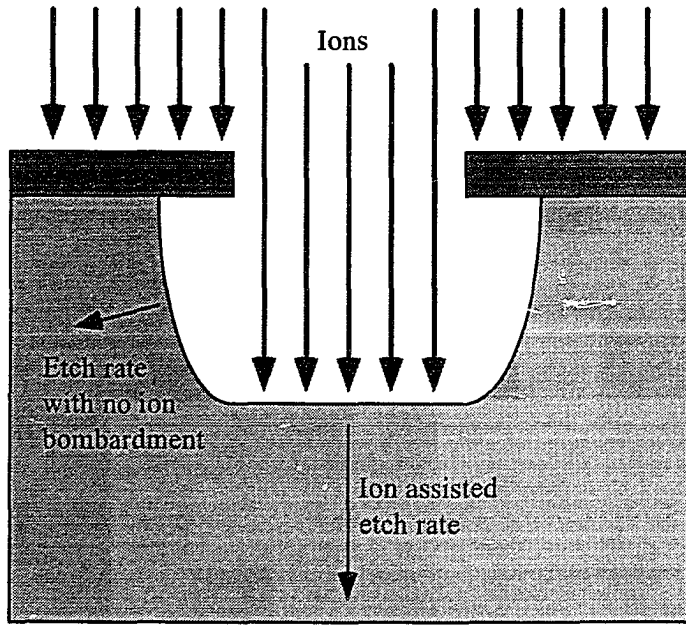


Figure 1.9: Directional etch produced by ion bombardment.

fluorine radicals and ions, approaching saturation for high flux ratios [44]. The removal rate of silicon atoms is thus

$$\text{Etch rate} = p_0 \left(\frac{\Gamma_F}{\Gamma_{Ions}}, \mathcal{E}_{Ions} \right) \times \Gamma_{Ions}, \quad (1.13)$$

where p_0 is the etch yield, Γ_F is the flux of fluorine radicals, Γ_{Ions} is the flux of ions, and \mathcal{E}_{Ions} is the energy of the ions. The energy of the ions is given by

$$\mathcal{E}_{Ions} = q (V_{plasma} - V_{bias}), \quad (1.14)$$

where q is a unit charge and V_{plasma} is the dc plasma potential shown in Figure 1.7. The plasma potential is generally small ($V_{plasma} \sim 20V$); therefore, assuming that most of the ions are singly charged, qV_{bias} is a good estimate of energy of the ions.

In reactive ion etching, it is the enhancement of etch rate due to ion bombardment that causes anisotropic etching. The ions only bombard the surface in areas left unprotected by the mask. Thus, as shown in Figure 1.9, ion enhanced etching occurs on the bottom surface,

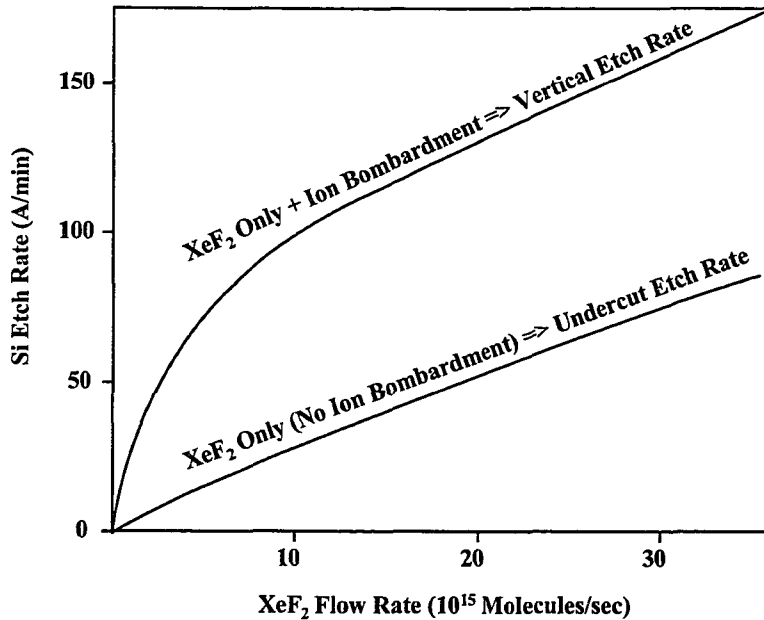


Figure 1.10: Etch rate with and without ion bombardment [38].

of a trench, while only chemical etching occurs on the sidewalls. The degree of anisotropy is controlled by the flux and energy of the ions, as well as the flux of neutral radicals.

1.2.3 Sidewall Passivation

Anisotropic etching is important to the production of microelectronic devices with small linewidths. Using ion beam studies with XeF₂ gas, it has been shown (see Figure 1.10) that the vertical etch rate and undercut etch rate go to zero together [38]. Therefore, it is not possible to get vertical sidewalls with a fluorine chemistry unless some sort of sidewall passivation is used. One method of achieving vertical sidewalls is by using a chemistry that deposits a polymeric film [42]. In this case, the polymerized films deposit on all the surfaces, including the surfaces of the trench being etched. As shown in Figure 1.11, high directional bombardment by the ions removes this film from the bottom surface but leaves the walls untouched [23]. This continuous clearing of the bottom allows etching to proceed in the

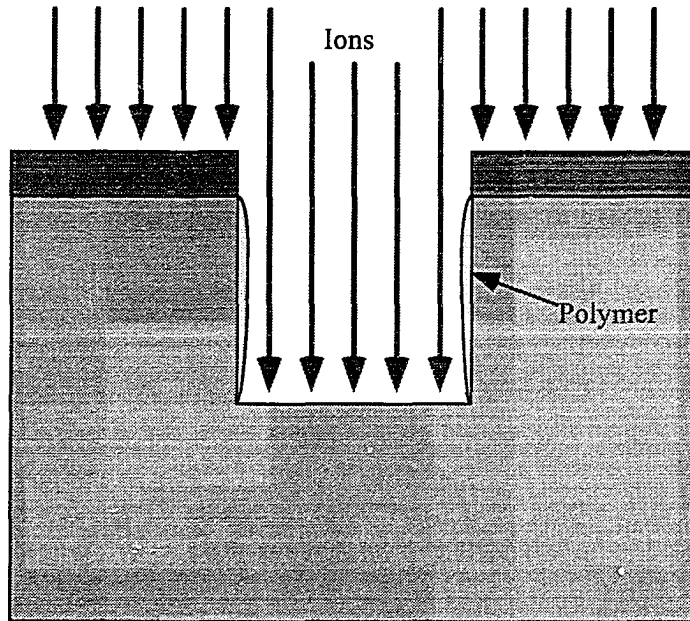


Figure 1.11: Sidewall passivation through polymerization.

vertical direction while the polymers inhibit etching of the sidewalls.

The key to this technique is to operate the plasma in a regime where polymeric films form on surfaces protected from ion bombardment while etching proceeds on the exposed surfaces. The separation between etching and polymerization can be *qualitatively* described by the fluorine-to-carbon (F/C) ratio of the plasma. The ratio includes only those species which participate in the etching or polymerizing chemistry (*e.g.* F, CF₃, CF₂, CF, CF₃⁺, *etc.*) and excludes inert species (*e.g.* CF₄, C₂F₆, SiF₄, CO, CO₂, HF, *etc.*). Increasing the ratio leads to increased Si etch rates, and decreasing the ratio lowers the etch rates and encourages polymerization [108]. The threshold between etching and polymerization varies with V_{bias} as shown in Figure 1.12. The F/C ratio can be varied by the addition of O₂ or H₂ to the feed gas. The addition of O₂ to the plasma chemistry consumes C (by forming CO and CO₂), while the addition of H₂ consumes F (by forming HF). By controlling the gas chemistry, polymers can be selectively deposited on the sidewalls and thus lead to

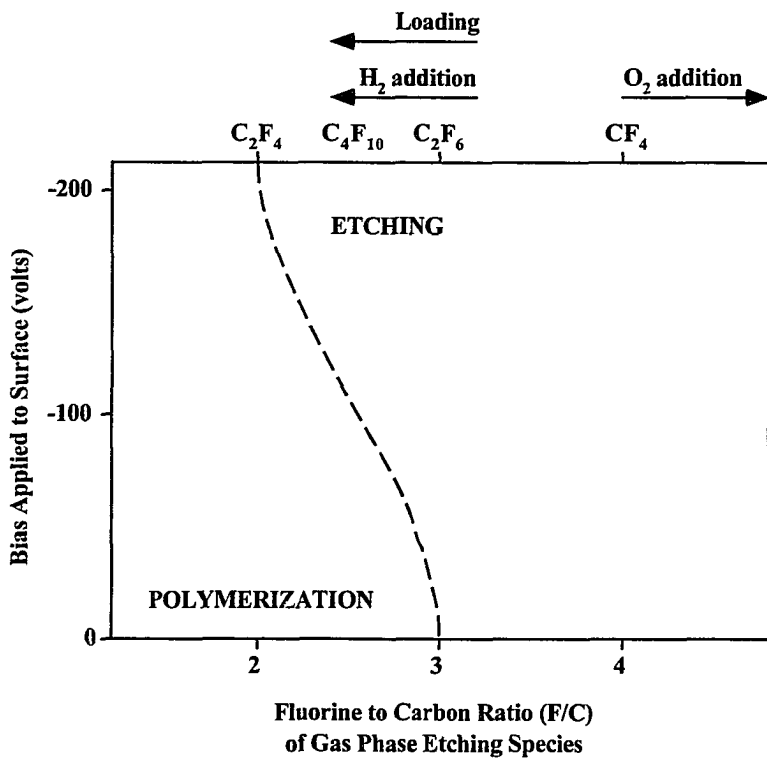


Figure 1.12: Boundary between polymerization and etching as influenced by F/C ratio [23].

anisotropic etching.

1.3 Applications of Feedback Control to Semiconductor Fabrication Processes

Traditional process control in the semiconductor industry has been primarily based on a collection of separate feedback loops relating one measurement of interest to one actuator. Over the past decade, there have been a number of different applications of multivariable feedback control to a variety of fabrication steps. Common to all of these applications is that the control algorithms are based on models of the particular process and in most

cases multiple process parameters (either of different process variables or of a single variable at different locations) are controlled by manipulating various equipment parameters. In addition, they all use real-time feedback in the sense that equipment parameters are manipulated during the process to maintain specified process conditions.

One of the first such applications was undertaken at the University of Texas at Austin. This group explored real-time monitoring and control for reactive ion etching of silicon and silicon dioxide [13, 76, 77]. This work applied block relative gain array analysis to silicon and silicon dioxide etching with both CF_4/O_2 and CF_4/H_2 plasmas. It was seen that single loop feedback control was inadequate for both of these etching processes [13]. Multivariable control was found to be effective in reducing dynamic process fluctuations.

During the fall of 1991, members of the Solid-State Electronics Laboratory and the Control Systems Laboratory at the University of Michigan began joint work on controlling the reactive ion etching process for polysilicon gate etching. An overview of applications of real-time feedback control to RIE at the University of Michigan was presented at the Electrochemical Society's 187th Meeting [46]. The basic idea of the control strategies is to decompose the reactive ion etching process into a plasma generation process and a wafer etch process. This will be discussed in detail in Section 3.1. Control of plasma characteristics has been shown to reject disturbances to the etch process [29, 86, 87]. The effect of controlling different sets of plasma characteristics was also explored [30], as well as the benefits of using a multiple-input multiple-output controller versus several "independent" single-input single-output controllers [30, 37]. In addition, this control strategy has been applied to etching amorphous silicon for thin film transistors [51]. A similar strategy has been applied to control sidewall profile [85]. The above work has been based on linear models and controllers for the plasma generation process. Nonlinear modeling and control have also

been applied [105].

Mutsukura, *et al.* [81] at Tokyo Denki University have applied real-time feedback to control optical sheath thickness and maximum optical intensity in etching plasmas. In this work, the spatial distribution of the optical emission intensity was measured with a CCD camera. Unlike the University of Michigan, no steps were taken to measure any particular wavelength of the emission. From this measurement, a sheath thickness and maximum optical intensity were extracted. A real-time feedback controller was used to regulate these plasma parameters by varying chamber pressure and applied power. It was shown that using this technique reduced the variance of etch depth over a number of trials.

Another application of modern control techniques has been to Rapid Thermal Processing (RTP) of single wafers. RTP is being explored as a possible way to overcome the uniformity problems associated with multiwafer furnaces [28]. A number of groups have been applying various modeling and control strategies to RTP. A joint group from Stanford University and Texas Instruments' Microelectronics Manufacturing Science and Technology project have been using low-order nonlinear models of a RTP system [93]. This model was then linearized and its unknown parameters were fit from experimental data [19, 95]. Based on this model, feedback control was applied using the Internal Model Control strategy [94]. Likewise, a group from the University of Texas at Austin [28, 100] has applied a successively linearized quadratic dynamic matrix control (QDMC) strategy [11] to an RTP developed at Sematech.

A strategy similar to that employed at the University of Michigan is being applied to plasma enhanced chemical vapor deposition (PECVD) at Carnegie Mellon University [18, 62]. This work has focused on the deposition of silicon nitride using SiH₄ and NH₃. A quadrupole mass spectrometer is used to measure key partial pressures in the plasma.

Experimental results will be presented in the near future [18].

All of the applications presented above focus on the processing of silicon wafers. Additionally, real-time control techniques have been applied to the processing of compound semiconductors. Looze, *et al.* [71, 72] have applied lead compensation to Czochralski growth of GaAs. Celii, *et al.* [14] have used spectroscopic ellipsometry to control layer thicknesses in AlAs/In_{0.53}Ga_{0.47}As resonant-tunneling diodes grown using molecular beam epitaxy (MBE).

1.4 Outline of the Dissertation

At the beginning of this introduction, the specific goals of this research were listed. First, it was important to configure our reactive ion etcher to allow the implementation of real-time feedback control. This will be described in Chapter 2. Next, as described in Chapter 3, a control-oriented model of the plasma generation process was developed. This model was used in Chapter 4 to design and implement a controller which rejects etch rate disturbances. The same strategy was employed in Chapter 5 to control sidewall profile. The dissertation will conclude with a discussion of future directions for this research.

CHAPTER 2

Experimental Apparatus

A major portion of the research presented in this dissertation has been experimental in nature. All of the plasma and etch experiments were performed using an Applied Materials Precision Etch 8300 (AME-8300)¹ which was donated by the manufacturer to the Solid-State Electronics Laboratory (SSEL) at the University of Michigan in 1987. This etcher, as with most commercially available etch systems, was designed for a production environment and was not configured for *in situ* measurements or the application of real-time control techniques. The first portion of my research focused on modifying our AME-8300 for the implementation of real-time feedback control.

2.1 Precision Etch 8300 Hexode RIE

The AME-8300 is a hexode reactive ion etcher (see Figure 2.1), where wafers are placed vertically on a hexagonally shaped powered electrode and the bell jar acts as the grounded electrode. The AME-8300 at the University of Michigan was designed to simultaneously etch 18 four inch wafers, though in this research it was used as a single wafer etcher. The hexode

¹The system was not truly an 8300 series etcher, but instead a hybrid between the 8100 and 8300 series. It is affectionately referred to as the "Mule."

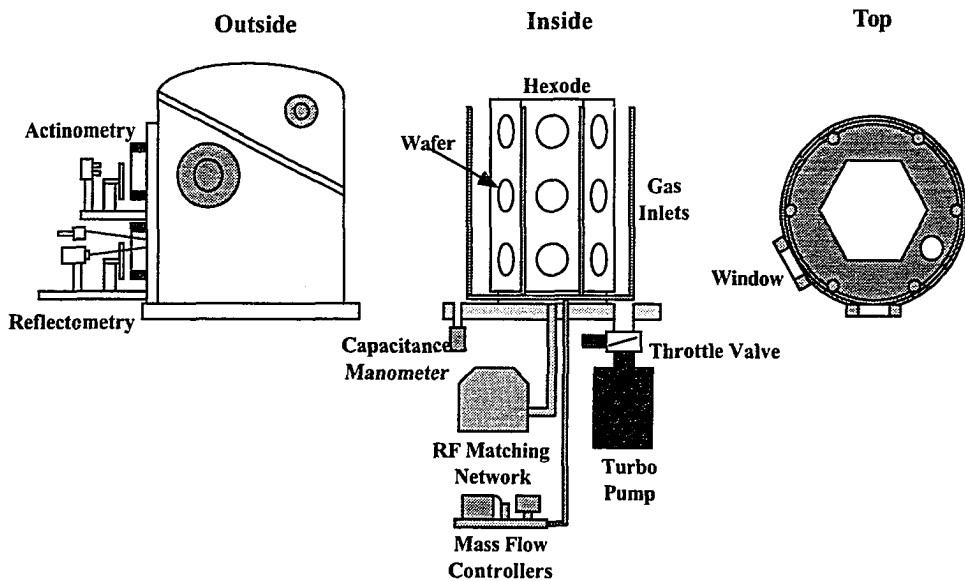


Figure 2.1: Precision Etch 8300 hexode reactive ion etcher.

has approximately one third the surface area of the bell jar. As was seen in Equation 1.7, this difference in surface area allows high energy ion bombardment of the powered electrode while minimizing the bombardment of the grounded electrode and other chamber surfaces. Process gases are mixed in a manifold and then enter the chamber in a sprinkler fashion through vertical pipes across from each corner of the hexode. The gas reactants are removed from the chamber by a turbomolecular pump with the exhaust conductance from the chamber regulated by a throttle valve. It is important to note that our system does not have a load lock, thus requiring the chamber to be vented to atmosphere each time a wafer is loaded. As will be explained in Section 4.2.1, this has had a strong impact on the etching process.

The AME-8300 comes standard with two viewports at which optical sensors can be mounted. One of the viewports is on the upper portion of the clam shell and moves with the top of the chamber when wafers are loaded. The other port has occasionally been

occupied by an infrared camera and more recently by a mass spectrometer. Neither port provided a stable mounting point for the optical sensors used in this research. Therefore, two additional 4 inch optical viewports were added to the face of the reactor where the gate valve for a load lock would have been situated. Optical breadboards were mounted below each of these windows to create a flexible and sturdy platform for the optical sensors.

2.1.1 Actuators

It was necessary to upgrade some of the actuators on the reactive ion etcher in order to improve our ability to control the process. The existing throttle valve, which regulates the exhaust of reactant gases from the chamber, had several shortcomings from the point of view of dynamic control. These included a large leakage conductance when fully closed, an operating regime near saturation, hysteresis in the motion of the valve, and the lack of a sensor for measuring actual valve position. The valve was replaced with an MKS Type 652A Throttle Valve and an MKS Type 653 Throttle Valve Controller. This valve was sized to be smaller than the old one, thus moving the operating region away from saturation. In addition, the valve has a low leakage conductance when fully closed, a good response time, and a sensor to measure the actual valve position. The throttle valve controller allows either the specification of a pressure setpoint to be regulated by an internal PID loop or the direct control of throttle position. The RF power actuator includes a Henry Electronics 2000W, 13.56 MHz generation unit and an RF Services RF8300RL matching network. The AME-8300 was originally supplied with a Micro-Match 8300N matching network supplied by Applied Materials. The upgraded matching network does a better job matching impedances (as measured by reflected power), has a quicker response time, and has a peak-to-peak voltage (V_{pp}) measurement. The V_{pp} is used by related research efforts, but not utilized

in this work. Gas flows are regulated by MKS Type 2259C Mass Flow Controllers and are mixed in a manifold prior to entering the process chamber. These flow controllers were sized to give the highest resolution over the flow rates necessary for this work.

During this research, short intermittent fluctuations in the gas flow rates were noted. It was suspected that these were due to the pressure regulator on the gas bottles [36]. These fluctuations, while short enough to have negligible effect on etch results, could make dynamic modeling difficult. The fluctuation problem was solved by placing a $2 \mu\text{m}$ VCR filter gasket in the outlet valve just downstream of the pressure regulator.

2.1.2 Sensors

Three types of sensors were used to make *in situ* measurements of the plasma environment for feedback control. The dc bias voltage (V_{bias}) was measured through an inductive tap on the powered electrode side of the matching network. Pressure in the chamber was monitored by an MKS Type 127A Baratron Capacitance Manometer. A typical operating regime for reactive ion etching in the AME-8300 is around 20 mTorr. The manometer, which originally had full scale range of 1 Torr, was resized to 100 mTorr to improve its resolution. The fluorine concentration is estimated via optical emission spectroscopy using actinometry; details of actinometry are presented in Section 2.1.3. In addition to these sensors, the AME-8300 was fitted with a laser reflectometry system to measure *in situ* etch rate; details on the reflectometry system are presented in Section 2.1.4. This measurement was only used to verify the performance of the control schemes and not for real-time feedback.

2.1.3 Fluorine Concentration Estimate

The fluorine concentration in the bulk plasma is strongly related to properties of the etch [44]. Unfortunately, it is not possible to directly measure fluorine concentration without perturbing the plasma. In research, various probes are sometimes used to sample the plasma chemistry; it is very difficult to relate plasma characteristics near the probe to those of the unperturbed plasma [56]. These probes are therefore not useful in measuring properties of a plasma during processing. Instead, the fluorine concentration is indirectly measured via optical emission spectroscopy using a technique known as actinometry.

Actinometry

The emission intensity from a spectral line of species x is given by [58]

$$I_x = N_x \left[\int_0^{\infty} Q_x(P, N_e) \sigma_x(\epsilon) N_e(\epsilon) d\epsilon \right], \quad (2.1)$$

where N_x is the concentration of species x , Q_x is the quantum yield from a given higher energy excited state to a given lower energy excited state, P is pressure, σ_x is the excitation cross section from the ground state to a given excited state of electron energy ϵ , and N_e is the electron density in an electron energy range $d\epsilon$. Because several of these parameters are unknown and impossible to measure, we use a technique known as actinometry [22]. In actinometry, a small amount of an inert gas, having excitation characteristics similar to the species of interest, is added to the feed gas; the inert gas is referred to as an actinometer. As will be seen below, the appropriate choice of spectral lines allows the concentration N_x to be determined without calculating the integral in Equation 2.1. Argon is used as an actinometer for fluorine concentration estimates.

The fluorine concentration estimate is found by first noting that the spectral line intensities are proportional to the corresponding excited state population densities (N_x^*) of each

of the species,

$$I_F \propto N_F^* \quad (2.2)$$

and

$$I_{Ar} \propto N_{Ar}^*. \quad (2.3)$$

It is necessary that the excitation efficiencies for the excited states corresponding to the spectral lines used in actinometry have similar dependence on plasma parameters [22]. In practice, both excited states need to have similar excitation thresholds and must only be populated from the ground state by electron collisions.

For fluorine actinometry, the 703.75 nm and 750.39 nm emission lines of fluorine and argon, respectively, satisfy these requirements. The excited states for these transitions have similar excitation thresholds [99], as shown in Figure 2.2. For low density plasmas, such as those used in RIE, these states are also only populated by electron excitation from the ground state [40]. From this choice of spectral lines:

$$\frac{N_F^*}{N_F} = \frac{N_{Ar}^*}{N_{Ar}}. \quad (2.4)$$

Therefore,

$$N_F = k \frac{I_F}{I_{Ar}} N_{Ar}, \quad (2.5)$$

where k is a proportionality constant known as the actinometric constant. We define γ to be the fraction of Ar in the chamber,

$$\gamma = \frac{P_{Ar}}{P} = \frac{N_{Ar}}{N}, \quad (2.6)$$

where N is the total concentration of species in the chamber. Note that from the ideal gas law

$$N = \frac{n}{V} = \frac{P}{RT}, \quad (2.7)$$

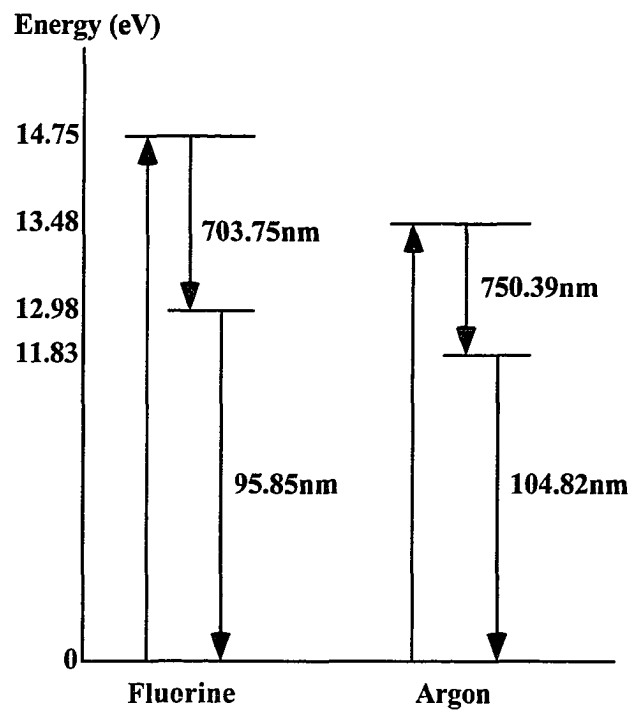


Figure 2.2: Atomic energy levels and emission wavelengths for F and Ar atoms [99].

where n is number of molecules, V is the chamber volume, P is the chamber pressure, R is the universal gas constant ($R = 8.314 \text{ J/mol}^\circ\text{K}$) and T is the temperature in degrees Kelvin. Therefore,

$$N_{Ar} = \gamma \frac{P}{RT} \quad (2.8)$$

and

$$N_F = k \frac{I_F}{I_{Ar}} \gamma \frac{P}{RT}. \quad (2.9)$$

Implicit in these equations is the assumption that the neutral temperature in the plasma remains constant. This assumption is based on the fact that the radicals remain "cold" in the plasma.

In general, it is assumed that the fraction of argon in the plasma is equal to the percentage of argon in the feed gas. This assumption is reasonable as the dissociation of the feed gases is usually between 0.01 and 10 percent [68]. This leads to the traditional estimate of fluorine concentration

$$N_F = \bar{k} \frac{I_F}{I_{Ar}} \gamma_{flw} P, \quad (2.10)$$

where $\bar{k} = \frac{k}{RT}$ and γ_{flw} is the percentage of total flow which is argon ($\gamma_{flw} = \frac{FLOW_{Ar}}{FLOW_{Total}}$). Thus, $\gamma_{flw} P$ is an estimate of the argon partial pressure (P_{Ar}). This equation is different from those traditionally seen in the literature [88] as it accounts for variations in the percentage of argon in the feed gas.

Throughout this dissertation no attempt was made to determine the actinometry constant k . In addition, during the etch rate control portion of this research the percentage of argon in the feed gas was held constant at 5% by premixing it with CF_4 in the gas bottle. Thus, the fluorine concentration estimate used in Chapters 3 and 4 was

$$[F] = \frac{I_F}{I_{Ar}} P. \quad (2.11)$$

In the sidewall profile control experiments, O₂ was added to the CF₄ chemistry. Initially, to insure a constant percentage of argon in the feed gas, a separate mass flow controller was used to regulate argon flow. The argon flow rate was typically quite small (~ 1.5 sccm) and the exact flow rate was not very reproducible. Therefore, the premixed CF₄ /Ar bottle was again used and the percentage of argon in the gas mixture dynamically calculated. Due to this, the fluorine concentration estimate used in Chapter 5 was

$$[F] = \frac{I_F}{I_{Ar}} \gamma_{flw} P. \quad (2.12)$$

The fluorine estimator presented in Equation 2.10 assumes that the relative concentration of argon in the chamber is equal to the percentage of argon in the feed gas. In the case when the dissociation is not negligible Equation 2.10 overestimates the actual fluorine concentration. In addition, as shown in Figure 2.3, outgassing from the chamber walls serves to dilute the argon partial pressure. This is particularly a problem for the reactor used in this research, as it does not have a load lock. It was necessary to expose the chamber to the ambient atmosphere every time a wafer was loaded to be etched. In doing this, water vapor adsorbs on the walls of the chamber; this moisture then desorbs when the plasma is struck. Because of the large surface area of the chamber walls, the moisture causes a large disturbance to the plasma which decays with a time constant on the order of 300 seconds. The effect of this disturbance on the etching process will be discussed in Section 4.2.

One solution to the problems associated with dilution of the actinometer is to measure the actual argon partial pressure in the chamber. This has been done by Jenq, *et al.*, for both RIE and electron cyclotron resonance (ECR) plasma using a mass spectrometer [58]. They noted that ion concentration was independent of applied power in RIE; this was not the case for ECR plasmas. This fact supports the assumption that there is a small percentage of dissociation in the plasma. Though not used in this research, an Extrel MS

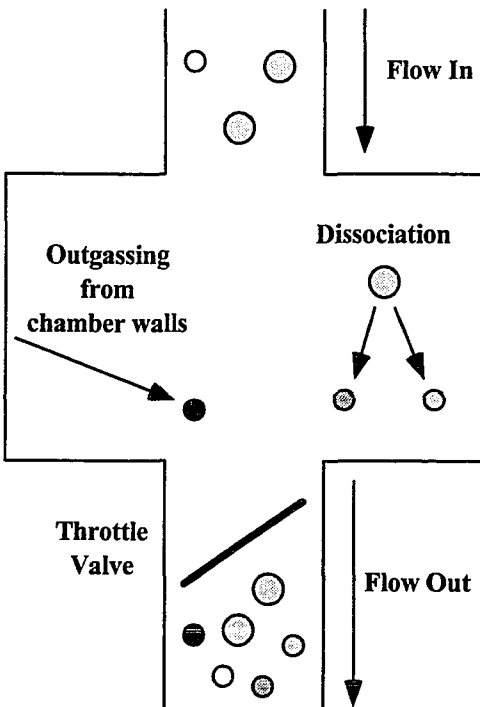


Figure 2.3: Dilution of actinometer.

250 mass spectrometer has recently been added to our AME-8300. It is our hope that this will allow us to account for argon dilution caused by outgassing from the chamber walls.

Optical Emission Hardware

The optics for collecting plasma emissions have gone through several iterations over the time period of this work, with the goal of providing better day-to-day repeatability and accuracy of the optical measurements. In the discussion below, I will only present the current system configuration.

The actinometry system is shown in Figure 2.4. Optical emission from the plasma is modulated to 1 kHz using a mechanical chopper and is collected by a fused silica fiber bundle. This bundle is bifurcated and sent to two Spex 500M 1/2 meter monochromators, each with a 1200 grooves/mm holographic grating with blaze wavelength of 750 nm. The

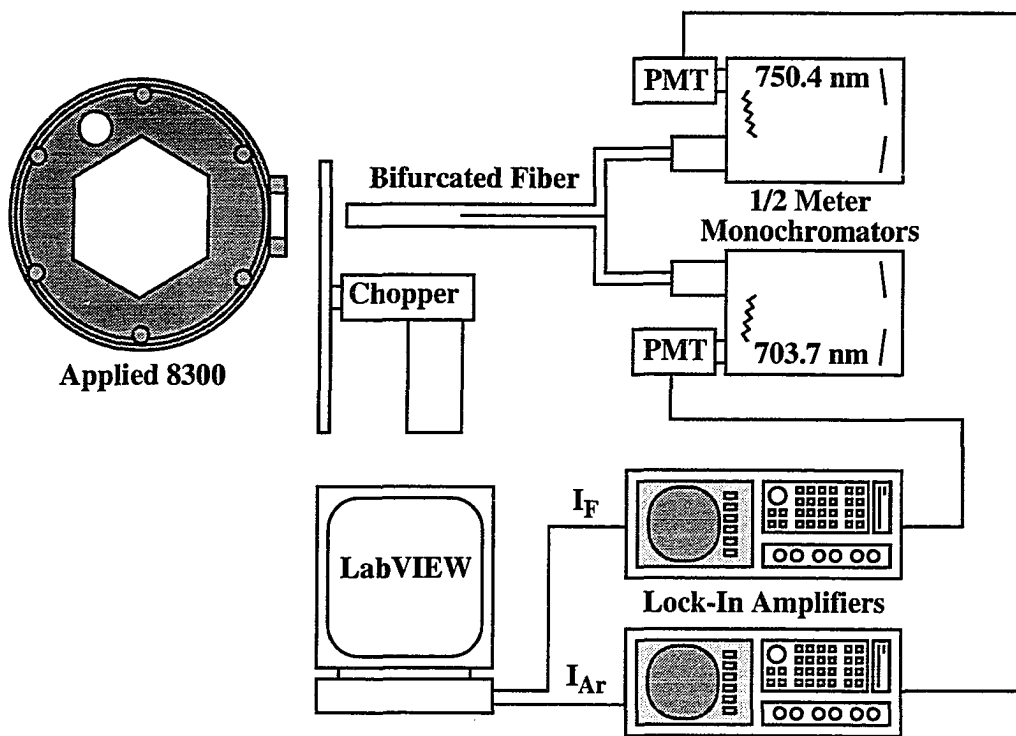


Figure 2.4: Actinometry system.

monochromators are calibrated using micro-stepper motors to the 703.7 nm and 750.4 nm wavelengths of the fluorine and argon spectra, respectively. The light is converted into electrical signals using thermoelectrically cooled Hamamatsu R928 photomultiplier tubes and demodulated with Stanford Research SR850 DSP Lock-In Amplifiers with a low pass filter time constant of 30 ms. These amplifiers use automatic phase correction, thus reducing sensitivity to chopper variations due to rf interference [9]. This system can also be used in a scanning mode to find the optical spectrum of the plasma. Figure 2.5 shows the optical spectrum between 675 and 775 nm for a CF_4/Ar plasma.

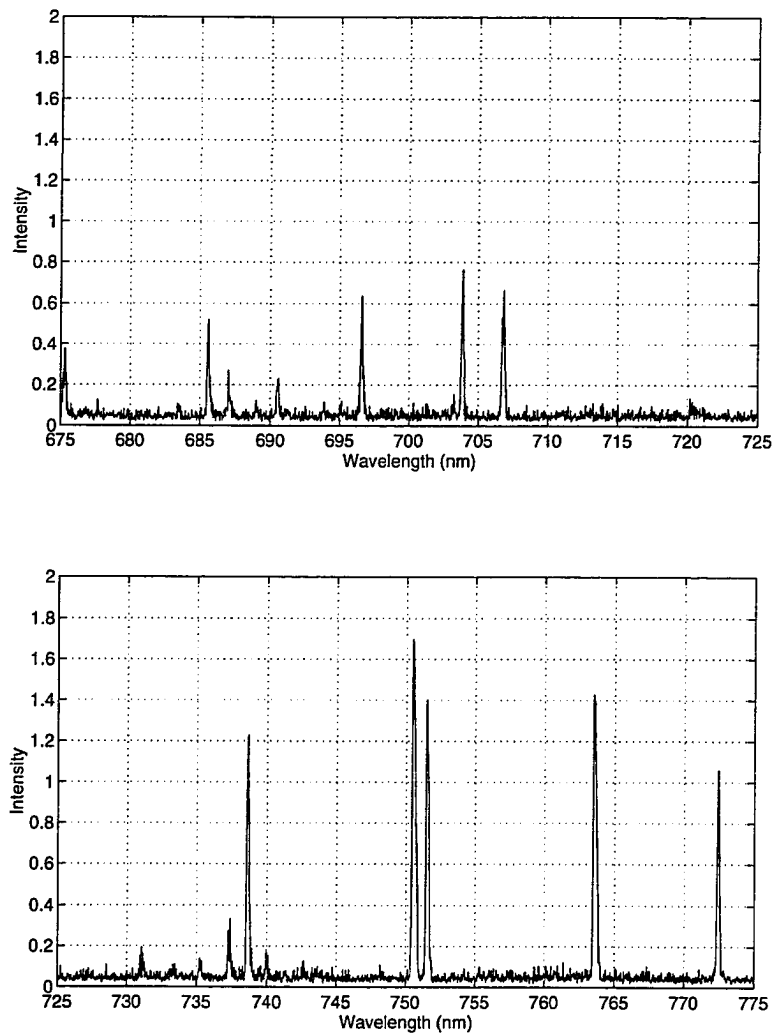


Figure 2.5: Optical spectrum of a CF_4 / Ar plasma.

2.1.4 Etch Rate Measurement

One of the performance metrics used for evaluating the effectiveness of the control strategies was their ability to reject disturbances to etch rate. In order to make this evaluation, the etch rate was measured during the length of the run through optical interferometry. After presenting a brief overview of interference from thin films, the hardware used in this research will be presented.

Interference in thin films

Due to optical interference, a stack of thin film layers exhibits a reflectance that is dependent on the wavelength of the incident light and the thicknesses of each film layer. This is seen by first noting that the change in phase of light traversing the m th layer of film is given by

$$\delta_m = \frac{2\pi}{\lambda_0} n_m d_m \cos \psi_m, \quad (2.13)$$

where λ_0 is the wavelength of the light in a vacuum, n_m is the index of refraction of layer m , d_m is the thickness of layer m , and ψ_m is the angle at which the light is incident on the interface between layers $m - 1$ and m . For light at normal incidence, the Fresnel reflection and transmission coefficients for an interface between films $m - 1$ and m are given by [49]

$$r_m = \frac{n_{m-1} - n_m}{n_{m-1} + n_m} \quad (2.14)$$

and

$$t_m = \frac{2n_{m-1}}{n_{m-1} + n_m}, \quad (2.15)$$

respectively. For light at angles other than $\psi_m = 0$ see [50].

We consider the stack of k thin film layers on a thick substrate (as shown in Figure 2.6) and adopt the convention that E_m^+ is the electric field traveling down at interface m and E_m^-

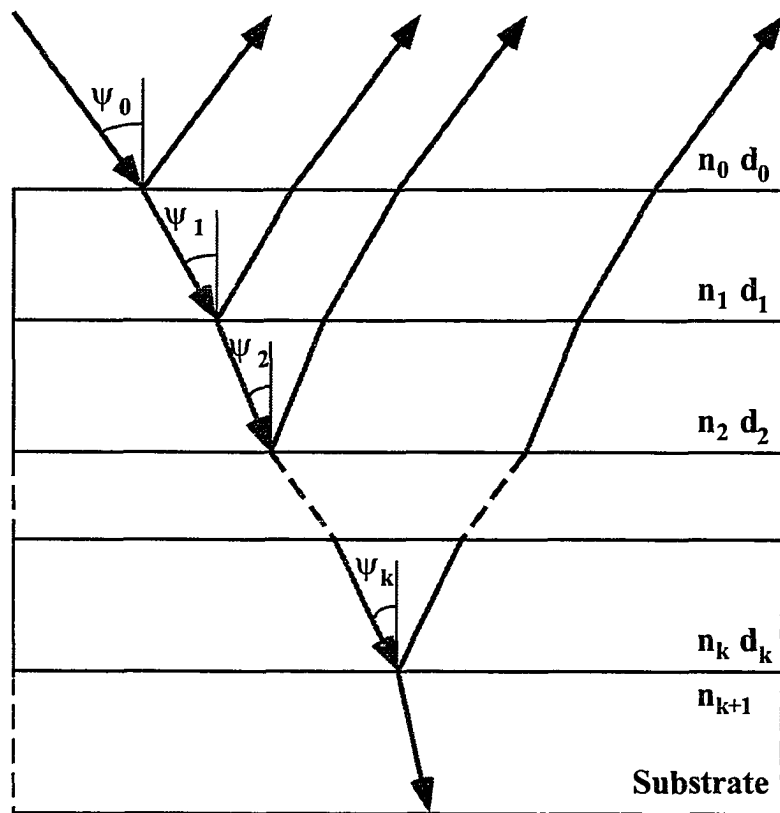


Figure 2.6: Stack of thin film materials

likewise refers to the electric field traveling up. A similar convention is also adopted for the magnetic field H . The following relationship is obtained by solving Maxwell's equations at each interface [49]

$$\begin{bmatrix} E_0^+ \\ E_0^- \end{bmatrix} = \frac{(C_1)(C_2) \cdots (C_{k+1})}{t_1 t_2 \cdots t_{k+1}} \begin{bmatrix} E_{k+1}^+ \\ E_{k+1}^- \end{bmatrix}, \quad (2.16)$$

where

$$(C_m) = \begin{bmatrix} e^{j\delta_{m-1}} & r_m e^{j\delta_{m-1}} \\ r_m e^{-j\delta_{m-1}} & e^{-j\delta_{m-1}} \end{bmatrix}. \quad (2.17)$$

We write the matrix product as

$$(C_1)(C_2) \cdots (C_{k+1}) = \begin{bmatrix} a & b \\ c & d \end{bmatrix}. \quad (2.18)$$

If the substrate is thick compared to the absorption wavelength of the incident light, then there is no negative traveling wave at the last interface, *i.e.*, $E_{k+1}^- = 0$; thus from Equation 2.16 we obtain

$$\frac{E_0^-}{E_0^+} = \frac{c}{a}. \quad (2.19)$$

The reflectance R of the multilayer stack is therefore given by [49]

$$R = \frac{(E_0^-)(E_0^-)^*}{(E_0^+)(E_0^+)^*} = \frac{cc^*}{aa^*}. \quad (2.20)$$

The interference between light reflected from the various surfaces changes as material is removed during the etching process. Therefore, a measurement of the reflectance of the wafer can be used to determine etch rates during an etch.

Reflectometry Hardware

The reflectometry system shown in Figure 2.7 is based on a single wavelength source, provided by a HeNe laser. The beam is modulated by a mechanical chopper before entering

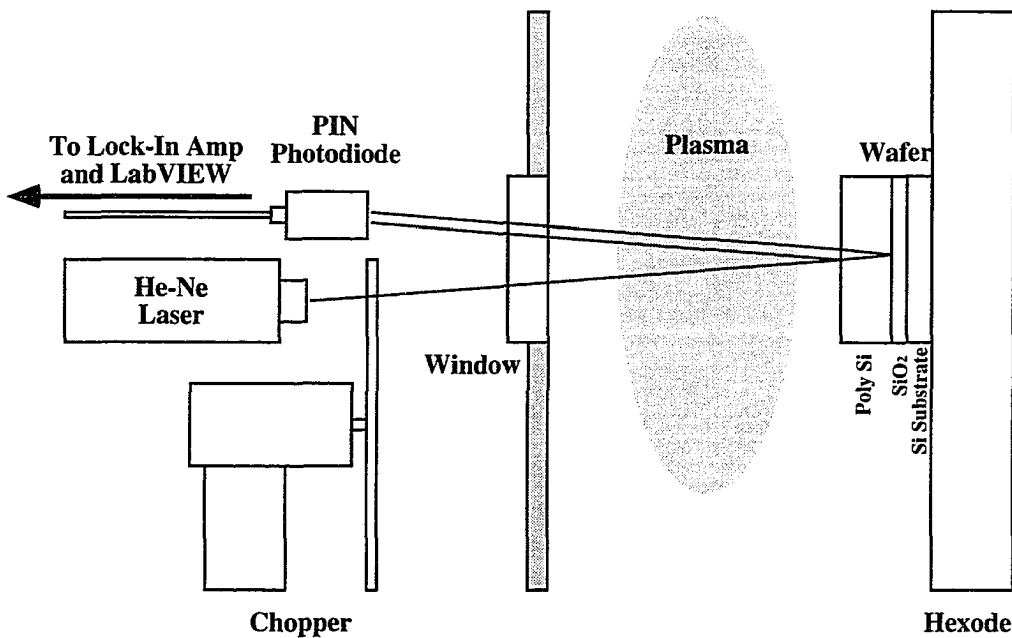


Figure 2.7: Reflectometry system.

the chamber. The reflected beam is then collected by a Thorlabs PDA50 p-i-n photodiode and amplified by a Stanford Research SR530 Lock-In Amplifier with a low pass filter time constant of 1 second. This amplifier does not have an automatic phase correction feature, but this was not a problem as there is ample signal-to-noise in this signal.

A typical trace of the reflectometry signal is shown in Figure 2.8. It can be found from Equation 2.20 that for a single wavelength of light at normal incidence ($\Psi_0 = 0$), the peaks and valleys in the interference pattern correspond to thickness differences of $\frac{1}{4} \frac{\lambda_0}{Re(n)}$, where $Re(n)$ is the real component of the index of refraction of the layer being etched. For the HeNe wavelength of 632.5 nm, the time between a peak and valley corresponds to the etching of 417 Å of polysilicon ($Re(n) = 3.768$). The x's in Figure 2.9 show the average etch rate (417 Å divided by the time between the peak and valley) plotted at the midpoint of

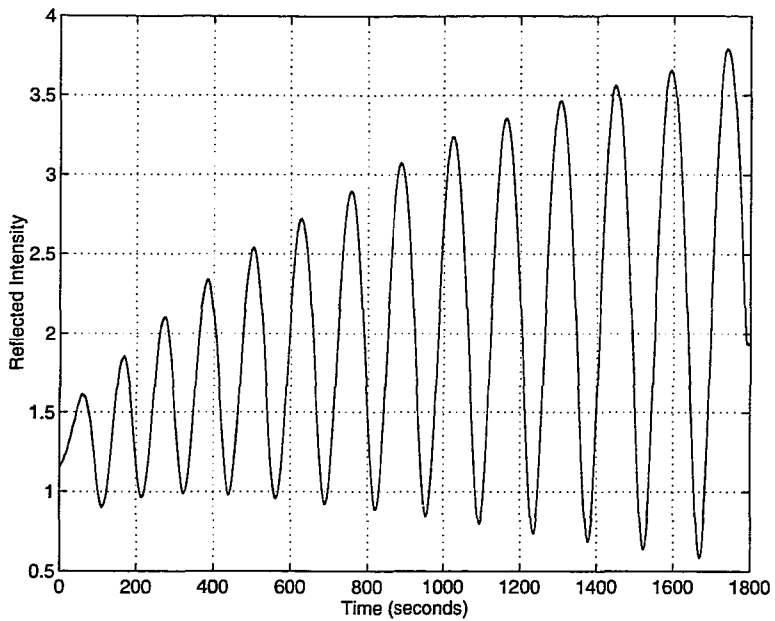


Figure 2.8: Sample reflectometry signal.

each time interval. From this figure there appears to be an oscillation in the etch rate, but this actually is due to the fact that the surface roughness of the polysilicon layer was not accounted for. To help in visualizing the actual etch rate, a smooth polynomial is fit to this data as shown in Figure 2.9. Note that data points are only available approximately once a minute. This is too slow to be used for real-time feedback.

Though not used in this research, two efforts have recently been undertaken to provide an etch rate measurement for real-time feedback. One of these involves developing an etch rate estimator which can extract information out of the HeNe signal at a much higher frequency [104]. The other utilizes a broader band light source, provided by a tungsten halogen lamp, and a CCD array as a detector [9].

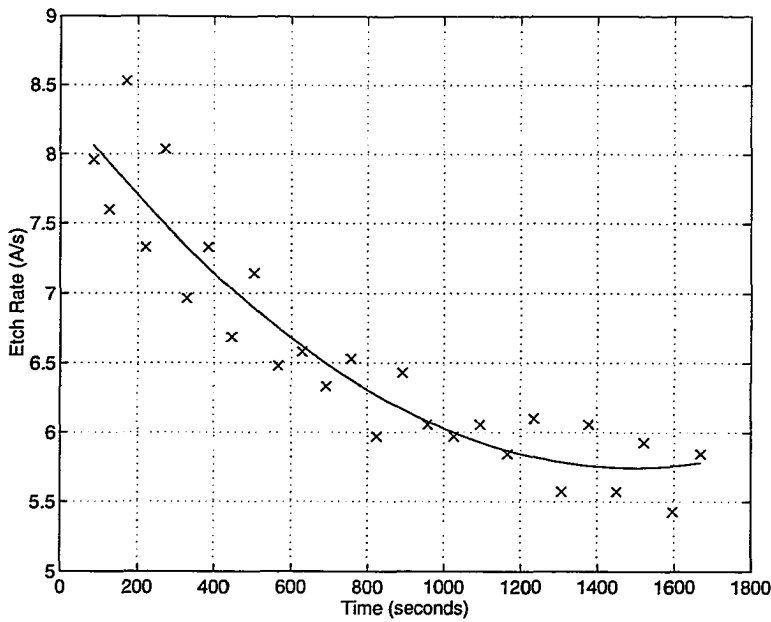


Figure 2.9: Calculated etch rates.

2.2 Data Acquisition and Control Platform

The largest modification made to the etcher was to upgrade its data acquisition and control software/hardware. Prior to the beginning of this work, the original control system on our AME-8300 had been replaced by a Techware Systems PAL 68000 process control computer. This system was excellent for running event-driven process recipes but was not capable of real-time monitoring and control². Two major limitations were: 1) data collection was (asynchronously) polled and 2) sampling rates were limited to approximately twice a second. These limitations were overcome by implementing a data acquisition and control system using LabVIEW³ to collect data and perform real-time control actions.

²Recently, in joint work with Techware Systems, we have shown that it is possible to implement real-time control algorithms on Techware's next generation of process control computers, the T-II. Work is continuing to develop a commercially available implementation.

³LabVIEW is a graphics-based programming language from National Instruments that provide drivers for their interface boards.

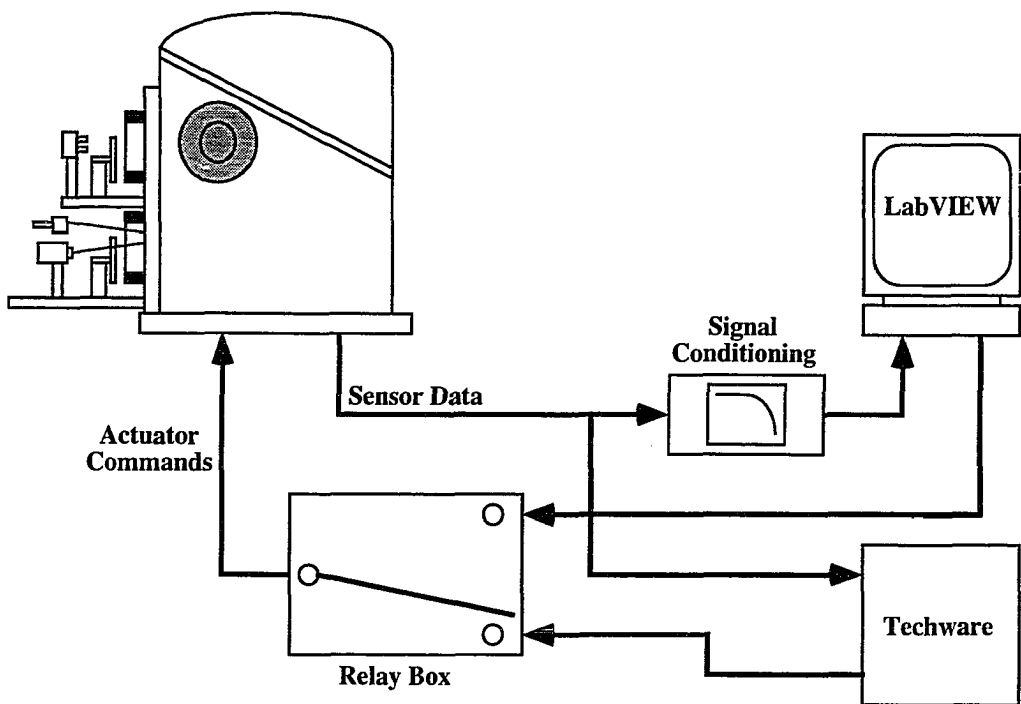


Figure 2.10: Techware and LabVIEW wiring configuration.

2.2.1 LabVIEW Data Acquisition and Control System

In order to provide the data acquisition and control capabilities necessary to build dynamic models and apply feedback control, an Apple Quadra 950 running LabVIEW was piggy-backed onto the Techware computer. The LabVIEW system was only used during the segment of the etch process when the plasma was lit; wafer loading, pumpdown, venting, etc. are all controlled by the Techware computer. During the time when the plasma is lit, a bank of relays gives control of the equipment setpoints to the LabVIEW system, while sensor data can be simultaneously monitored by both computers. This wiring configuration is shown in Figure 2.10.

Our LabVIEW system consists of three expansion bus boards:

NB-MIO-16-25L a multifunction input-output board which has 16 signal-ended analog inputs, 2 analog outputs, 8 TTL inputs/outputs, and 3 counter-timers.

NB-AO-6 an analog output board with 6 channels.

NB-DMA-2800 which provided direct memory access (DMA) and a high speed IEEE 488 (GPIB) interface.

In developing the LabVIEW data acquisition and control system, care was taken to synchronize the timing of the various input and output channels. One of the counter/timers (CNTR#1) was configured to produce a square wave with the period of the sampling interval. This signal is shared among the various boards via a real-time system integration (RTSI) bus, which is a local bus connecting the boards. As seen in Figure 2.11, the sample interval begins on the rising edge of the CNTR#1 signal. When this rising edge occurs the analog output (AO) channels are updated and reading of the analog input channels (AI) is initiated. While the NB-MIO-16-25L board has 16 input channels, it only has one analog-to-digital (A/D) converter. A multiplexer switches between channels on the rising edge of an AI conversion pulse generated by a second counter (CNTR#2). The A/D converter on this board has a settling time of $25 \mu s$; however due to a software bug in the data acquisition drivers the period of the AI conversion pulses was set to $90 \mu s$. The number of conversions is controlled by CNTR#1 (the gating pulse), in that the CNTR#2 only runs when the gating pulse is high. After all of the channels are acquired, the next control action is calculated and the inactive output buffer is loaded with the new values. More details on timing for real-time control implementations can be found in [7].

LabVIEW is a graphics-based programming language in which programs are written by “wiring” icons together. An example of LabVIEW code for reading data from the analog

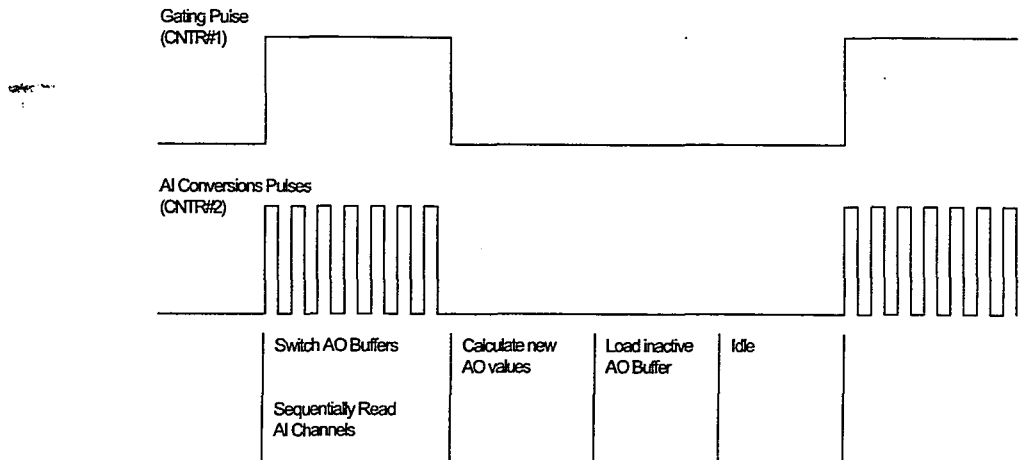


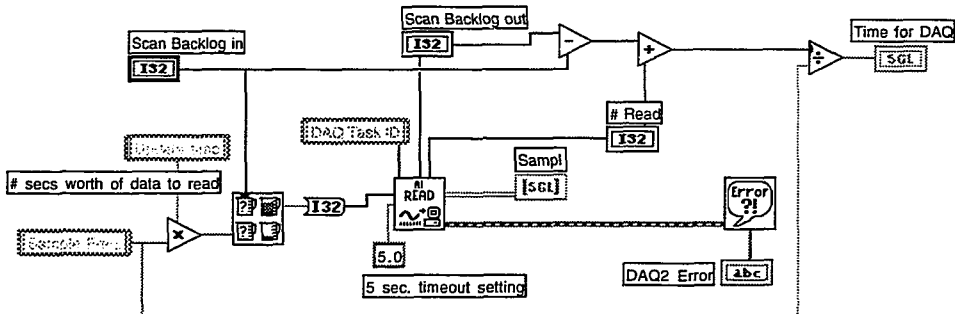
Figure 2.11: Data acquisition timing diagram.

input channels is shown in Figure 2.12. LabVIEW also provides the programmer with a number of widgets in which a graphical interface (or panel) can be developed for the user. One such panel is the Control Setup Panel, shown in Figure 2.13. From this panel the user can select data acquisition and control parameters for the etch. It allows the user to select the controller file, reference command file and sampling rate to be used for the etch. In addition, the user can select which sensor channels will be displayed to the screen and logged to disk for future analysis. The selected sensor channels are displayed on strip charts on the Monitor Panel (Figure 2.14) during the etch.

2.2.2 Signal Preconditioning

In sampling an analog line, it is important to take precautions against a phenomenon known as aliasing [78]. If the signal being sampled contains frequency components that are higher than half the sampling frequency (f_s) then these components may appear to be low frequency components. This can particularly be a problem if there are high frequency periodic signals [6]. To prevent aliasing, a low-pass filter known as an antialiasing filter is

Block Diagram



Time past while samples arrived = ((# Read) + (# Backlog Out - # Backlog In))/Freq

Figure 2.12: Example of LabVIEW code for data acquisition.

Front Panel

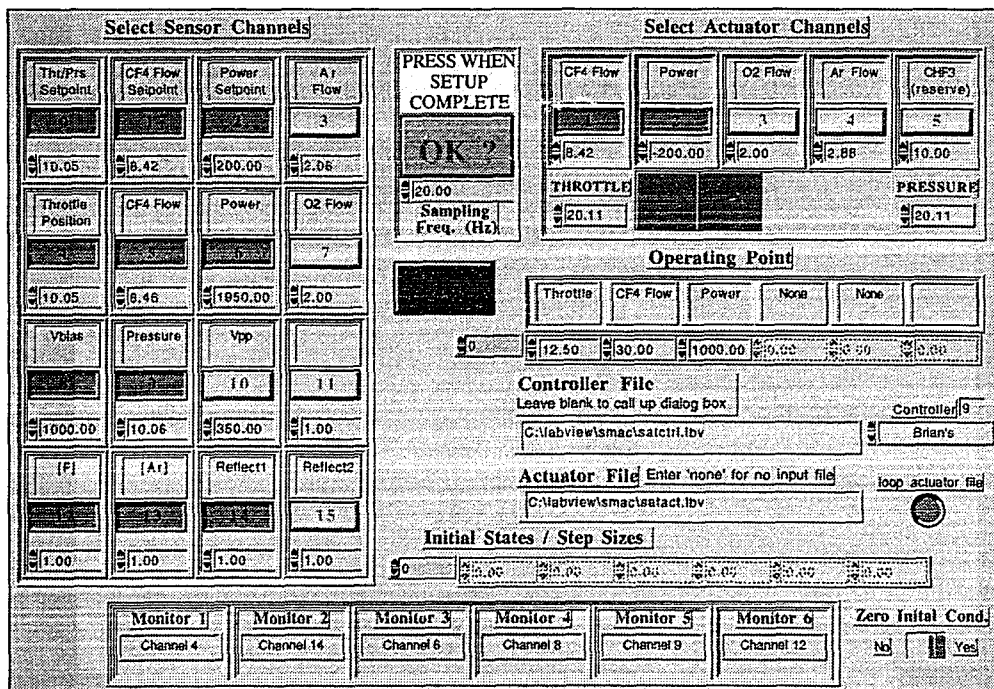


Figure 2.13: LabVIEW Control Setup Panel.

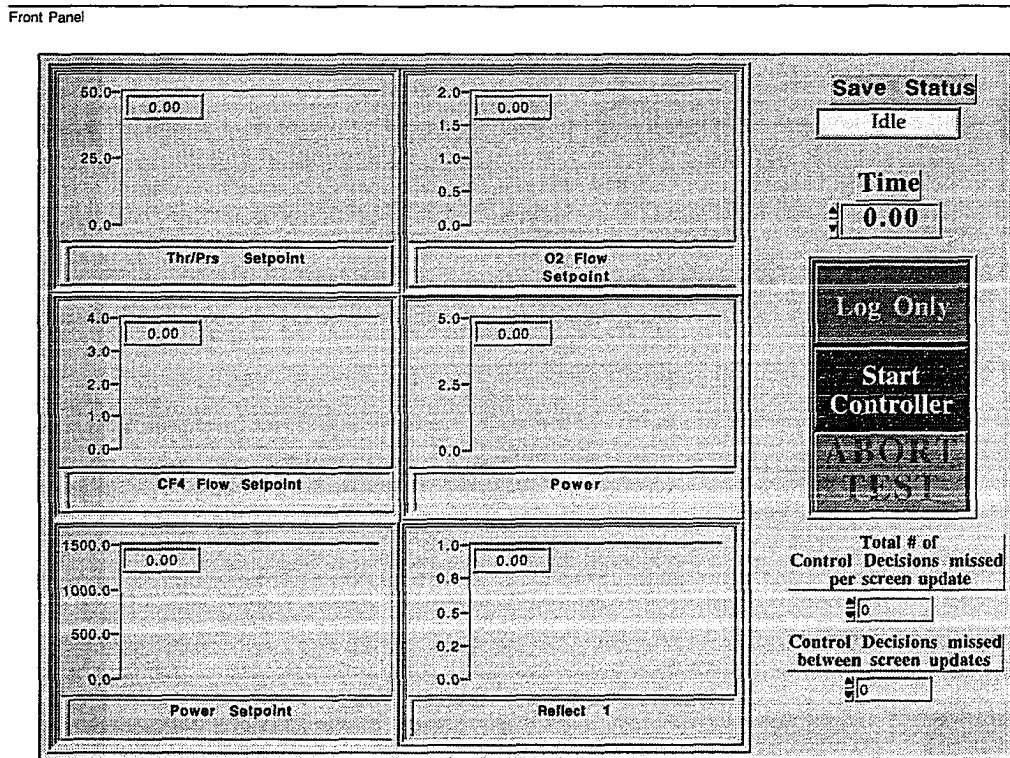


Figure 2.14: LabVIEW Monitor Panel.

used to remove high-frequency components from the signals before sampling. Often either Butterworth [78] or Bessel [6] filters are used for this task.

Second-order Butterworth filters were chosen for our system. These were designed around a single operational amplifier as shown in Figure 2.15 [55]. For a Butterworth filter with corner frequency f_c , the resistors and capacitors are chosen such that

$$f_c = \frac{1}{2\pi RC} \quad (2.21)$$

and

$$K = 1.586. \quad (2.22)$$

The LabVIEW data acquisition system was capable of collecting data at 45 Hz. Therefore, the desired corner frequency was 22.5 Hz. In practice, the resistors and capacitors had to be chosen to correspond to standard values. The filter was implemented with

$$R = 24.1 \text{ k}\Omega, \quad (2.23)$$

$$(K - 1) R = 15.9 \text{ k}\Omega, \quad (2.24)$$

and

$$C = 0.33 \mu F. \quad (2.25)$$

These values lead to

$$f_c = 19.4 \text{ Hz} \quad (2.26)$$

and

$$K = 1.606. \quad (2.27)$$

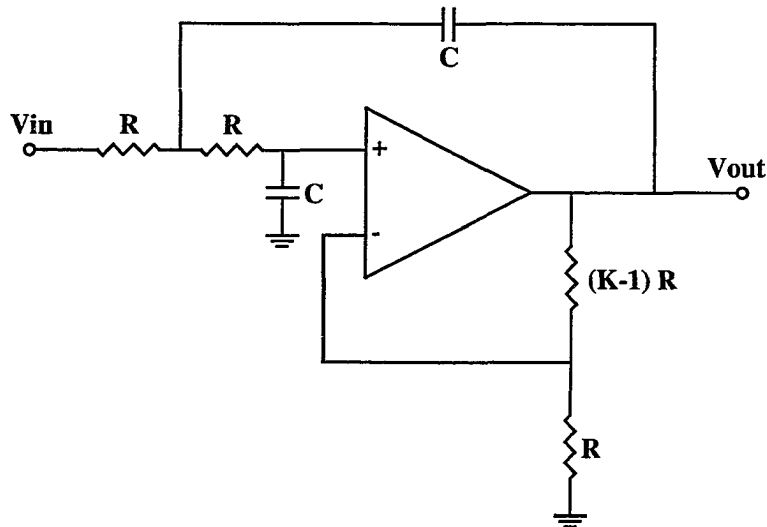


Figure 2.15: Implementation of a lowpass filter.

The analog input channels on the NB-MIO-16 board were configured with a range of 0 to 10 Volts. If the filters are connected to the input channels at V_{out} , the analog channels will saturate at a filter input voltage of $V_{in} = 6$ V. A voltage divider was added to step the filter gain down to unity. However, because the operational amplifier was powered by ± 15 V, V_{out} still saturates at 14.3 V. This saturation occurs at $V_{in} = 8.9$ V, thus limiting the measurable voltage range to 0 – 8.9 V. In general, this was not a problem for us as most signals remained below 8 volts during normal operation of the system. The exception to this was the optical input signals where it was convenient to have the full 10 volts of range. Recently, the voltage was stepped down at the input stage using a voltage divider and unity gain buffer, as shown in Figure 2.16. This allows the full 0 – 10 V range for the measured inputs. In addition, several of the signals, such as V_{bias} and power, had ranges between 0 and -10 volts. Therefore, inverting amplifiers were used to bring these voltages into the range of the input channels. Finally, the inverting amplifiers drew enough current on the V_{bias} channel to actually drop the voltage at the electrode, so a high impedance unity gain

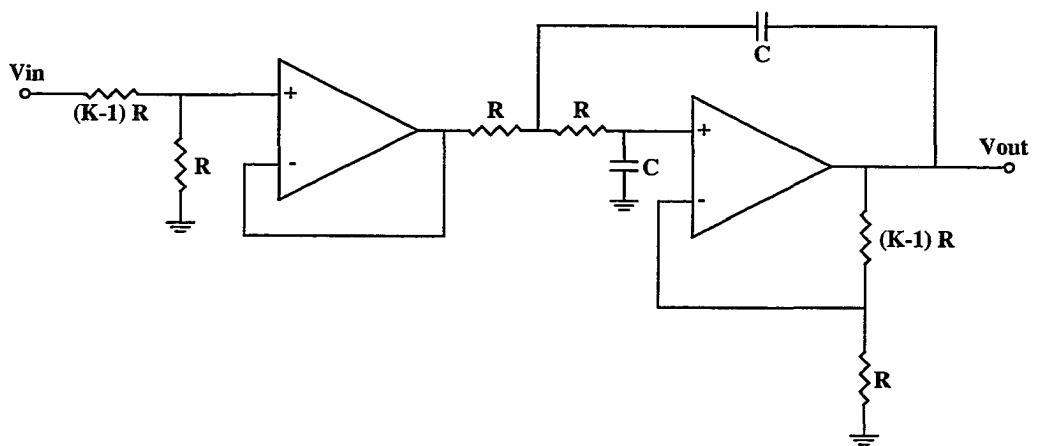


Figure 2.16: Improved lowpass filter.

buffer was used to isolate the powered electrode from the filter.

CHAPTER 3

Dynamic Modeling of the Plasma Generation Process

In the traditional control of plasma etch tools very few process characteristics are regulated in real time. While the quality of the etch is determined by the etch characteristics presented in Section 1.1.2, real-time *in situ* measurement of these characteristics is difficult (if not impossible). Therefore, these etch characteristics cannot be used to control the etching process; instead, process recipes are often specified only in terms of equipment setpoints. These setpoints affect the etch characteristics only indirectly through the plasma properties. In some sense, the process engineer is handicapped in that there is only access to equipment inputs, rather than plasma parameters. As the plasma characteristics strongly influence the etch properties, controlling the plasma generation process has the potential for improving the quality of the etch. This forms the basis for the control strategies pursued in this research.

3.1 Control-Oriented Decomposition and Control Strategy.

We begin by “conceptually” decomposing the etch into two separate, but interacting, processes: the plasma generation process (PGP) and the wafer etch process (WEP). This

decomposition is shown graphically in Figure 3.1. These sequential processes separate the generation of the important chemical and physical species from the action of etching the surface of the wafer. The inputs to the PGP are the various equipment settings (*e.g.* throttle position, gas composition and flow rates, and applied power); the outputs are the key plasma parameters that are responsible for etching (*e.g.* V_{bias} , pressure, ion flux, and the concentration of neutral radicals and polymer precursors¹). The WEP is driven by these plasma parameters and has as outputs the characteristics crucial to etch performance. This decomposition actually represents a physical separation: the PGP represents the bulk plasma, the WEP represents the wafer surface phenomena, and the interface between them is the sheath. It is important to note that there does exist a certain amount of feedback coupling from the wafer surface to the plasma (see, for example, the loading effect in Section 4.2.1). The wafer itself is therefore a disturbance to the plasma generation process.

It is desirable to control the five plasma characteristics shown in Figure 3.1. While there are well established methods of measuring both V_{bias} and pressure, custom sensors are necessary for the measurement of the other characteristics. Unfortunately, of these characteristics, we are presently only able to estimate the concentration of the fluorine radicals. Separate research projects are underway to measure ion current (flux) through rf electrical measurements and polymer precursors using optical emission spectroscopy. For the rest of this dissertation, control of plasma parameters will be limited to V_{bias} , pressure, and fluorine concentration ([F]).

The above decomposition of the RIE leads to our control structure. The key idea is to regulate the inputs to the WEP by precisely controlling the outputs of the PGP. This is accomplished by designing a real-time controller for the PGP as shown in Figure 3.2.

¹It is actually the flux of these species to the wafer surface that affects the etching process. However, as was shown in Section 1.2.2, the flux of each species is closely related to its concentration in the bulk plasma.

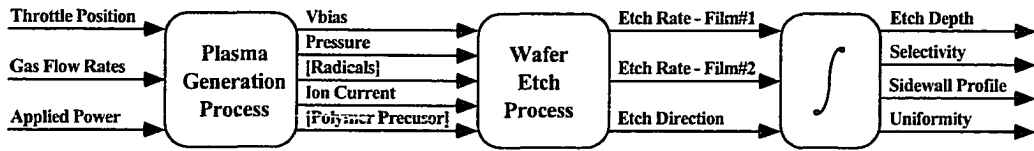


Figure 3.1: Conceptual decomposition of the RIE process.

Future research is expected to include the development of a controller around the WEP and a supervisory level controller. The WEP controller will translate desired etch characteristics into setpoints for the PGP control system. The supervisory controller will perform the high-level cell control functions that include on-line monitoring, diagnostics, and failure recovery as well as post-process analysis of the data for the purposes of sequential optimization, quality control, and so forth. At present, only the PGP controller has been implemented.

There are many merits to this approach:

- With existing sensor technology, it is very difficult to measure the key wafer etch parameters (selectivity, anisotropy, etc.) in real time during the etch process. (Some of these can be measured in near-real-time.) Therefore, for real-time feedback control, an indirect strategy is necessary.
- Modeling of the etch characteristics is the most difficult part of the problem. With this controller structure, the modeling task may become more tractable. The model for the PGP can be developed first, leading to the development of the real-time plasma controller. Then the modeling task for the WEP would involve relating the effects of the key plasma parameters on the etch performance, which is much more direct than trying to build a single model from the equipment inputs to the etch characteristics.
- The switch from specifying the process recipes in terms of [throttle position, flow rates,

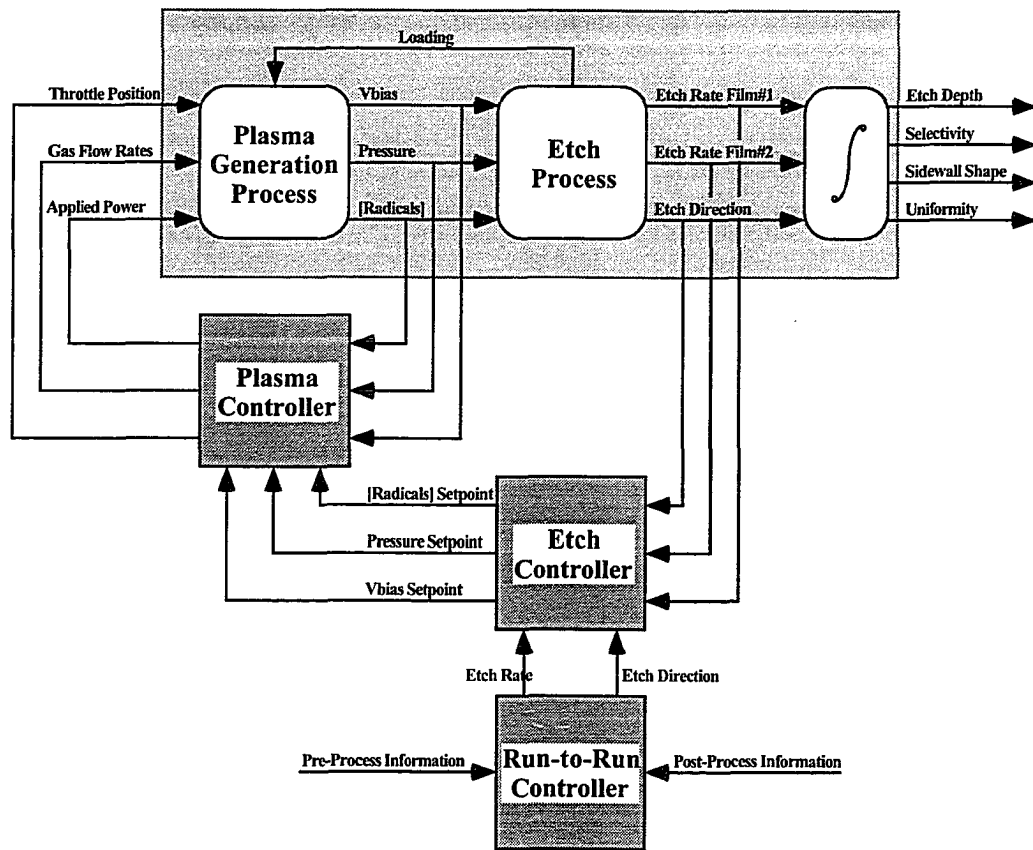


Figure 3.2: Feedback control strategy for the reactive ion etching process.

power] to [V_{bias} , pressure, fluorine concentration] is a significant change of viewpoint. As was seen in Section 1.2.2, these new setpoints are, in many ways, more directly connected to the overall etch performance; tightly regulating them should eliminate much of the variance seen in plasma systems. Using plasma characteristics as setpoints may also facilitate the exchange of process recipes between different systems.

3.2 System Identification of the Plasma Generation Process

The PGP controller is based upon a dynamic model of the plasma generation process. While the PGP is highly nonlinear, a linear model was desired to allow the use of linear control design techniques. Thus, instead of modeling the process dynamics over a wide range of operating conditions, a model was developed that captured the process dynamics in a small region around a give operating point. Two major factors in choosing this operating point were that the etching was in an RIE regime (both chemical and physical) and that the actuators have good authority over the plasma properties. Roughly, the AME-8300 is in an RIE regime for pressures below 50 mTorr and power above 500 W.

The nonlinear nature of the throttle valve made it difficult to determine *a priori* its region of highest authority. In the next section, the procedure for determining the throttle settings at which the throttle valve has maximum authority as an actuator is described. This throttle position, along with the CF_4 flow rate required to make pressure approximately 20 mTorr and a power of 1000 W, defined the operating point used for the modeling of the plasma generation process.

3.2.1 Conductance Through the Throttle Valve

The throttle valve is nonlinear in nature and has different levels of authority at various throttle positions and chamber pressures. Therefore, a set of experiments was devised to find an operating region where the valve was most effective in influencing the pressure.

First, the chamber was sealed from the pump stack by closing the turbo gate valve. The chamber was then filled with CF₄ to approximately 85 mTorr, after which the CF₄ flow was shut off. The throttle was then set to the desired position; experiments were run at throttle positions

$$\theta = [2.5, 5.0, 7.5, \dots, 22.5, 25.0] \text{ (% Open).} \quad (3.1)$$

Finally, the turbo gate valve was opened and the pressure was monitored as the chamber was pumped out. A plot of pressure vs. time for the throttle setting $\theta = 12.5 \text{ %Open}$ is shown in Figure 3.3.

Flow can be expressed in terms of a volume per unit time

$$\frac{dV}{dt} = \frac{dn}{dt} \frac{RT_{STP}}{P_{STP}}, \quad (3.2)$$

where $\frac{dn}{dt}$ is the change in moles of CF₄ per unit time, R is the universal gas constant, T_{STP} is standard temperature (298 °K) and P_{STP} is standard pressure (760 Torr). The slope of the pressure curve from Figure 3.3 (shown in Figure 3.4) is related to $\frac{dn}{dt}$ by

$$\frac{dn}{dt} = \frac{dP}{dt} \frac{V_{cham}}{RT_{STP}}, \quad (3.3)$$

where V_{cham} is the volume of the chamber. Thus, the flow through the throttle valve can be found from

$$\frac{dV}{dt} = \frac{dP}{dt} \frac{V_{cham}}{P_{STP}}. \quad (3.4)$$

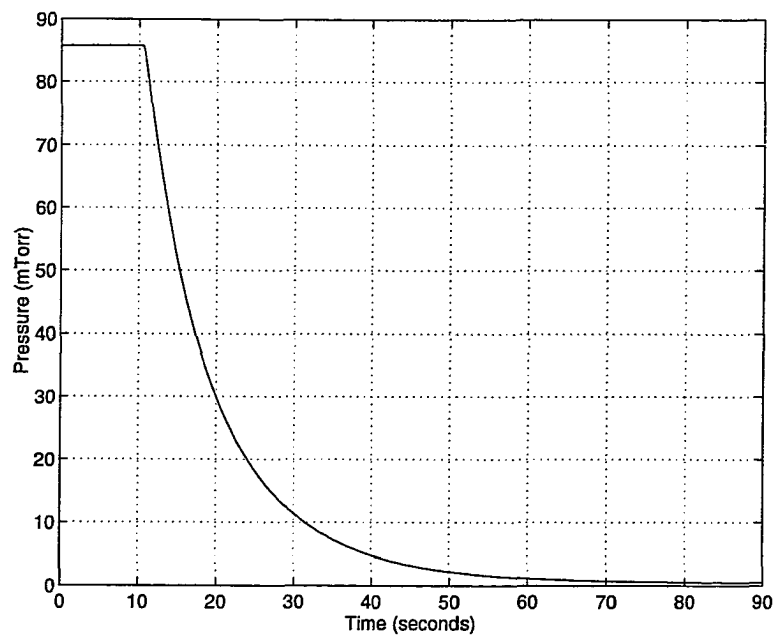


Figure 3.3: Pressure response during conductance experiment.

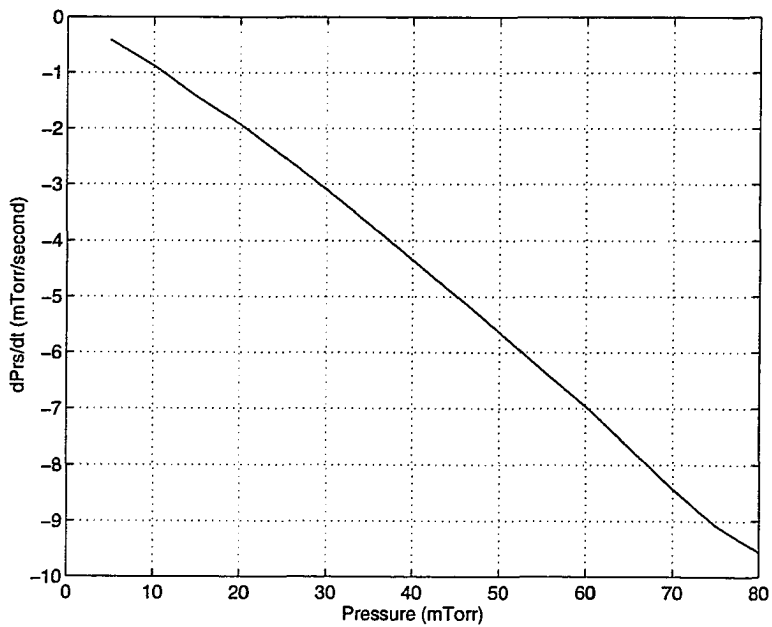


Figure 3.4: dP_{rs}/dt vs. pressure during conductance experiment.

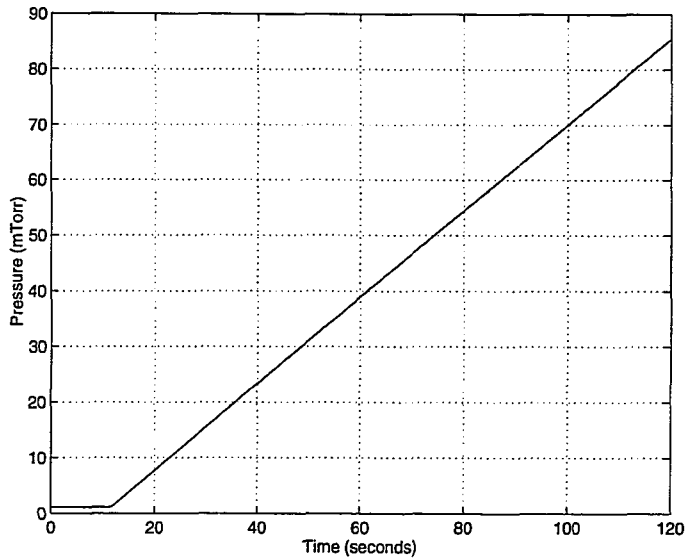


Figure 3.5: Pressure response during volume experiment with a Ar flow of 14 sccm.

All that remained was to find the volume of the chamber. This was found by isolating the chamber from the pumping stack and measuring the pressure rise at a fix flow rate. The throttle valve could not be used to isolate the chamber, because there is a small (but significant for this experiment) amount of leakage when the valve is fully closed. However, on the AME-8300 there is a turbo gate valve directly above throttle valve; this valve is effective at shutting off flow out of the chamber and was thus used. The throttle valve and the turbo gate valve are very close together, thus using the gate valve does not significantly change the chamber volume. The response of the pressure during this experiment is shown in Figure 3.5.

From this data, the pressures P_1 and P_2 were recorded at times t_1 and t_2 , respectively.

From the flow rate (flw), the standard volume² of gas added (V_{added}) was calculated,

$$V_{added} = flw \times \Delta t, \quad (3.5)$$

where $\Delta t = t_2 - t_1$. One mole of gas at standard temperature and pressure occupies a volume of $22.4 \times 10^{-3} \text{ m}^3$ [110]. Next, the number of moles added (Δn) was computed by

$$\Delta n = \frac{V_{added}}{22.4 \times 10^{-3} \text{ m}^3}. \quad (3.6)$$

This allowed the volume of the chamber (V_{cham}) to be determined by

$$V_{cham} = \frac{\Delta n RT}{\Delta P}, \quad (3.7)$$

where $\Delta P = P_2 - P_1$. From this experiment, the chamber volume was calculated to be

$$V_{cham} = 0.211. \quad (3.8)$$

This value was verified by repeating the experiment with different flow rates and gases.

Finally, the flow through the throttle valve was calculated using Equation 3.2. Figure 3.6 shows this flow vs. various throttle positions and pressures. From this figure it is seen that the throttle valve has the most authority at settings between 12.5 and 15.0 %Open. It was determined that for a throttle position of 12.5 %Open, a CF_4 flow rate of 30 sccm yielded a chamber pressure of 20 mTorr. This operating point was used to develop the model for the plasma generation process and is given again in Table 3.1.

3.2.2 Dynamic Model

The feedback controller design was based on a dynamic model of the plasma generation process. There are several different models that can be used to represent these dynamics. First principle models, such as [64], have the potential of providing a detailed physical

²The volume of gas is measured at standard pressure (760 Torr) and temperature (298°K).

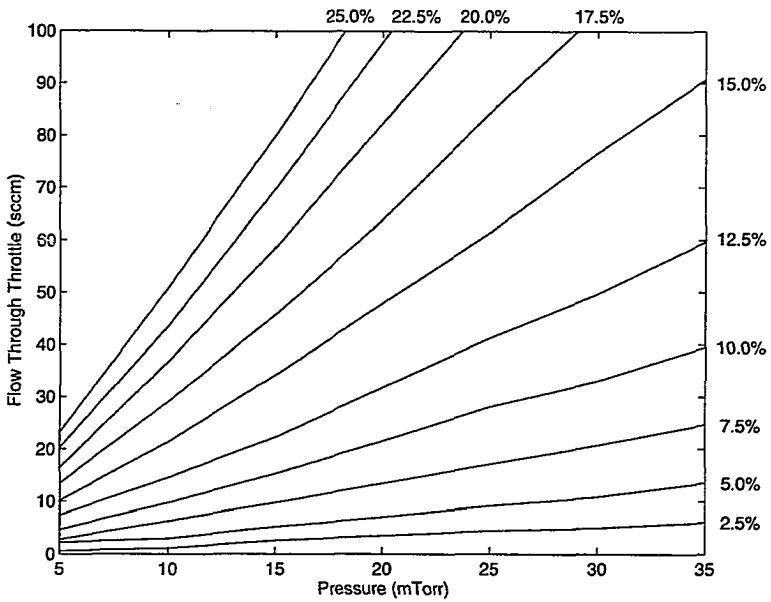


Figure 3.6: Flow through the throttle valve vs. pressure and throttle position.

description of the system. Unfortunately, the modeling of plasma and surface reactions is very complex and these models are not well suited for use in real-time feedback control. Another approach is to empirically develop models with input-output data from the system. These models, while easy to develop, only apply to the reactor from which the data was collected. In addition, these models provide little insight into the underlying mechanisms of the process [12]. Many empirical models of plasma etching processes (see, for example, [2, 3, 57]) only give a static relationship between equipment inputs and etch characteristics. Those used for real-time feedback control need to be dynamic in nature. Between these two extremes are phenomenological models [15]. Phenomenological models attempt to capture only the dominant physical mechanisms and are often empirically tuned to a specific reactor or process.

In this research, I have primarily used empirical models of the plasma generation process. The fluorine concentration estimate was based on the physics presented in Section 2.1.3.

Throttle Position	12.5 %Open
CF ₄ Flow Rate	30 sccm
Applied Power	1000 W

Table 3.1: Operating point for the plasma generation process model.

However, the estimate itself was empirically related to the inputs of the plasma generation process. The PGP model was based on input-output data collected by separately applying steps to the inputs of our reactor. In the rest of this chapter, I present the procedure through which this model was developed.

The initial goal of the control strategy was to use throttle position, CF₄ flow rate, and power to control the three plasma parameters as shown in Figure 3.2. In order to independently set the steady-state values for all of these properties, the dc gain matrix between the equipment inputs and plasma characteristics must be invertible. This dc gain matrix was found by separately changing each actuator settings allowing the system to settle, and taking the ratio of the change in each plasma property to the change in the input. For the plasma generation process the dc gain matrix had the following form³

$$\begin{bmatrix} V_{bias} \\ \text{Pressure} \\ [F] \end{bmatrix} = \begin{bmatrix} 0.330 & -0.254 & 0.740 \\ -1.000 & 1.460 & 0.000 \\ 0.246 & 0.205 & 1.760 \end{bmatrix} \begin{bmatrix} \text{Throttle Position} \\ \text{CF}_4 \text{ Flow Rate} \\ \text{Power.} \end{bmatrix}. \quad (3.9)$$

The invertibility of this matrix is measured by its condition number κ . The condition number is the ratio of the largest to smallest singular value of the matrix⁴. The singular

³The original dc gain matrix upon which conclusions were drawn was not available at the time of writing of this dissertation. Therefore, presented here is a similar dc gain matrix that was recently collected by Oliver Patterson.

⁴For a complete description of singular values and matrix condition numbers see [54].

values for the dc gain matrix were

$$\sigma = \begin{bmatrix} 1.966 & 1.785 & 0.004626 \end{bmatrix}, \quad (3.10)$$

and the condition number was

$$\kappa = 425. \quad (3.11)$$

This implied that the dc gain matrix was almost singular (noninvertible) and that all three outputs could not be independently controlled. The throttle position and flow inputs are almost redundant; they both primarily affect the plasma through pressure. Of the three outputs, V_{bias} and fluorine concentration most directly affect the etch characteristics; therefore it was decided to regulate these two plasma properties with the feedback controller. The throttle valve was chosen over the flow controller as a manipulated input to the plasma generation process, because the throttle had a quicker time response and slightly higher command authority. For the remainder of this work, flow rate was held fixed at 30 sccm.

In collecting the data for the step experiments, it was noted that the fluorine concentration measurement was very noisy. One possible method to remove some of this noise is to lower the corner frequency of the lock-in filter; however this could potentially filter out some of the dynamics of the fluorine response. An alternative was to repeat the step experiment several times and average the responses together, thus improving the signal-to-noise ratio while preserving the time response of the signals. The V_{bias} and fluorine concentration responses to the steps in power are shown in Figures 3.7 and 3.8. As can be seen in Figure 3.9, this averaging technique greatly improves the signal-to-noise ratio of the fluorine concentration estimate.

The step response data was then used to determine a model for the plasma generation process. This was done by separately identifying a transfer function for each of the input-

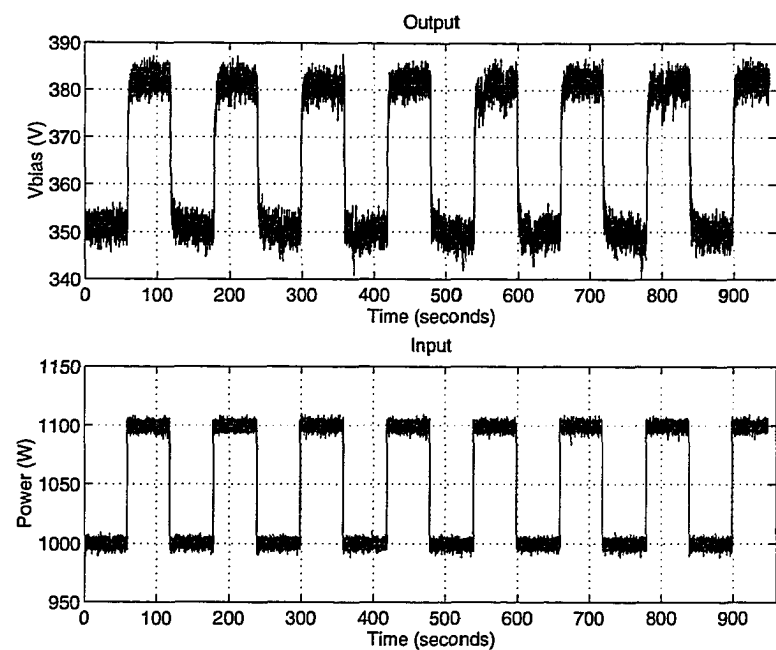


Figure 3.7: V_{bias} data from power step experiment.

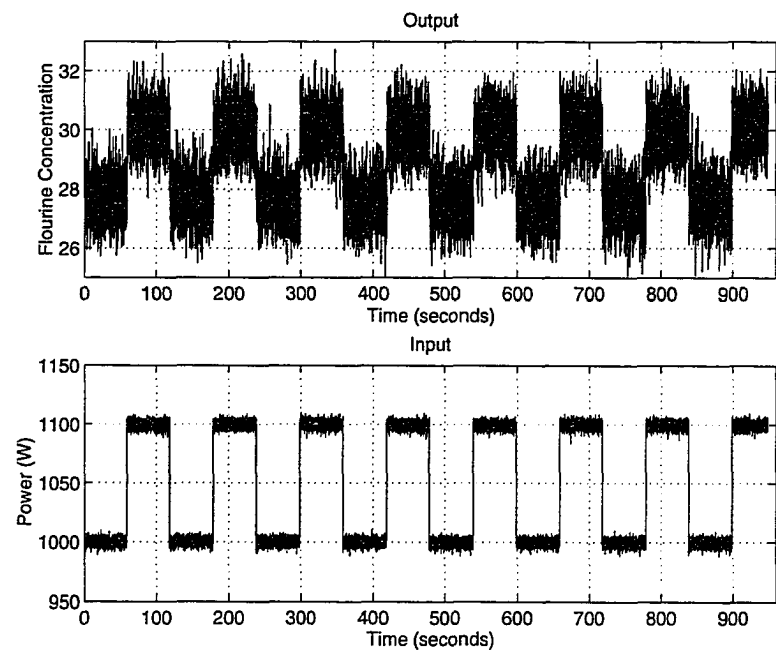


Figure 3.8: Fluorine concentration data power step experiment.

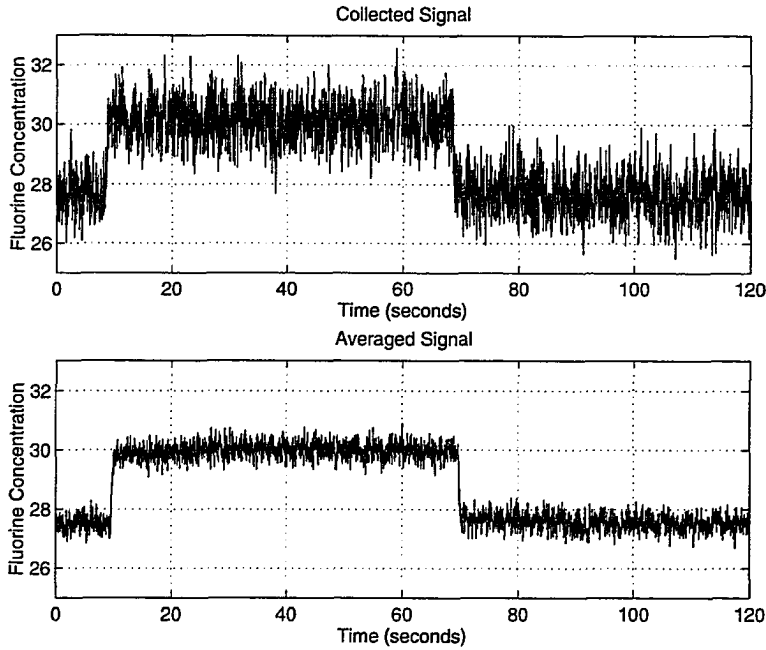


Figure 3.9: Noise reduction due to averaging of [F] signal.

output pairs. There are several different linear model structures that can be used to capture the dynamics of a system. A complete description of the various model structures can be found in [69, 98]. Each of these model structures is characterized by a number of parameters which are empirically determined through a least squares optimization; this process is known as system identification. Initially, several different model structures were compared; the Auto-Regressive Moving Average with eXogenous input (ARMAX) model provided the best fit to the experimental data and was used to model the plasma generation process. In practice, it is often useful to overparameterize the model [69]; this may lead to better fits with the experimental data. The extraneous parameters can later be removed. The system identification algorithms used in this dissertation generate discrete-time models which were then converted to continuous time for controller design.

Order	Transfer Function	DC Gain	Mean Square Error
First order	$\frac{0.3726}{s+1.195}$	0.3118	0.772
Second order	$\frac{0.6593(s+7.543)}{(s+1.085)(s+14.639)}$	0.3131	0.739
Third order	$\frac{0.4679(s+0.467)(s+1.9828)}{(s+0.362)(s+1.923)(s+1.9832)}$	0.3136	0.593

Table 3.2: Transfer functions from power to V_{bias} .

Power to V_{bias} Response

The goal was to identify transfer functions that capture local process dynamics around the operating point given in Table 3.1. The input-output data was taken to be with respect to the corresponding operating conditions by subtracting off the mean of the signal measured before the step in the actuator. The first step in the identification of each transfer function was to visually inspect the input-output data to determine any pure time delays that existed in the response. As can be seen in Figure 3.10, the response of V_{bias} to a step in power had a delay of only one sample. The actual delay may have been less than one sample, but because the data collection was synchronized to the input step the minimum measured delay was one sample. Next, the `armax` command from the Matlab System Identification Toolbox [68] was used to identify first, second, and third order models based on the empirical data. The simulated response of each model to a step in power was compared to the actual system response. The identified transfer functions, as well as the corresponding dc gains and mean square errors between the actual and simulated responses, are given in Table 3.2.

As can be seen from this Table and the simulated step responses in Figure 3.11, the third order model had the best fit to the experimental data. The differences in the models can be seen from the Bode plots in Figure 3.12. Note that the third order model has an almost pole-zero cancelation; removing the pole-zero pair yields a second order model that

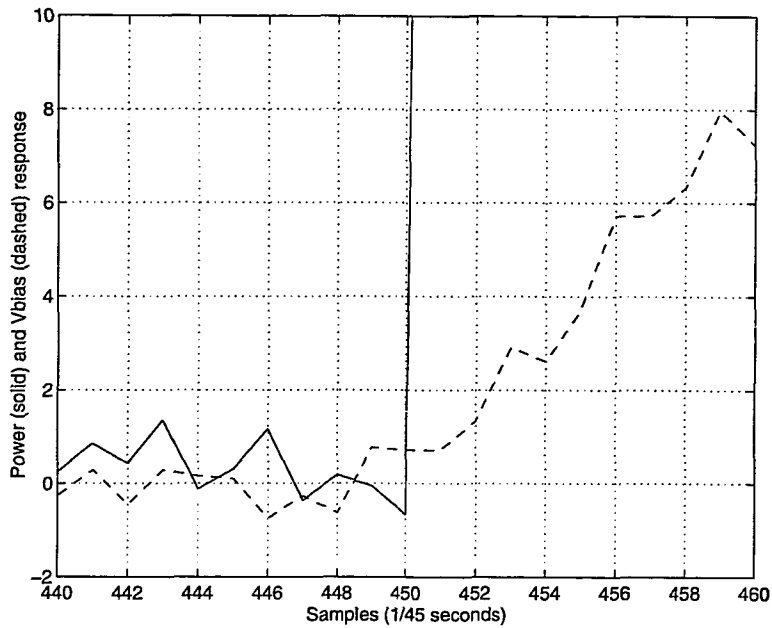


Figure 3.10: Delay in response of V_{bias} to a step in power.

fits the experimental data better than the second order model obtained directly from the identification. In principle, the second order model obtained directly should be optimal; however, the parameters of this model are obtained by the gradient search technique and thus may have converged only to a local minimum. Therefore, by removing the pole-zero pair for the third order model, the following second order transfer function for the response from power to V_{bias} was found to be

$$G_{vp}(s) = \frac{0.468(s + 0.467)}{(s + 0.362)(s + 1.923)}. \quad (3.12)$$

Power to Fluorine Concentration Response

Next, the transfer function for the response from power to estimated fluorine concentration was identified. As with the response of V_{bias} to this input, the fluorine concentration also responds with a delay of only one sample. This can be seen in Figure 3.13. The **armax**

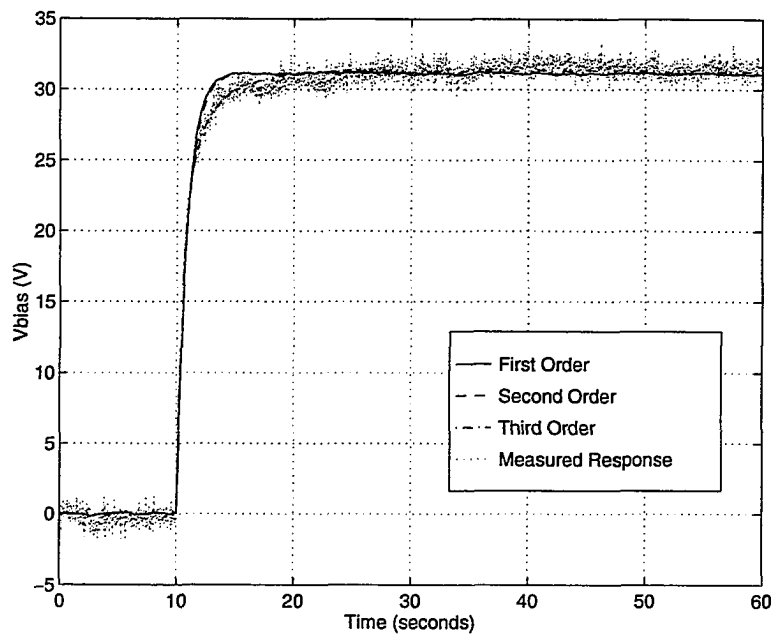


Figure 3.11: Step response: Power to V_{bias} .

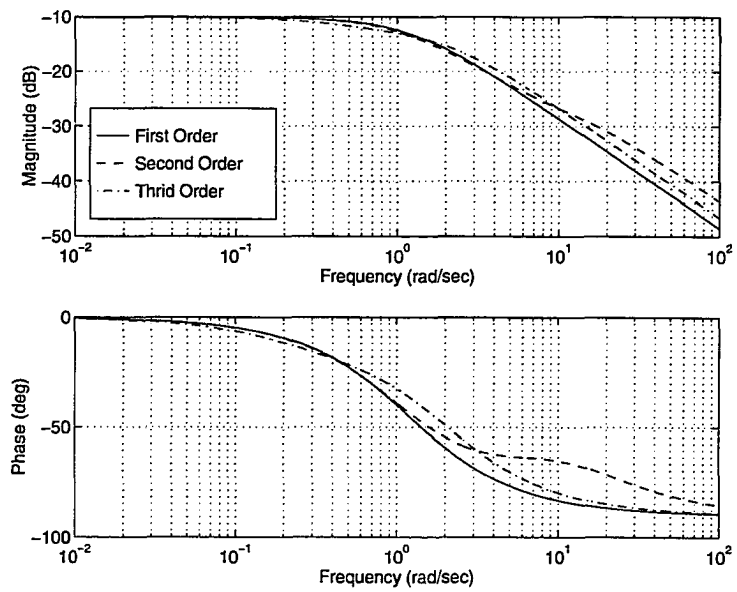


Figure 3.12: Bode plot: Power to V_{bias} .

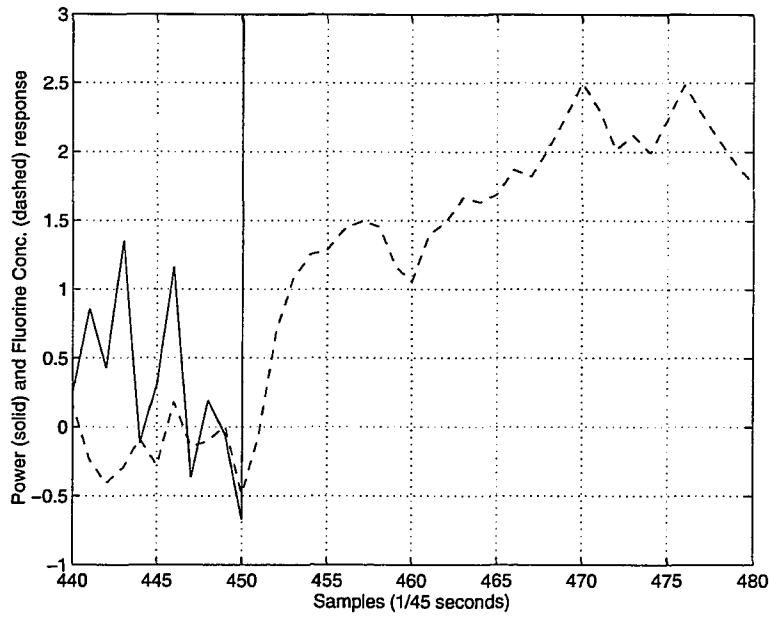


Figure 3.13: Delay in response of fluorine concentration to a step in power.

Order	Transfer Function	DC Gain	Mean Square Error
First order	$\frac{0.4314}{s+27.61}$	0.0245	0.248
Second order	$\frac{0.4598(s+6.275)}{(s+2.662)(s+44.07)}$	0.0246	0.230
Third order	$\frac{0.5630(s+5.54)(s+34.47)}{(s+2.48)(s+36.29)(s+48.63)}$	0.0246	0.230

Table 3.3: Transfer functions from power to fluorine concentration.

command was again used to identify first, second, and third order models; these are given in Table 3.3. A comparison of the step responses of each of these models, seen in Figure 3.14, shows that both the second and third order transfer functions do an adequate job of fitting the measured response. Indeed, as shown in Figure 3.15, the Bode plots of these models are very similar. This is a result of a near pole-zero cancelation in the third order model. It was concluded that that

$$G_{Fp}(s) = \frac{0.460(s + 6.28)}{(s + 2.66)(s + 44.07)}. \quad (3.13)$$

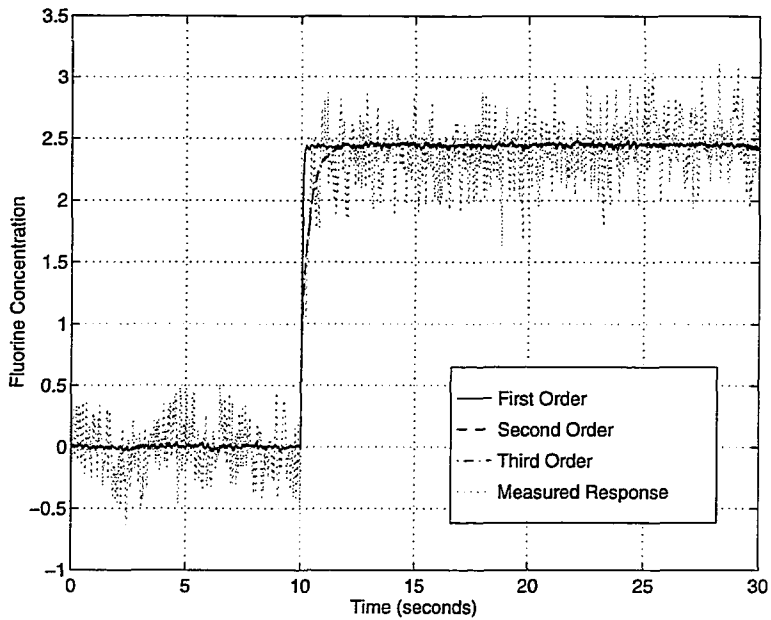


Figure 3.14: Step response: Power to fluorine concentration.

was an adequate representation of the response fluorine concentration to a step in power. Though the pole at -44.07 has no significant effect on the response, it is retained to keep the transfer function strictly proper. This simplifies the controller design by providing a model with no direct feedthrough term.

Throttle Position to V_{bias} Response

The response of the system to a step change in throttle position was identified next. Determining the pure time delay for this response was more difficult than in the previous cases. There was a gradual initiation in the response and this coupled with noise made it difficult determine the time delay. Therefore to assist in calculating this delay, a line was drawn tangent to the rising slope of the response and extended back through the x-axis, as shown in Figure 3.16. From a close-up view of the region where this line intercepts the axis

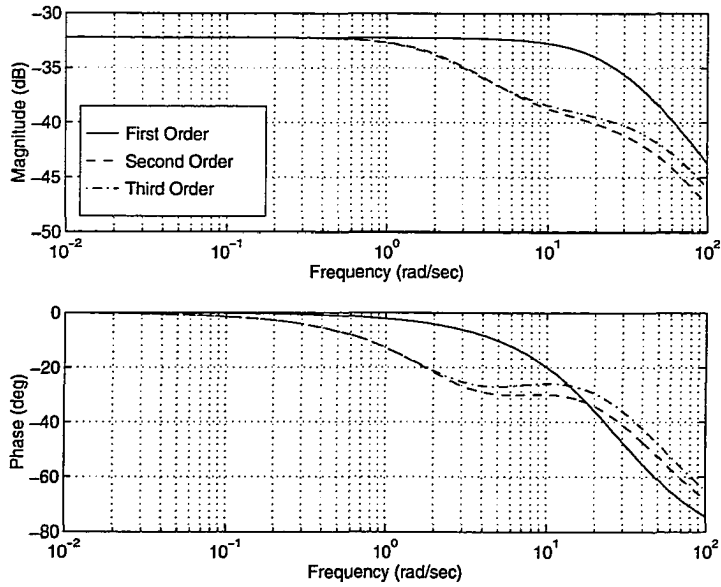


Figure 3.15: Bode plot: Power to fluorine concentration.

Order	Transfer Function	DC Gain	Mean Square Error
First order	$\frac{2.80}{s+0.174}$	16.08	0.614
Second order	$\frac{2.98(s+3.48)}{(s+0.173)(s+3.72)}$	16.08	0.618
Third order	$\frac{-0.768(s+2.35)(s-68.46)}{(s+1.75)(s+2.58)(s+16.30)}$	16.10	0.611

Table 3.4: Transfer functions from throttle position to V_{bias} .

(Figure 3.17), the delay was determined to be approximately 28 samples or 0.622 seconds.

The various order identified models are shown in Table 3.4. The dominant pole in each of these models was around $s = -0.174$. Indeed both the step responses (Figure 3.18 and Bode plots 3.19 show similar responses for all of these models. Thus, for this input-output pair the transfer function model was found to be

$$G_{vt}(s) = \frac{2.80e^{-0.622\tau}}{s + 0.174}, \quad (3.14)$$

where $e^{-0.622\tau}$ represents the time delay of $\frac{28}{45}$ seconds.

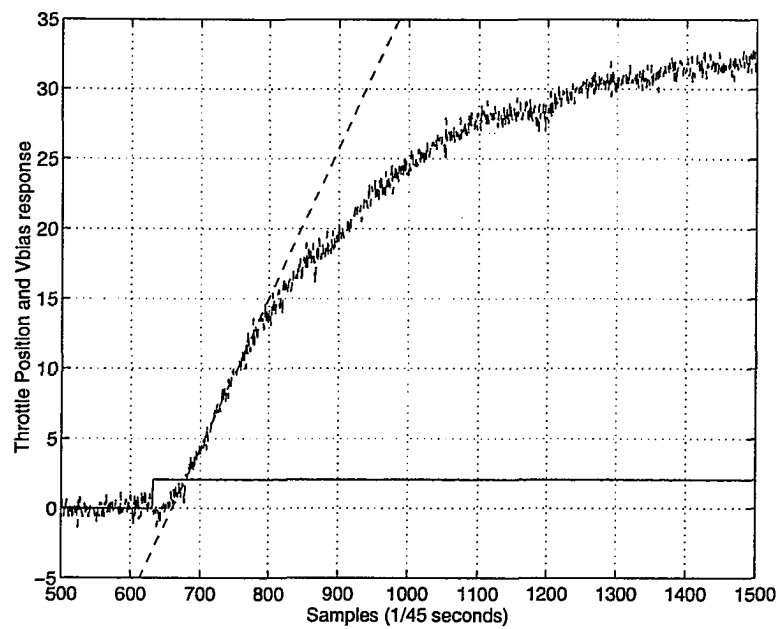


Figure 3.16: Delay in response of V_{bias} to a step in throttle position.

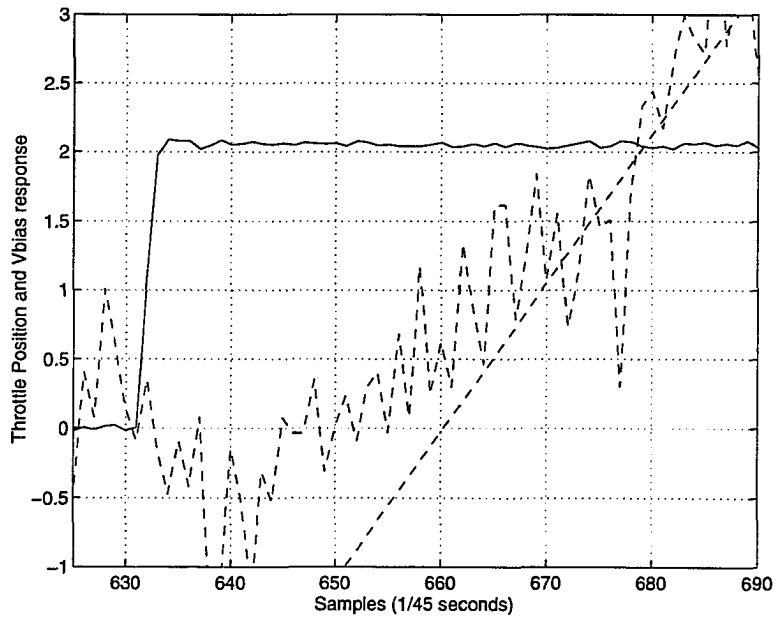


Figure 3.17: Detailed view of the delay in response of V_{bias} to a step in throttle position.

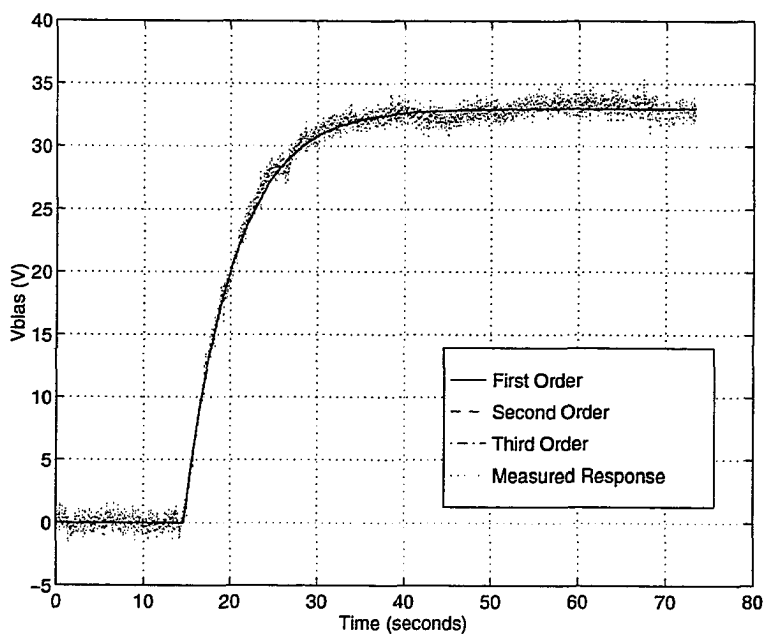


Figure 3.18: Time response: Throttle position to V_{bias} .

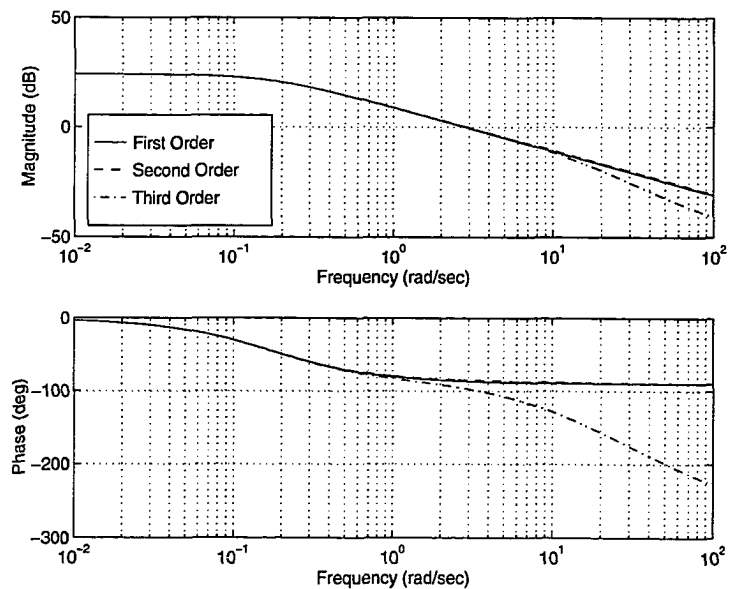


Figure 3.19: Bode plot: Throttle position to V_{bias} .

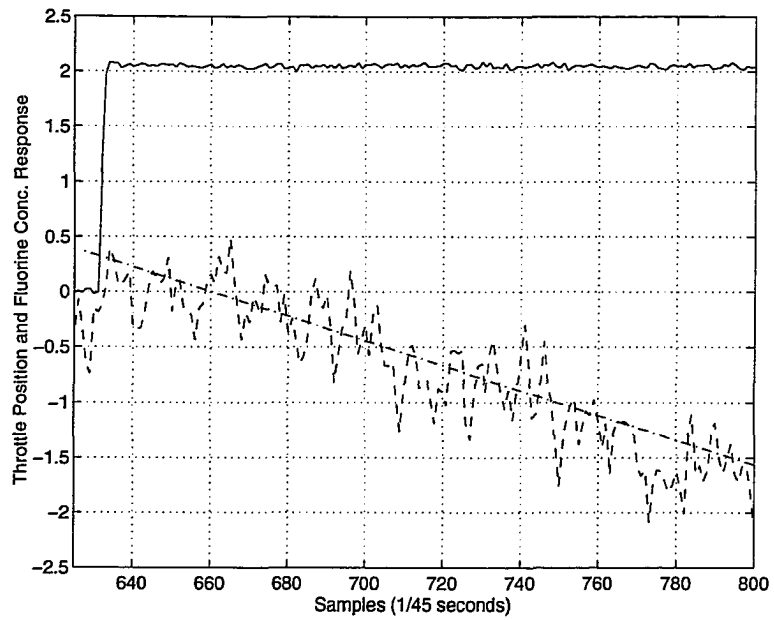


Figure 3.20: Delay in response of fluorine concentration to a step in throttle position.

Throttle Position to Fluorine Concentration Response

The final transfer function to be identified was for the response of fluorine concentration to a step in throttle position. The time delay was determined in the same manner as the one for the V_{bias} response. As is shown in Figures 3.20 and 3.21, the delay is again approximately 28 samples. The identified transfer functions are shown in Table 3.5. In this

Order	Transfer Function	DC Gain	Mean Square Error
First order	$\frac{-3.93}{s+2.03}$	-1.93	0.728
Second order	$\frac{4.03(s-3.56)}{(s+0.204)(s+33.38)}$	-2.10	0.300
Third order	$\frac{3.91(s+2.42)(s-3.61)}{(s+0.204)(s+2.39)(s+33.33)}$	-2.10	0.300

Table 3.5: Transfer functions from throttle position to fluorine concentration.

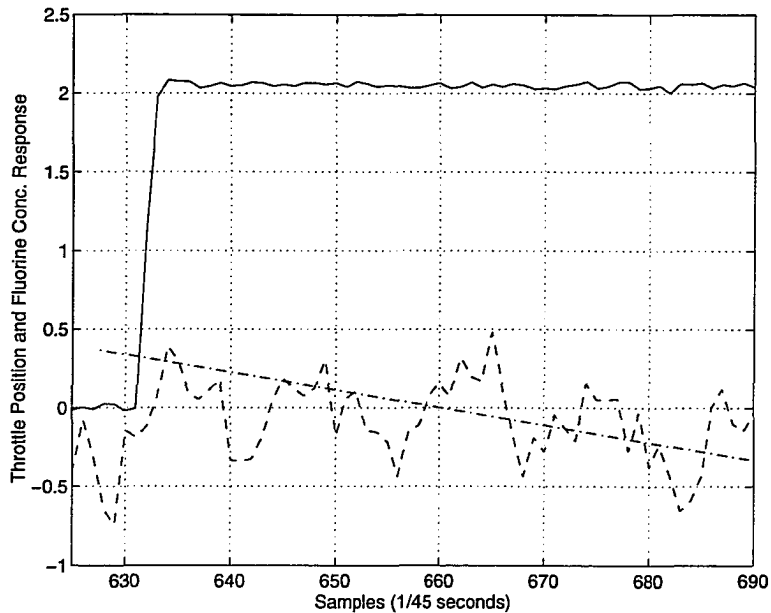


Figure 3.21: Detailed view delay in response of fluorine concentration to a step in throttle position.

case, the second and third order models accurately simulate the fluorine response. This is shown in Figure 3.23. Likewise, both of these models have similar Bode plots (Figure 3.22). In each model, the pole at $s = -0.204$ dominates the other poles and zeros. Therefore, including the time delay, the model was reduced to

$$G_{Ft}(s) = \frac{-0.428e^{-0.622\tau}}{s + 0.204} \quad (3.15)$$

Full Model

The full system was modeled by combining the four individual transfer function (Equations 3.12, 3.13, 3.14, and 3.15) into a 2×2 transfer function matrix.

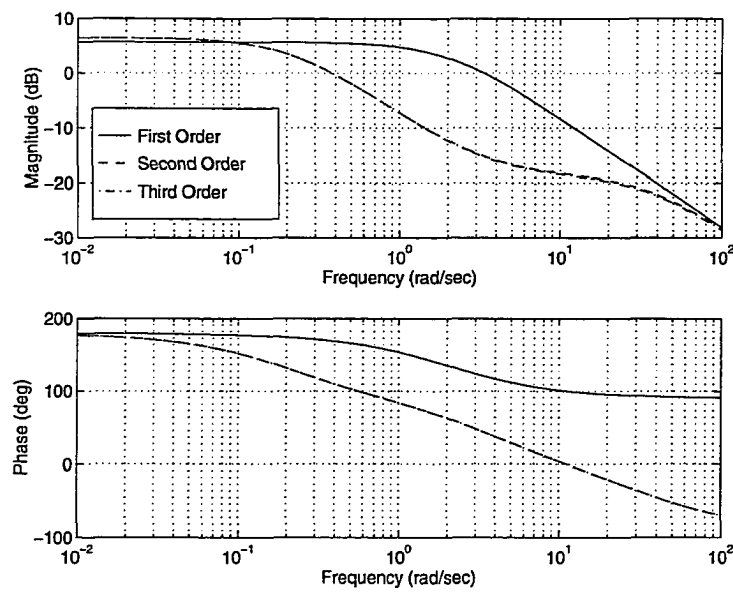


Figure 3.22: Bode plot: Throttle position to fluorine concentration.

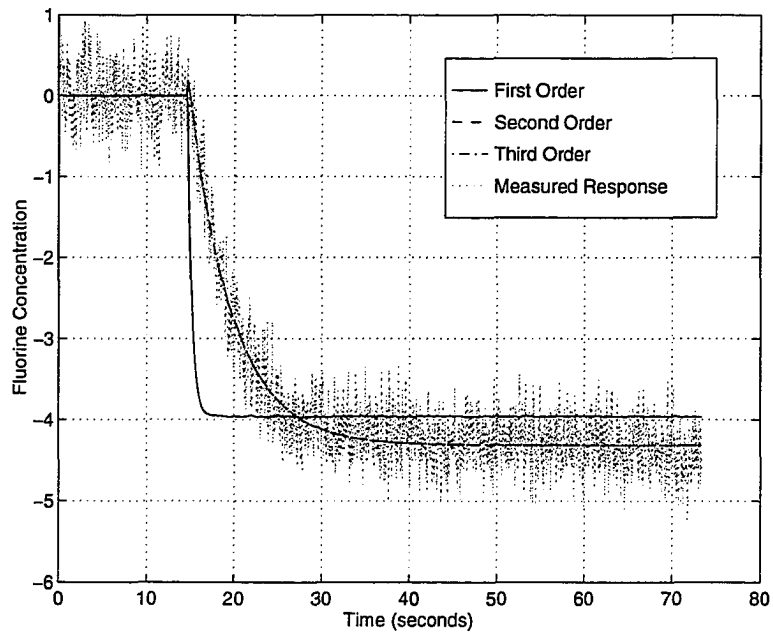


Figure 3.23: Time response: Throttle position to fluorine concentration.

$$\begin{bmatrix} V_{bias} \\ [F] \end{bmatrix} = \begin{bmatrix} \frac{2.80e^{-0.622\tau}}{s+0.174} & \frac{0.468(s+0.467)}{(s+0.362)(s+1.923)} \\ \frac{-0.428e^{-0.622\tau}}{s+0.204} & \frac{0.460(s+6.28)}{(s+2.66)(s+44.07)} \end{bmatrix} \begin{bmatrix} \text{Throttle Position} \\ \text{Power} \end{bmatrix} \quad (3.16)$$

3.3 Model Validation

In order to determine if the 2×2 transfer function model was a good approximation of the physical system, an experimental test was performed. The model was identified by exciting the system with only one actuator at a time; in the real system, it is of course possible to vary both the throttle position and power simultaneously. In principle, our linear model should predict the response to small simultaneous variations in the actuators with the same fidelity as it predicts the response to individual variations. In practice, however, the model may fail to accurately describe the system response due to neglected nonlinearities. To test the fidelity of our model's ability to describe simultaneous actuator variations, two simultaneous pseudo random binary signals (PRBS) [98] were applied to the actuators; these are shown in Figure 3.24. The PRBS applied to the throttle position was given a slower switching rate because the dynamics associated with the throttle were slower than those associated with the power input. The response of the model and the actual system, as well as the error between them, is plotted in Figure 3.25 for the V_{bias} signal. As can be seen from this plot, except for a small bias in the response, the model accurately represents the dynamics of the system; a tentative explanation for this bias is that it is due to nonlinearity. A similar comparison for fluorine concentration is shown in Figure 3.26. In this case the resulting error shows very little bias, though the signal-to-noise ratio is very poor.

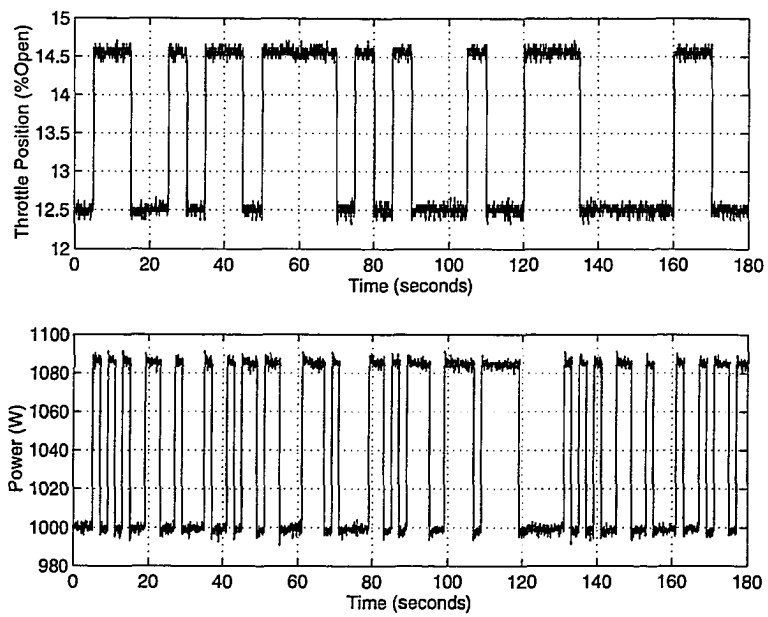


Figure 3.24: PRBS applied in model validation experiment.

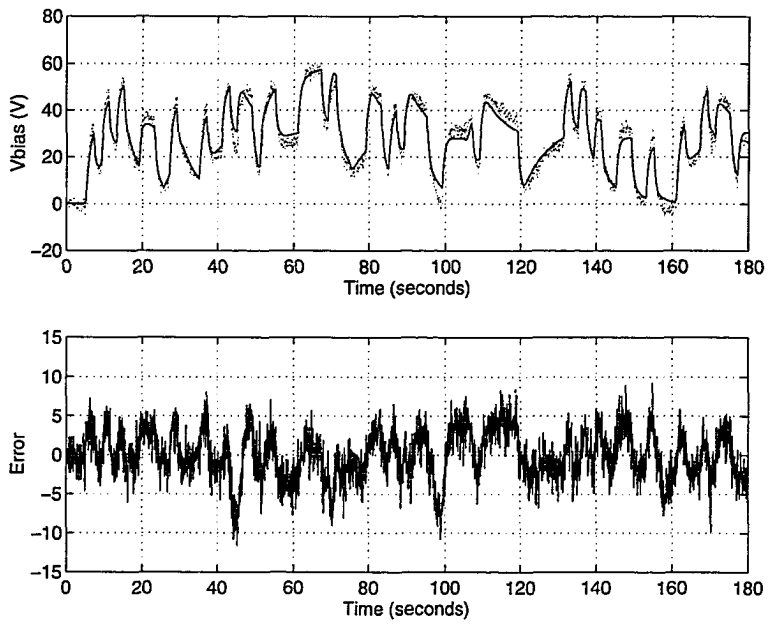


Figure 3.25: Comparison of actual and simulated V_{bias} response to simultaneous PRBS inputs.

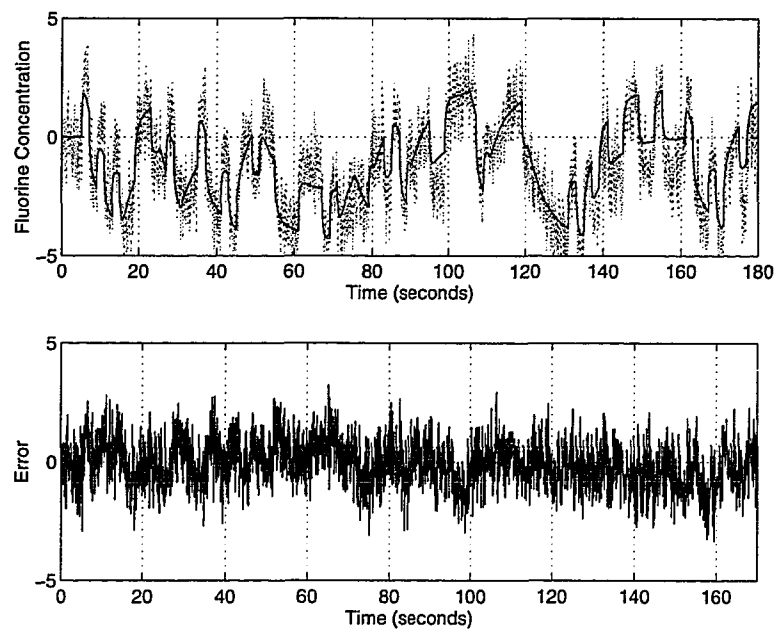


Figure 3.26: Comparison of actual and simulated fluorine concentration response to simultaneous PRBS inputs.

CHAPTER 4

Etch Rate Control and Disturbance Rejection

The principle aim of this research was to show how modern real-time control techniques can be used to improve the quality of the reactive ion etching process. It was based on the hypothesis that regulating plasma properties, instead of simply setting equipment inputs, provides tighter control of important etch characteristics. In this chapter, the ability of this control strategy to attenuate the effect of exogenous perturbations on etch rate was explored. First, a controller for the plasma generation process was designed based upon the dynamic model developed in Section 3.2. This controller allowed the operator to specify process condition in terms of plasma properties (V_{bias} and fluorine concentration), as opposed to the standard industrial practice of only using feedback control to regulate pressure (in this case, gas flow rates and applied power are set to constant values). The PGP controller is then compared to standard practice in its ability to reject disturbances to etch rate.

4.1 Plasma Generation Process Controller

The plasma generation process controller was designed to regulate the plasma properties by manipulating the inputs to the AME-8300. It was desired that the plasma setpoints be

held at constant values during the etch; therefore, the controller was designed to have zero steady-state error in tracking constant reference signals. At the process conditions used for this research, the duration of a typical etch was at least 900 seconds. It was decided that a settling time of approximately 25 seconds was sufficient for an etch of this length.

In meeting these performance objectives, there were a number of constraints that limited the bandwidth of the controller. These included the time delay in the response of the system to changes in the throttle position, the noise on the fluorine concentration estimate, and the throttle nonlinearity. Of these, the throttle nonlinearity was dominant and thus the overshoot in the throttle valve response was limited to 20%.

4.1.1 Controller Design

The design of the plasma generation process controller was done using a state space representation¹ of the transfer function matrix from Equation 3.16. The pure time delay in the system's response to changes in throttle position was represented by a Padé approximation. Both first and second order approximations were compared. The controller bandwidth was expected to be below 1 radian/second. Since, as shown in Figure 4.1, the phase lag of both approximations was similar out to the expected controller bandwidth, it was decided that the first order approximation was sufficient. Therefore, the delay was represented as

$$e^{-s\tau} \approx \frac{-\frac{\tau}{2}s + 1}{\frac{\tau}{2}s + 1}. \quad (4.1)$$

Using this approximation, a Simulink² model of the dynamics from throttle position and power to V_{bias} and $[F]$ was developed. This is shown in Figure 4.2. In order to equate changes in the inputs and outputs, each was scaled by its nominal value. For convenience,

¹In the state space representation, the system is modeled by a first order matrix differential equation. Complete details of the state space representation can be found in [17].

²Simulink is a block-diagram-based simulation package that is part of Matlab.

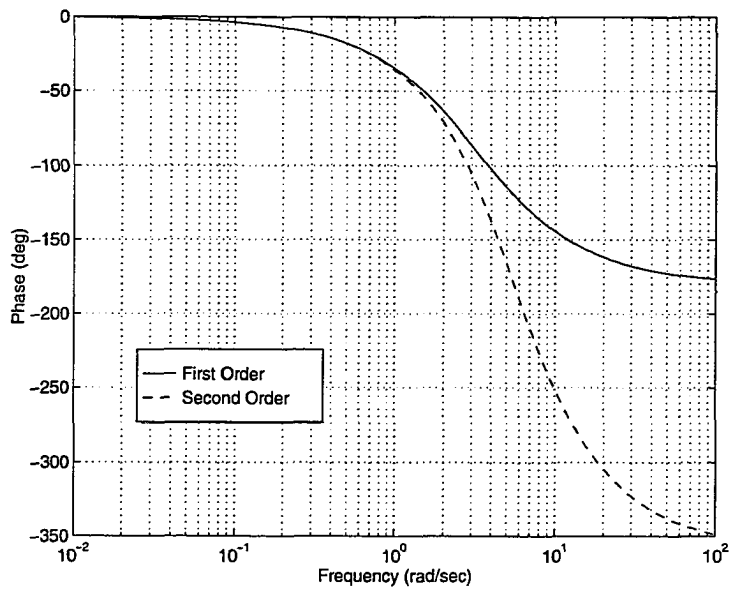


Figure 4.1: Phase lag from the Padé approximations of time delay.

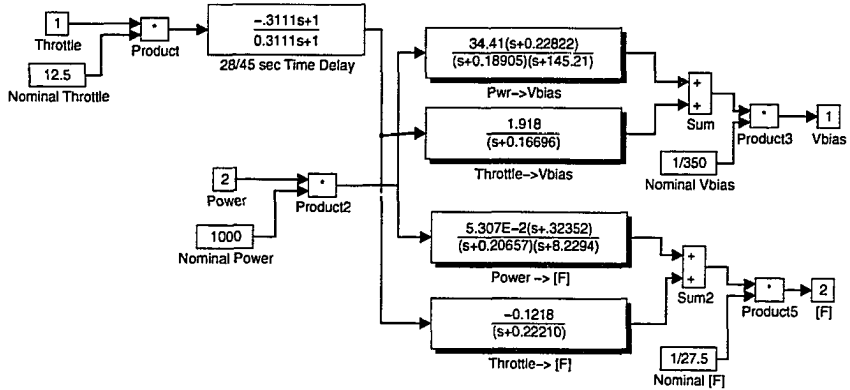


Figure 4.2: Simulink block diagram: plasma generation process model.

the Simulink command **linmod** [73] was used to create the state space representation

$$\dot{x}(t) = A_p x(t) + B_p u(t)$$

$$y(t) = C_p x(t) + D_p u(t), \quad (4.2)$$

where $u(t)$ are the process inputs, $y(t)$ are the process outputs, $x(t)$ are the states of the model, and

$$A_p = \begin{bmatrix} -8.436 & -1.304 & 0 & 0 & 0 & 0 & 0 \\ 1.304 & 0 & 0 & 0 & 0 & 0 & 0 \\ 0 & 0 & -0.2221 & 0 & 0 & 0 & 6.429 \\ 0 & 0 & 0 & -145.4 & -5.239 & 0 & 0 \\ 0 & 0 & 0 & 5.239 & 0 & 0 & 0 \\ 0 & 0 & 0 & 0 & 0 & -0.167 & 6.429 \\ 0 & 0 & 0 & 0 & 0 & 0 & -3.214 \end{bmatrix} \quad (4.3)$$

$$B_p = \begin{bmatrix} 0 & 1000 \\ 0 & 0 \\ -12.5 & 0 \\ 0 & 1000 \\ 0 & 0 \\ -12.5 & 0 \\ 12.5 & 0 \end{bmatrix} \quad (4.4)$$

$$C_p = \begin{bmatrix} 0 & 0 & 0 & 0.0983 & 0.0043 & 0.0055 & 0 \\ 0.0019 & 0.0005 & -0.0044 & 0 & 0 & 0 & 0 \end{bmatrix} \quad (4.5)$$

$$(4.6)$$

$$D_p = \begin{bmatrix} 0 & 0 \\ 0 & 0 \end{bmatrix} \quad (4.7)$$

This model of the system dynamics is known as the *plant*. For the rest of this dissertation, the time dependence will be dropped from this notation and it should be understood that the inputs u , states x , and outputs y are all functions of time. Also, since $D_p = 0$, it does not enter into the calculations presented below.

The most important performance objective was to have zero steady-state error in tracking plasma setpoints. This was accomplished by using integral control [25]. The first step in the design was to augment the system with integrators. A set of states q , equal to the integral of the error between the plant output and the desired output r , was defined by

$$\dot{q} = y - r. \quad (4.8)$$

Augmenting the system in Equation 4.2 with these states, the new plant became

$$\begin{aligned} \begin{bmatrix} \dot{x} \\ \dot{q} \end{bmatrix} &= \underbrace{\begin{bmatrix} A_p & 0 \\ C_p & 0 \end{bmatrix}}_{A_m} \begin{bmatrix} x \\ q \end{bmatrix} + \underbrace{\begin{bmatrix} B_p \\ 0 \end{bmatrix}}_{B_m} u + \underbrace{\begin{bmatrix} 0 \\ -I \end{bmatrix}}_{G_m} r, \\ y &= \underbrace{\begin{bmatrix} C_p & 0 \end{bmatrix}}_{C_m} \begin{bmatrix} x \\ q \end{bmatrix}. \end{aligned} \quad (4.9)$$

To simplify notation, we define the augmented state vector $x_m = \begin{bmatrix} x \\ q \end{bmatrix}$ and rewrite Equation 4.9 as

$$\begin{aligned} \dot{x}_m &= A_m x_m + B_m u + G_m r \\ y &= C_m x_m. \end{aligned} \quad (4.10)$$

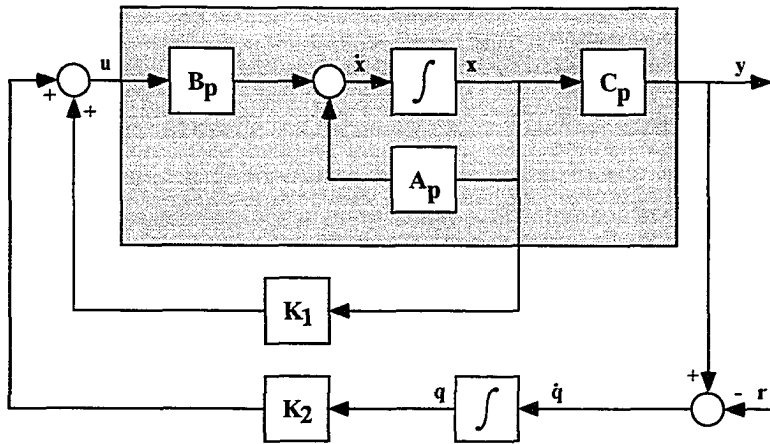


Figure 4.3: State feedback diagram.

In selecting the feedback gains, it was first assumed that the states x_m were measurable and that the controlled inputs had the form

$$u = -Kx_m, \quad (4.11)$$

where

$$K = \begin{bmatrix} K_1 & K_2 \end{bmatrix} \quad (4.12)$$

was the state feedback gain as shown in Figure 4.3. This state feedback gain was found by solving the linear quadratic regulator (LQR) problem. Briefly, in the LQR problem the controller gain K is found by minimizing the cost function

$$J = \int_0^\infty (x'Qx + u'Ru) dt, \quad (4.13)$$

subject to the system in Equation 4.10 and the control input from Equation 4.11. In this equation, Q is a matrix of weights for the states and R is a matrix of weights for the inputs. Complete details of the LQR problem can be found in [4]. In this research, the weight

matrix for the states had the form

$$Q = \begin{bmatrix} \alpha C_p' C_p & 0 \\ 0 & Q_q \end{bmatrix} \quad (4.14)$$

where α was a scalar and Q_q was a diagonal matrix of the weights for each integrator state.

The input weight matrix R was a diagonal matrix of weights for each individual input.

Applying the control inputs from Equation 4.11 to the system in Equation 4.10 yields the following closed loop system

$$\begin{aligned} \dot{x}_m &= (A_m - B_m K) x_m + G_m r \\ y &= C_m x_m. \end{aligned} \quad (4.15)$$

Parameters for the weight matrices were chosen and the closed loop system simulated to determine if the performance objectives and design constraints were satisfied. After several iterations, the following parameters were settled upon

$$\alpha = 1, \quad (4.16)$$

$$Q_q = \begin{bmatrix} 0.6 & 0.0 \\ 0.0 & 0.5 \end{bmatrix}, \quad (4.17)$$

and

$$R = \begin{bmatrix} 4.0 & 0.0 \\ 0.0 & 3.0 \end{bmatrix}. \quad (4.18)$$

The **lqr** command from the Matlab Control Systems Toolbox [40] was used to calculate the state feedback gains

$$K_1 = \begin{bmatrix} 0.000 & 0.000 & 0.006 & 0.000 & 0.001 & 0.004 & 0.019 \\ 0.000 & 0.000 & -0.002 & 0.011 & 0.001 & 0.005 & 0.004 \end{bmatrix} \quad (4.19)$$

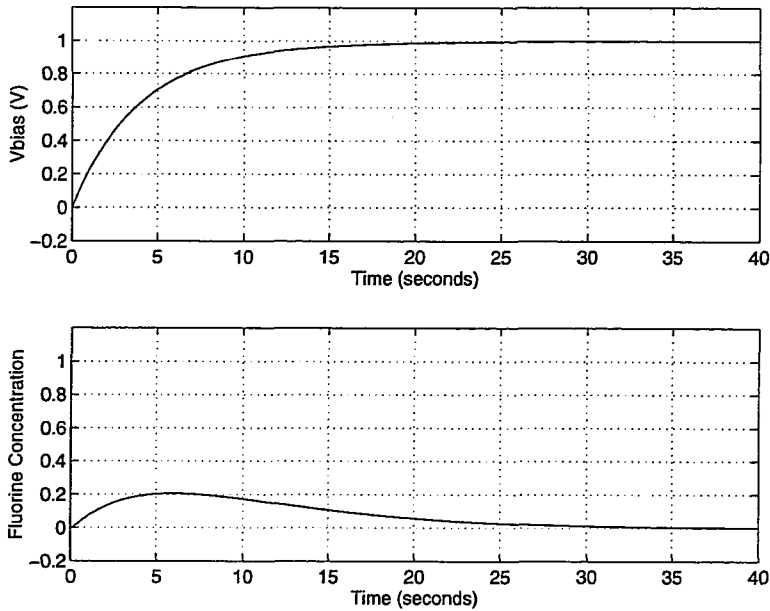


Figure 4.4: Simulated response of closed loop system to a step in V_{bias} .

and

$$K_2 = \begin{bmatrix} 0.162 & -0.321 \\ 0.406 & 0.171 \end{bmatrix}. \quad (4.20)$$

Figure 4.4 shows the simulated response of the plasma to a step change in the V_{bias} command. The corresponding responses of the actuators are shown in Figure 4.5. Likewise, the plasma and actuator responses for a step change in the fluorine concentration setpoint are shown in Figures 4.6 and 4.7.

Observer Design

In practice, the states of the system are not available for feedback, therefore they must be estimated. Actually, only the states of the plant x needed to be estimated, as the integrated error states q are calculated in the controller. The true system has disturbances

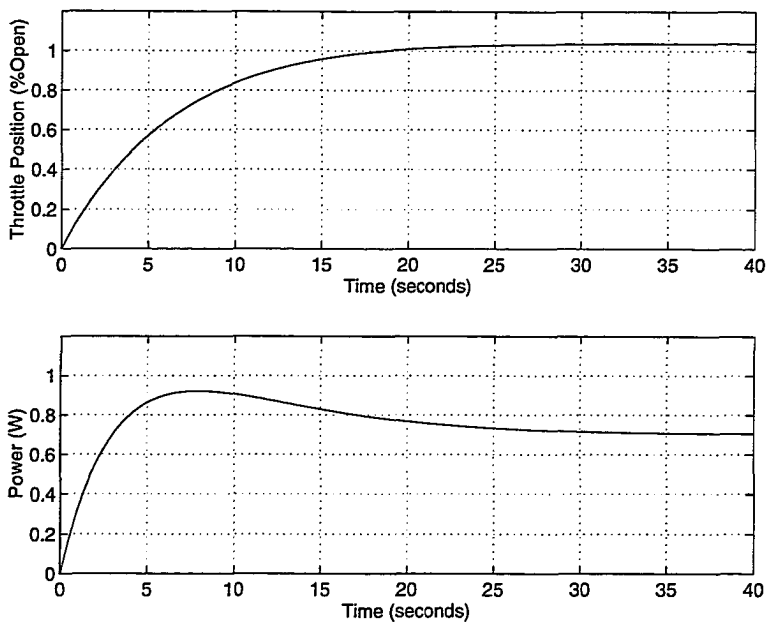


Figure 4.5: Simulated response of actuators to a step in V_{bias} .

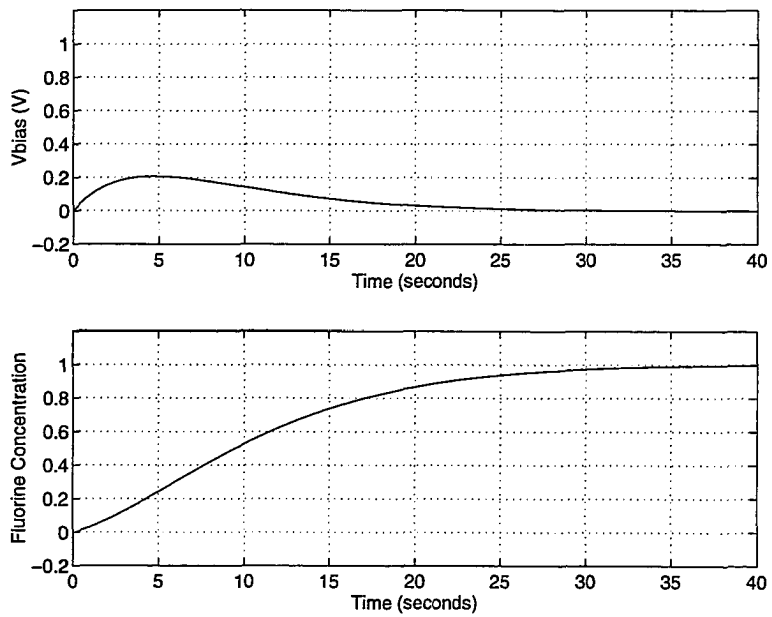


Figure 4.6: Simulated response of closed loop system to a step in fluorine concentration.

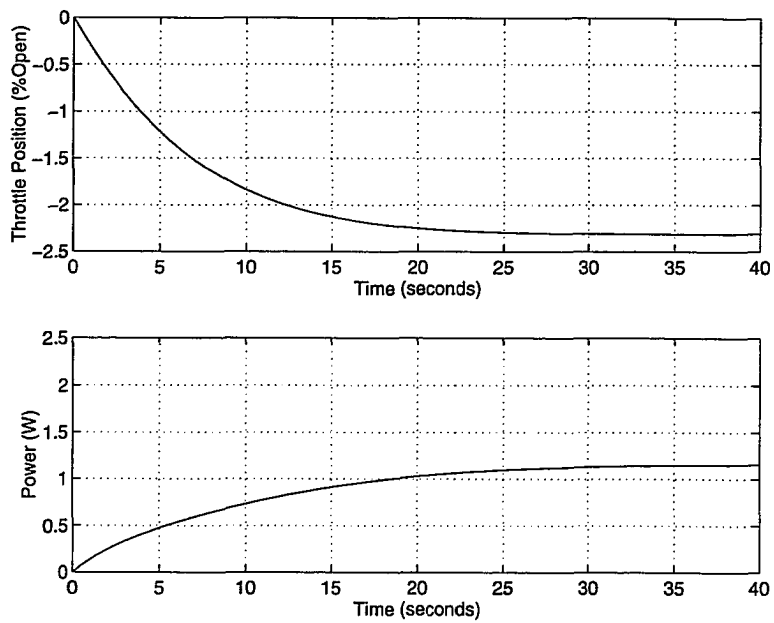


Figure 4.7: Simulated response of actuators to a step in fluorine concentration.

to the process and noise in the measurements. This was represented by

$$\begin{aligned}\dot{x}(t) &= A_p x + B_p u + v \\ y(t) &= C_p x + w,\end{aligned}\tag{4.21}$$

where v and w were assumed to be white noise. The states of this system were then estimated using an observer of the form [17]

$$\dot{\hat{x}} = A_p \hat{x} + B_p u + L' (y - \hat{y}),\tag{4.22}$$

where L' is the observer gain and $\hat{y} = C_p \hat{x}$. The LQG/LTR technique [26] was used to find the observer gain by minimizing the covariance between the actual and estimated values for the states. The `lqr` command was used again to find this gain. However, this time the LQR problem was solved for (A'_p, C'_p) where the weightings were the covariance matrices V and W , for the process and measurement noise, respectively. These matrices were assumed to have the following form

$$V = B'_p B_p\tag{4.23}$$

and

$$W = \rho I,\tag{4.24}$$

where I is the identity matrix and ρ is a scalar. For the PGP controller $\rho = 1$ was used.

Combining the observer with the state feedback gain leads to a controller of the form

$$\begin{aligned}\begin{bmatrix} \dot{\hat{x}} \\ \dot{q} \end{bmatrix} &= \underbrace{\begin{bmatrix} A_p - B_p K_1 - L' C_p & -B_p K_2 \\ 0 & 0 \end{bmatrix}}_{A_c} \begin{bmatrix} \hat{x} \\ q \end{bmatrix} + \underbrace{\begin{bmatrix} L' & 0 \\ I & -I \end{bmatrix}}_{B_c} \begin{bmatrix} y \\ r \end{bmatrix} \\ u &= \underbrace{-K}_{C_c} \begin{bmatrix} \hat{x} \\ q \end{bmatrix}.\end{aligned}\tag{4.25}$$

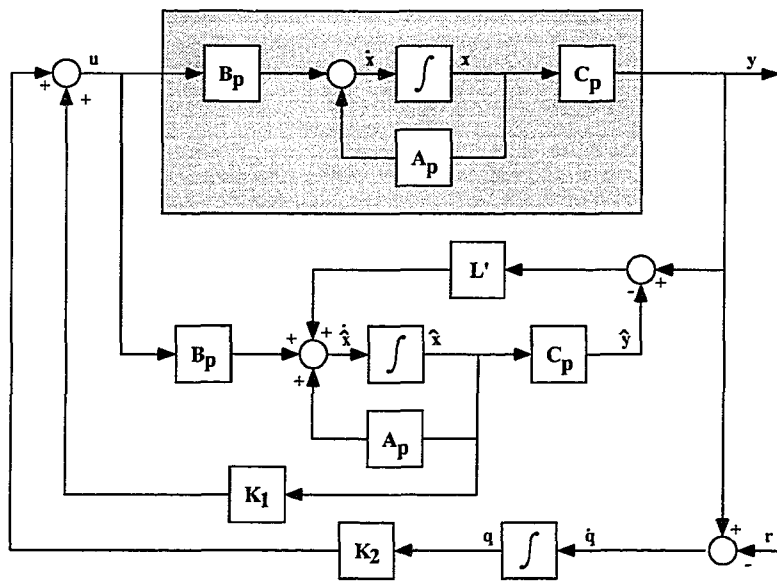


Figure 4.8: LQG/LTR closed loop system.

Defining the controller states as $x_c = \begin{bmatrix} \hat{x} \\ q \end{bmatrix}$ yields the closed loop system

$$\begin{bmatrix} \dot{x}_c \\ \dot{x} \end{bmatrix} = \begin{bmatrix} A_c & B_c C_p \\ B_p C_c & A_p \end{bmatrix} \begin{bmatrix} x_c \\ x \end{bmatrix} + \begin{bmatrix} 0 \\ -I \end{bmatrix} r,$$

$$y = \begin{bmatrix} 0 & C_p \end{bmatrix} \begin{bmatrix} x_c \\ x \end{bmatrix}. \quad (4.26)$$

The closed loop system is shown graphically in Figure 4.8. Simulations showed that this controller had virtually identical performance to the state feedback design.

Model Reduction

In order to reduce the computational complexity of the controller, states that weakly affect the input-output properties were eliminated. This is known as *model order reduction* and was done using a technique called balanced truncation. The states of the controller

were transformed from physically meaningful variables to a balanced realization. In this realization the relative effect of each state on the input-output dynamics of the controller can be examined. Details of this method of model reduction can be found in [60].

In order to transform the controller into a balanced realization, the integrator states must first be removed. The controller was therefore decomposed into two parts

$$\begin{aligned} \begin{bmatrix} \dot{q} \\ u_q \\ y \end{bmatrix} &= \underbrace{\begin{bmatrix} 0 \\ -K_2 \\ 0 \end{bmatrix}}_{A_i} \begin{bmatrix} q \end{bmatrix} + \underbrace{\begin{bmatrix} I & -I \\ 0 & 0 \end{bmatrix}}_{B_i} \begin{bmatrix} r \\ y \end{bmatrix} \\ \begin{bmatrix} \dot{x} \\ \hat{x} \\ u_q \\ y \end{bmatrix} &= \underbrace{\begin{bmatrix} A_p - B_p K_1 - L' C_p \\ -K_1 \\ I \end{bmatrix}}_{A_s} \begin{bmatrix} \dot{x} \\ \hat{x} \end{bmatrix} + \underbrace{\begin{bmatrix} B_p & L' \\ I & 0 \end{bmatrix}}_{B_s} \begin{bmatrix} u_q \\ y \end{bmatrix} \end{aligned} \quad (4.27)$$

and

$$\begin{aligned} \begin{bmatrix} \dot{x} \\ \hat{x} \\ u_q \\ y \end{bmatrix} &= \underbrace{\begin{bmatrix} A_p - B_p K_1 - L' C_p \\ -K_1 \end{bmatrix}}_{A_s} \begin{bmatrix} \dot{x} \\ \hat{x} \end{bmatrix} + \underbrace{\begin{bmatrix} B_p & L' \\ I & 0 \end{bmatrix}}_{B_s} \begin{bmatrix} u_q \\ y \end{bmatrix} \\ u &= \underbrace{\begin{bmatrix} u_q \\ y \end{bmatrix}}_{C_s} \hat{x} + \underbrace{\begin{bmatrix} u_q \\ y \end{bmatrix}}_{D_s} \end{aligned} \quad (4.28)$$

where the system $[A_i, B_i, C_i, D_i]$ was the integral portion and the system $[A_s, B_s, C_s, D_s]$ was the state feedback portion. The state feedback portion was then balanced using the **balreal** command from the Matlab Control System Toolbox. From this command, the relative effect of each state on the input-output dynamics was found to be

$$g = \begin{bmatrix} 0.2119 & 0.0610 & 0.0313 & 0.0045 & 0.0036 & 0.0006 & 0.0001 \end{bmatrix}. \quad (4.29)$$

The order of the controller was then reduced by eliminating those states corresponding to elements of g more than an order of magnitude smaller than the largest element. This was done using the **modred** command and yielded a reduced state feedback portion with three states. Incorporating the integral states back into the controller yielded

$$A_{cr} = \begin{bmatrix} -0.3297 & 0.0269 & -0.4947 & -0.0545 & 0.1201 \\ -0.1154 & -2.1648 & 14.9135 & 0.1731 & 0.0997 \\ 0.7559 & 14.7504 & -114.6750 & -0.9359 & -0.5572 \\ 0 & 0 & 0 & 0 & 0 \\ 0 & 0 & 0 & 0 & 0 \end{bmatrix} \quad (4.30)$$

$$B_{cr} = \begin{bmatrix} 0.0465 & -0.0494 & 0 & 0 \\ -0.2259 & -0.0478 & 0 & 0 \\ 0.9371 & 0.0661 & 0 & 0 \\ 1.0000 & 0 & -1.0000 & 0 \\ 0 & 1.0000 & 0 & -1.0000 \end{bmatrix} \quad (4.31)$$

$$C_{cr} = \begin{bmatrix} -0.3637 & -0.1224 & 0.4062 & -0.1612 & 0.3234 \\ -0.0865 & 0.4990 & -2.6466 & -0.4024 & -0.1707 \end{bmatrix} \quad (4.32)$$

$$D_{cr} = \begin{bmatrix} -0.0000345 & 0.0003689 & 0 & 0 \\ -0.0005203 & 0.0003663 & 0 & 0 \end{bmatrix} \quad (4.33)$$

The Bode plots of the gains of the full and reduced order controllers from V_{bias} and fluorine concentration are shown in Figures 4.9 and 4.10, respectively. As can be clearly seen, the reduced order controller has very similar input-output properties to the full order controller.

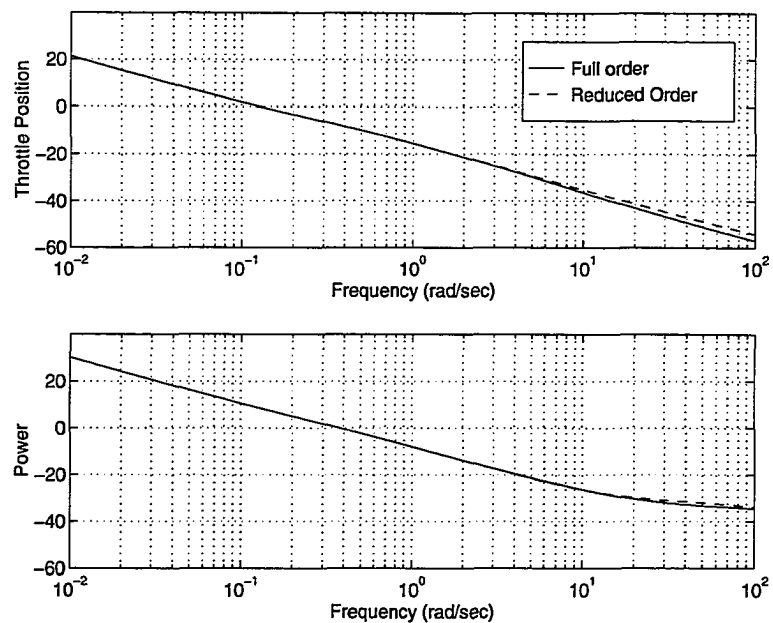


Figure 4.9: Controller gains from V_{bias} .

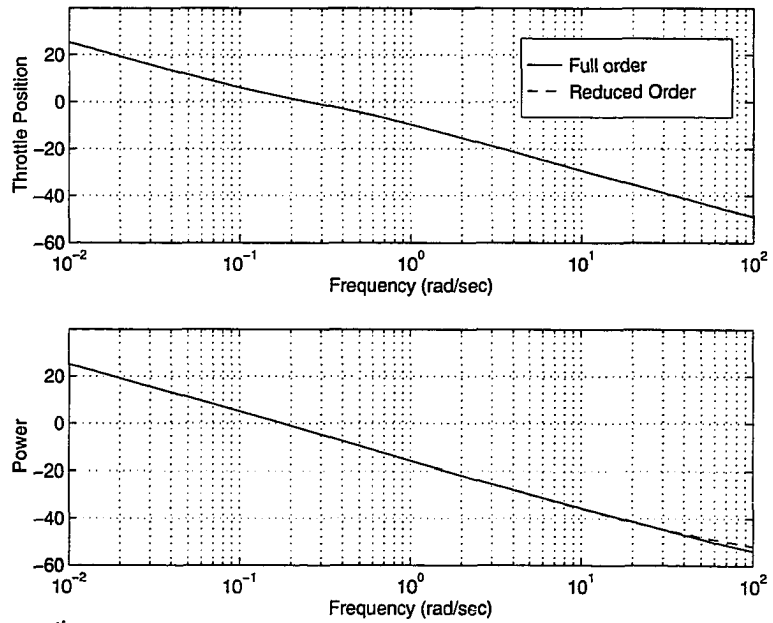


Figure 4.10: Controller gains from fluorine concentration.

4.1.2 Implementation

The controller design was based on a model of the PGP with normalized inputs and outputs. Before the controller could be implemented, these scalings need to be incorporated. This was done in the Simulink block diagram shown in Figure 4.11. Also, the controller needed to be discretized for implementation on a digital computer (using the LabVIEW system described in Section 2.2). This was accomplished using the **c2d** command from the Matlab Control Systems Toolbox and yielded a controller of the structure

$$\begin{aligned}x(k+1) &= \bar{A}_c x(k) + \bar{B}_c \begin{bmatrix} y(k) \\ r(k) \end{bmatrix}, \\ u(k+1) &= \bar{C}_c x(k) + \bar{D}_c \begin{bmatrix} y(k) \\ r(k) \end{bmatrix}. \end{aligned} \quad (4.34)$$

4.2 Disturbance Rejection Experiments

A number of experiments were designed to examine the ability of the plasma generation process controller to attenuate process disturbances. The controller was compared to the standard practice in its ability to reject disturbances to etch rate. Etches were performed on unmasked wafers with material layers polysilicon/SiO₂/Si substrate. Etch rate data was collected in real time using the reflectometry system described in Section 2.1.4. This data was processed after the experiments, as described in Section 2.1.4, and was not available to be used for etch rate control.

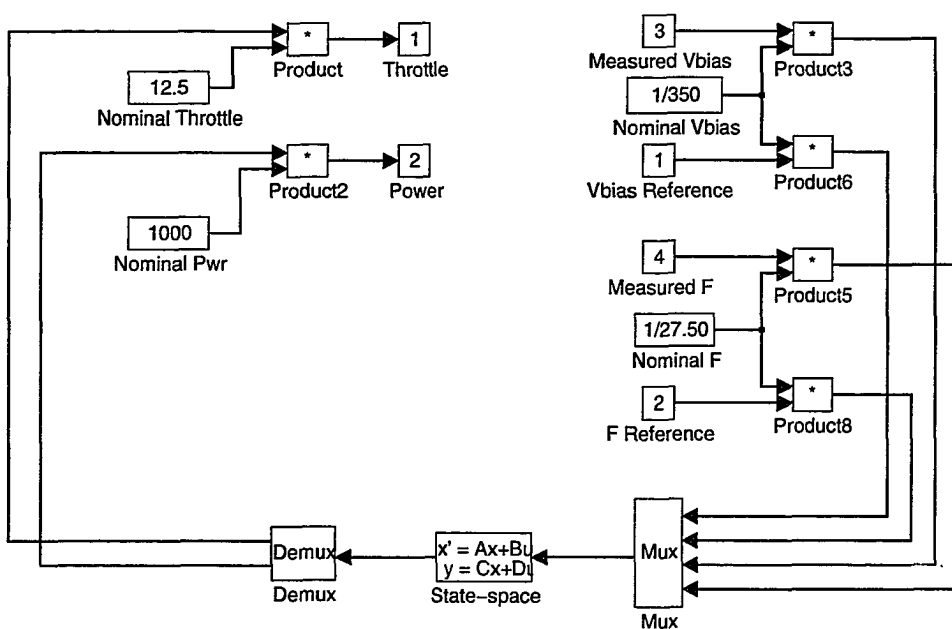


Figure 4.11: Simulink block diagram: controller structure.

4.2.1 Description of Experiments

All of the experiments have a common disturbance due to the lack of a load lock on our AME-8300. Without a load lock, the chamber must be opened to the ambient atmosphere when a wafer is loaded before each etch. As a result, water vapor adsorbs onto the inner walls of the reactor; the thickness of this film seems to vary with the degree of polymer buildup on the reactor's inner surfaces and the ambient conditions in the cleanroom. The desorption of this moisture into the chamber acts as a "wall disturbance" to the etch process and is present in all of our experiments. As our reactor has a large surface area, this is a very large disturbance. While in a production environment etchers are usually load locked, the condition of the chamber walls varies as the reactor seasons. We shall use the wall disturbance as a test to demonstrate the power of feedback control.

The experiments that were run are now described:

1. *Baseline, Standard Practice Etch:* This etch was run with the pressure, CF_4 flow rate, and applied power set to their nominal values, *i.e.*, 20 mTorr, 30 sccm, and 1000 W, respectively. In this experiment, pressure was regulated by a PID loop internal to the throttle valve controller, and V_{bias} and $[F]$ were not regulated.
2. *Baseline, Closed-Loop Etch:* In this case, the plasma generation process controller was used to demonstrate the efficacy of feedback control in reducing the effect of the wall disturbance upon etch rate. The setpoints for V_{bias} and $[F]$ were chosen to be 342 V and 47.1 (arbitrary units), respectively.
3. *Loading Effect Experiment:* The amount of exposed surface area to be etched will often vary from batch to batch or during a single run as material is removed; see Figure 4.12. As the amount of exposed material on the wafer increases, so does the

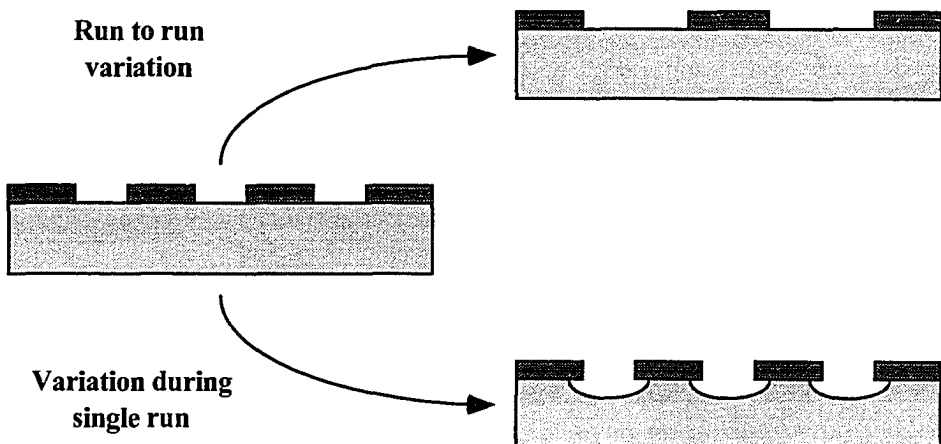


Figure 4.12: Loading effect.

rate of consumption of the etchant. This may result in a decrease in the etch rate, and is often referred to as the “loading effect” [109]. To assess the effect of a loading disturbance upon etch rate, etches were run with two wafers in the chamber, instead of just one, therefore doubling the area of exposed silicon.

4. *Oxygen Leak Experiment:* The addition of small amounts of oxygen has been found empirically to cause a significant increase in the etch rate of polysilicon. It is believed that this is caused by reactions between CF_x , $x = (1 - 3)$, and oxygen atoms. These reactions liberate more fluorine atoms and prevent recombination, thus resulting in an increased fluorine concentration [85]. The effect of an O_2 disturbance on etch rate was explored by introducing 1 sccm of O_2 in increments of $\frac{1}{2}$ sccm of O_2 applied at 600 and 1200 seconds into the etch.

5. *Power Mismatch Experiment:* As mentioned previously, an rf matching network was used for impedance matching between the power source and the reactor load. The impact of variations in the matching network or other variations in the power supply was examined by having the power generation unit respond with 2% more power

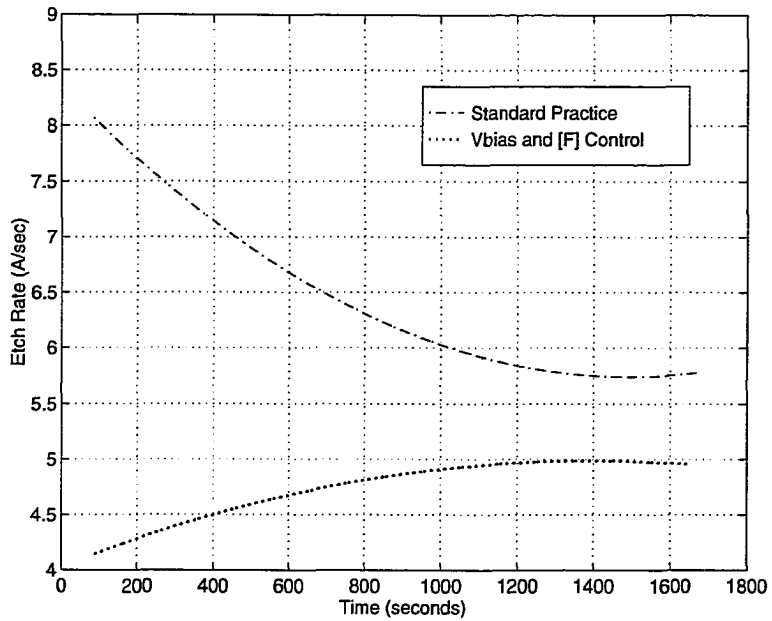


Figure 4.13: Wall disturbance experiment.

than was commanded. In the open-loop case, this resulted in shifting the power from 1000W to 1020W.

In all of the experiments the wall disturbance was present. Therefore, the first two experiments serve as a baseline to which the others were compared.

4.2.2 Experimental Results

In Figure 4.13, the dash-dot curve is the etch rate under a standard practice open-loop etch. Notice that the etch rate decreased slowly over the length of the experiment. As can be seen in Figure 4.14, the fluorine concentration follows a similar trajectory during the etch. A possible explanation for this is that, during the initial phase of the etch, a significant amount of moisture is desorbed from the walls into the chamber. This moisture leads to an increased fluorine concentration and hence increased etch rate[84]. This hypothesis is supported by experiments that showed that optical emission from the 451.1 nm line of CO

followed a trajectory similar to that of fluorine concentration. As the experiment progresses, the desorption of moisture decreases, as does the etch rate. The etch rate under the closed-loop conditions is shown by the dotted line. The corresponding trajectories for the plasma characteristics and actuator commands are shown in Figure 4.15 and 4.16, respectively. As one can see, the etch rate was much more constant under closed-loop conditions. The etch rates settled to different values because the setpoints under closed-loop control were different from the steady-state values of the plasma conditions in the open-loop experiment³. In Figure 4.17 it is shown that, if the plasma setpoints are chosen to be the steady-state open-loop conditions, then the etch rates do indeed settle to the same rate. In this closed-loop experiment, as well as the others, the etch rate started off below the steady-state value. However, the values of V_{bias} and $[F]$ remain constant throughout the etch. One potential explanation is that the fluorine estimate, $[F] = \frac{I_F}{I_{Ar}}P$, overestimated the fluorine concentration resulting from the O_2 disturbance [47]. The controller responded by reducing the actual fluorine concentration below the desired value and thus decreased the etch rate. As the disturbance decayed during the run, the estimate was more accurate and the etch rate approached its steady-state value. Another possible reason for the reduced etch rate during the first portion of the etch is that factors other than V_{bias} and $[F]$ affect the etch rate. In other words, while regulating V_{bias} and $[F]$ does reduce the impact of the disturbance substantially, it does not eliminate its effect.

Figure 4.18 shows the etch rates during the loading effect experiment. Here, the dashed curve represents the open-loop etch rate while the solid curve represents the closed-loop etch rate. The dash-dot and dotted lines from the wall disturbance experiments are included on this and the other plots to make comparisons easier. As expected, increased loading led to

³The reason that the plasma setpoints did not match the open-loop steady-state values was due to operator error.

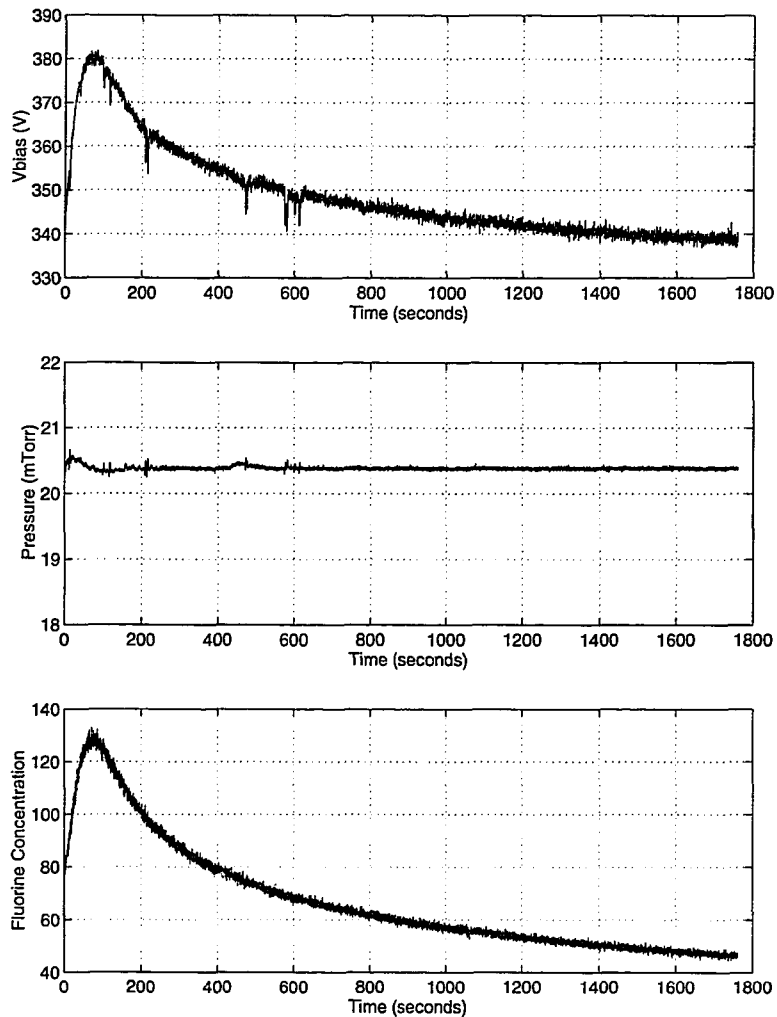


Figure 4.14: Response of plasma characteristics during standard practice etch.

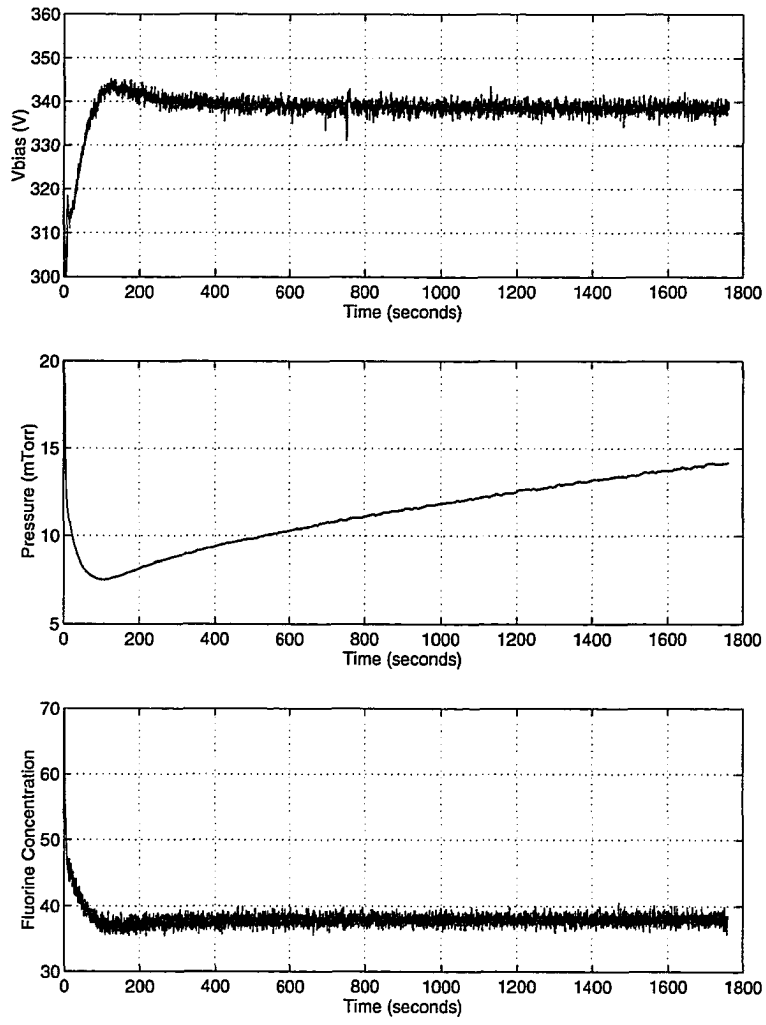


Figure 4.15: Response of plasma characteristics during closed-loop etch.

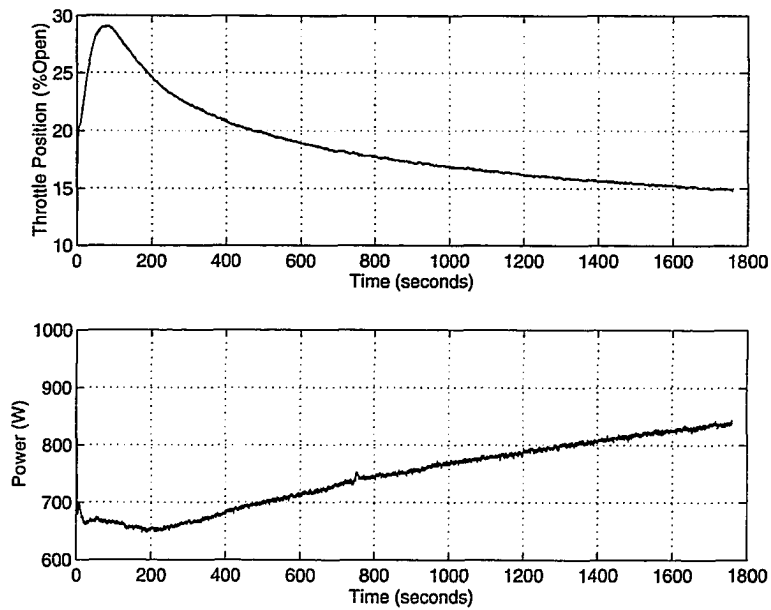


Figure 4.16: Corresponding actuator responses during closed-loop etch.

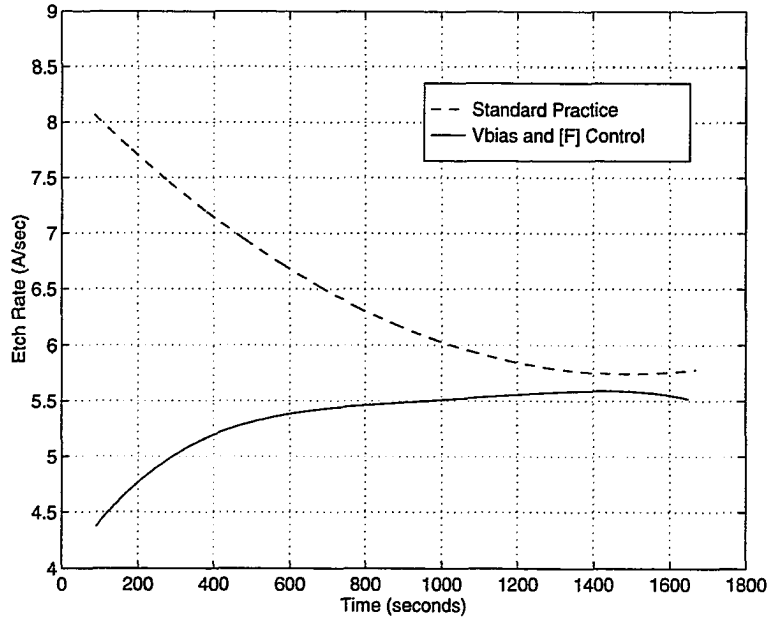


Figure 4.17: Etch rate with plasma setpoints matching steady-state conditions from standard practice baseline etch.

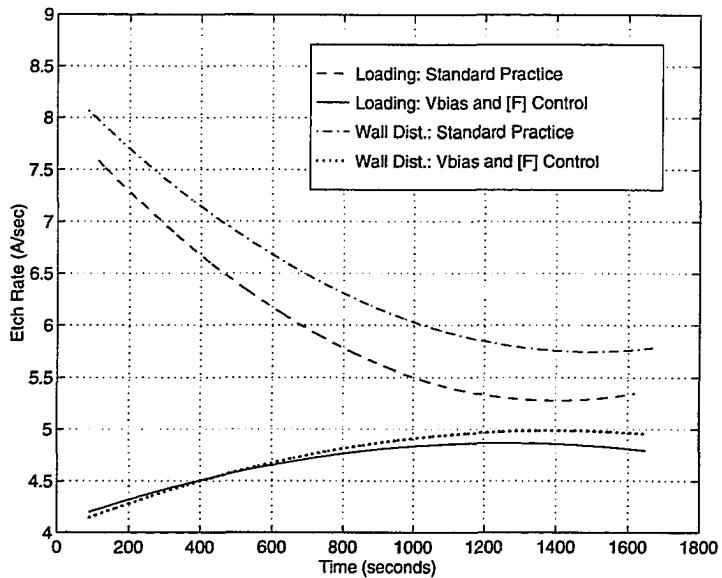


Figure 4.18: Loading experiment.

a decrease in etch rate under open-loop conditions. However, comparison of the closed-loop data (the solid and dotted lines) showed that the impact of the loading on etch rate was greatly attenuated.

Etch rate data for the oxygen leak experiment is shown in Figure 4.19. Notice that upon injection of oxygen, the etch rate increased during the standard practice etch, as expected. Under closed-loop conditions, the addition of oxygen appeared to make virtually no difference to the etch rate. However, recall from Section 2.1.4 that the etch rate measurement was actually the average rate between a peak and valley in the reflected interference pattern. During the disturbance experiments, etch rate measurements were available approximately every 90 seconds. Therefore, it is likely that the etch rate did change at each step in O₂ flow, but the effect was attenuated before the next etch rate measurement was available. Notice that, despite very similar operating conditions, there was a difference in the open-loop experiment between the dashed curve and the dash-dot curve even before the injection

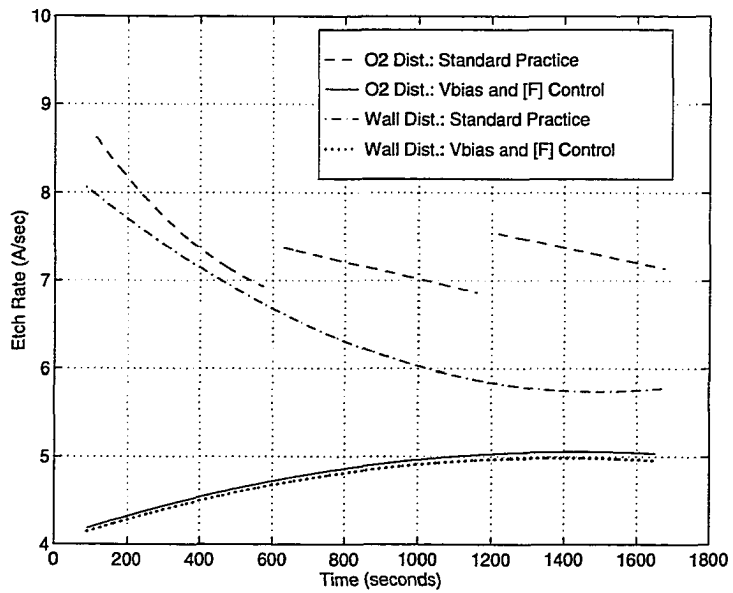


Figure 4.19: Oxygen disturbance experiment.

of oxygen. An explanation for this phenomenon is that the amount of moisture absorbed on the walls varies from etch to etch depending upon the duration of the exposure to the atmosphere while loading the wafer and the condition of the chamber.

Finally, the power disturbance results are shown in Figure 4.20. As expected, an increase in applied power increased the etch rate under open-loop conditions. However, under closed-loop control, there was a much smaller change in etch rate.

These results demonstrate that closed-loop control of the key plasma parameters, such as V_{bias} and $[F]$, can result in a significant reduction in the effects of common disturbances as compared to the standard practice open-loop etches. This was certainly quite true for the loading effects, oxygen disturbance, and the power disturbance. This can be seen very clearly in Figure 4.21, where results from the various disturbances using each control strategy are presented again. Even for the wall disturbance, we have achieved a significant reduction in the impact of the disturbance, but there is room for improvement.

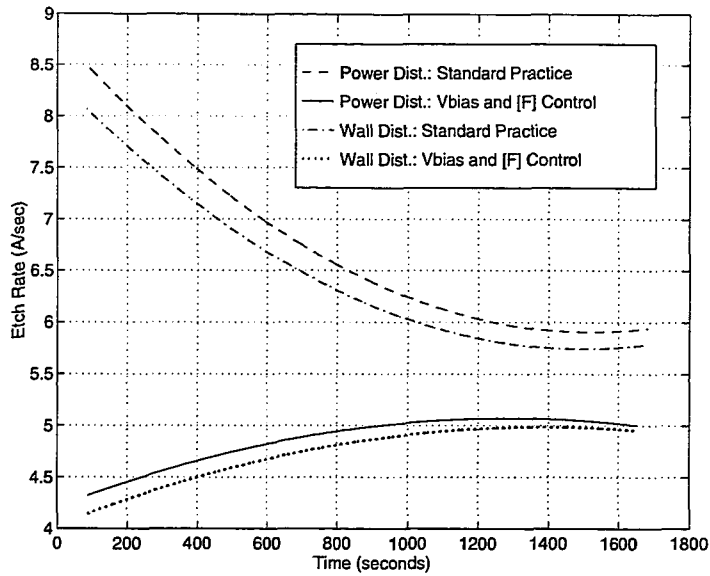


Figure 4.20: Power disturbance experiment.

4.3 Comparison of $V_{bias}/[F]$ vs. $V_{bias}/\text{Pressure}$ Control

It is becoming common in industrial applications to use feedback control to regulate both pressure and V_{bias} . The oxygen disturbance experiment was repeated to compare the effect of controlling only pressure, V_{bias} and pressure, and V_{bias} and fluorine concentration. In this experiment, 1 sccm of O_2 was introduced into the feed gas at 600 seconds into the etch. As can be seen in Figure 4.22, that while $V_{bias}/\text{pressure}$ control slightly attenuates the effect of the wall disturbance during the first portion of the etch, this strategy is ineffective against the oxygen disturbance. This result is not surprising as the oxygen disturbance primarily effects etch chemistry and hence fluorine concentration.

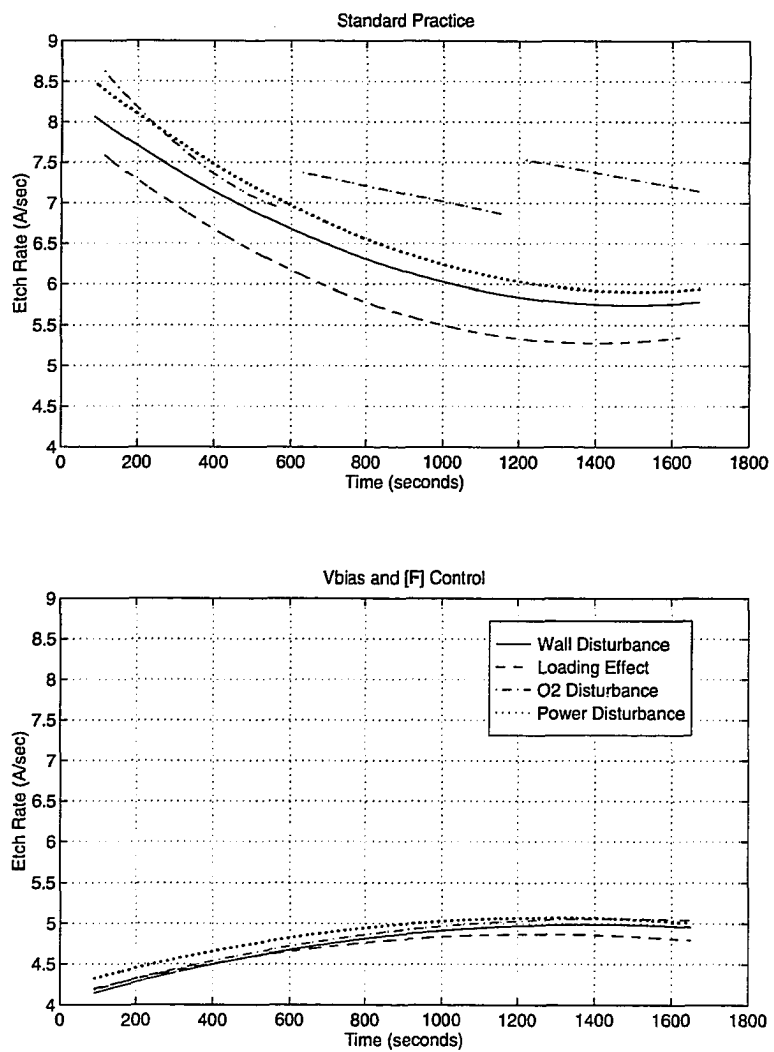


Figure 4.21: Comparison of the effects of the various disturbances.

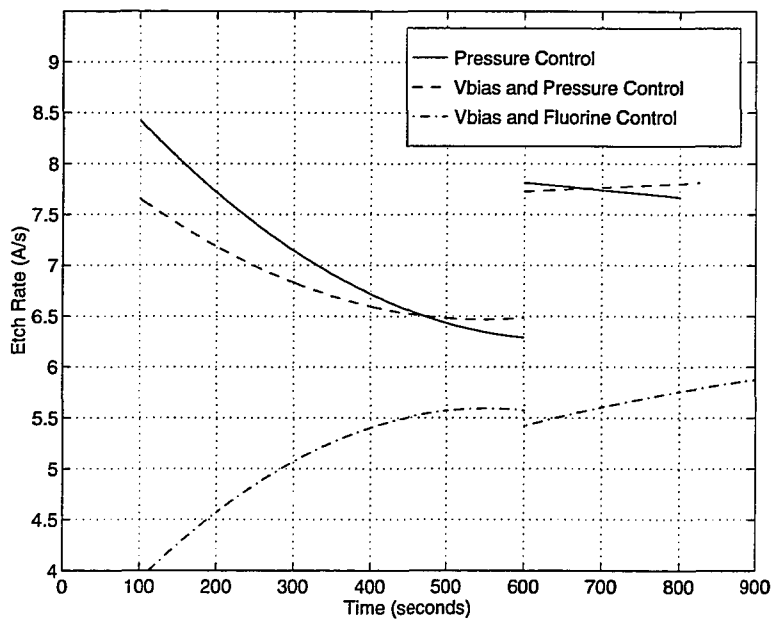


Figure 4.22: Comparison of controlling pressure, V_{bias} /pressure, and $V_{bias}/[F^-]$.

CHAPTER 5

Sidewall Profile Control Strategy

In the previous chapter, it was shown that real-time multivariable feedback control can be used to stabilize etch rate during reactive ion etching. While the stabilization of etch rate shows the utility of real-time feedback control, there are other important etch characteristics that also need to be controlled. As was described in Section 1.1.2, these include sidewall profile, selectivity, uniformity, and surface damage. In particular, control of sidewall profile has been an active area of research [1, 61, 66, 93]. I have developed a strategy for sidewall profile control based on applying real-time feedback to the plasma generation process. In this chapter, a study of the feasibility of this strategy is presented.

5.1 Sidewall Control Strategy

Sidewall profiles are difficult to characterize due to the small size ($< 1 \mu m$) of most features in integrated circuit devices. These profiles are often measured using scanning electron microscopy (SEM). Unfortunately, SEM is inherently destructive (the wafer must be cleaved through the structure of interest) and can therefore only be used on selective samples. Recently, a non-destructive optical technique known as scatterometry has been

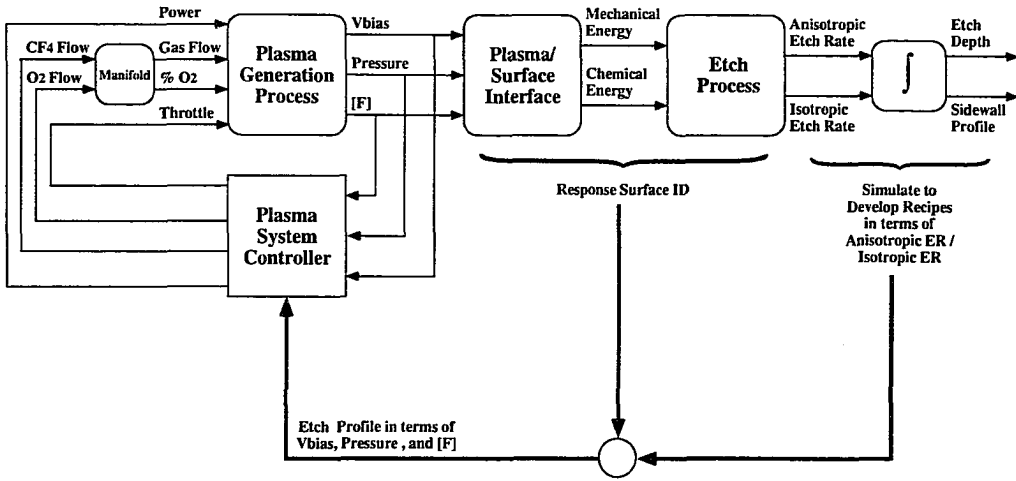


Figure 5.1: Sidewall control strategy.

explored to characterize reactive ion etch profiles [45, 80, 81]. In scatterometry, laser light is scattered off a periodic structure on the wafer surface. The sidewall profile can then be estimated from the intensity of the scattered light at various diffraction angles. Scatterometry requires the measurement of diffracted light intensity over the entire 180 degrees above the wafer. Therefore, as there are a limited number of viewports on most chambers, scatterometry is not suited for *in situ* measurements during the etch process. In addition, the analysis can be problematic when a mask layer is present over the profile. Therefore, scatterometry is not suited for real-time profile measurement during reactive ion etching, and an indirect strategy must be used to control sidewall profile.

The strategy for sidewall profile control that has been developed is based on a decomposition similar to that used in Section 3.1. This strategy can be broken down into two parts: 1) determining the plasma characteristics necessary to achieve a desired sidewall profile and 2) using a feedback controller to set these characteristics during an etch. The mapping of sidewall profile to plasma properties is, in turn, divided into two parts. First,

the etch rate components associated with the sidewall profile are found using a string model simulation. Next, the plasma characteristics necessary to generate these etch rate components are determined using a response surface. Once the necessary plasma properties are found, the etch can be performed using a feedback controller to regulate the plasma to these conditions. In order to implement this strategy, a linear model of the plasma generation process must first be developed. From this model, a real-time feedback controller can be designed to hold plasma characteristics at desired values despite disturbances. Next, for each of a variety of plasma conditions the resulting sidewall profile must be mapped into etch rate components. Results from different operating points can then be used to construct a response surface relating plasma characteristics to etch rate components. In the rest of this chapter, the feasibility of this strategy is shown by relating the etch rate components to a sidewall profile etched using real-time feedback control.

5.2 Process Chemistry

In using plasma characteristics to control sidewall profile, it is likely that all three properties (V_{bias} , pressure, and fluorine concentration) play an important role. As was seen in Section 3.2.2, in a pure CF_4 chemistry only two of these characteristics could be independently controlled. In order to achieve control over a third characteristic, O_2 was added to the feed gas. Oxygen causes the following reactions to occur in the plasma [85, 90, 91]





and



These reactions lead to a higher fluorine concentration by liberating more fluorine radicals and by blocking the recombination reaction



where $x = \{0, \dots, 3\}$. Oxygen has a small effect on total dissociation and the electrical properties of the discharge; thus its addition does not greatly effect V_{bias} and pressure. The use of %O₂, in addition to throttle position and applied power, should allow independent control of all three plasma characteristics. This was verified by using the dc gain matrix for the plasma generation process

$$\begin{bmatrix} V_{bias} \\ \text{Pressure} \\ \text{Fluorine} \end{bmatrix} = \begin{bmatrix} 0.3713 & 0.0088 & 0.8232 \\ -1.2194 & 0.0168 & 0.0084 \\ -0.6279 & 0.5932 & 1.0835 \end{bmatrix} \begin{bmatrix} \text{Throttle} \\ \% \text{O}_2 \\ \text{Power} \end{bmatrix} \quad (5.6)$$

The singular values for this matrix were

$$\begin{bmatrix} 1.6016 & 1.2560 & 0.2835 \end{bmatrix}, \quad (5.7)$$

yielding condition number of

$$\kappa = 5.7. \quad (5.8)$$

Thus, the dc gain matrix was invertible and independent control of the three plasma characteristics was possible.

In general, sidewall passivation is often used to control etch profiles. As was discussed in Section 1.2.3, in a CF_4 chemistry the passivation occurs when polymers form on the polysilicon in areas where ion bombardment is not present. While the addition of hydrogen into the plasma chemistry potentially allows for the control of polymerization, there is a significant amount of preliminary research that needs to be performed before this procedure may be used in a real-time control strategy. This is beyond the scope of this dissertation. To focus our research, we decided to simplify the plasma/surface interactions by not exploiting sidewall passivation. The addition of oxygen to the plasma chemistry not only provides an extra degree of plasma control, but also reduces polymerization from the plasma [23].

In order to show that a variety of sidewall profiles could be achieved using the CF_4/O_2 chemistry, a number of etches were performed using the standard industrial practice of setting pressure, flow rates, and applied power. Figure 5.2 shows an isotropic sidewall profile resulting from an etch performed at 20 mTorr, %5 O_2 , 30 sccm total flow, and 1000 W applied power. Likewise, Figure 5.3 shows a near vertical profile resulting from an etch performed at 10 mTorr, %1 O_2 , 30 sccm total flow, and 1200 W applied power. These etches show that the CF_4/O_2 chemistry is capable of etching a wide variety of sidewall profiles.

5.3 Plasma Generation Process Model

As in the previous chapter, the process of designing a controller begins by developing a model of the plasma generation process for the CF_4/O_2 chemistry. As before, the first step in developing this model was the selection of an operating point around which the model would be identified. The operating conditions for throttle position and applied power were chosen to be the same as in the pure CF_4 case. It has been shown that while fluorine

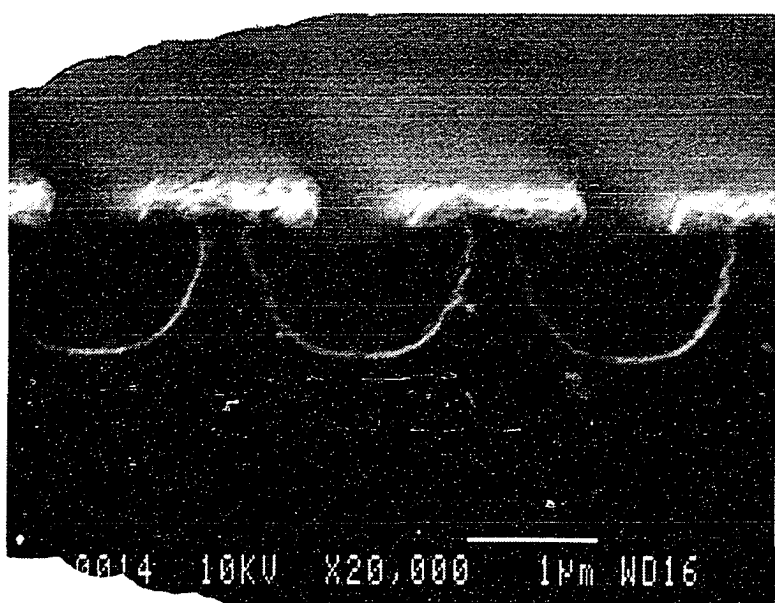


Figure 5.2: Sidewall profile resulting from an etch with settings of 20 mTorr, 5 %O₂, 30 sccm total flow, and 1000 W power.



Figure 5.3: Sidewall profile resulting from an etch with settings of 10 mTorr, 1 %O₂, 30 sccm total flow, and 1200 W power.

Throttle Position	12.5 %Open
% O ₂	5 %
Applied Power	1000 W
Total Flow Rate	30 sccm

Table 5.1: Operating point for CF₄/O₂ plasma.

concentration continues to increase up to the addition of $\sim 25\%$ O₂, the etch rate decreases after the addition of $\sim 12\%$ O₂ [79]. Hence, the operating point was selected at 5% O₂ with a total gas flow (flow of CF₄ + Ar + O₂) of 30 sccm. The operating point is given in Table 5.1.

Using the same techniques outlined in Section 3.2.2 the following model was identified for the CF₄/O₂ plasma generation process

$$\begin{bmatrix} V_{bias} \\ \text{Pressure} \\ \text{Fluorine} \end{bmatrix} = \begin{bmatrix} \frac{1.65e^{-42s}}{s+0.16} & \frac{0.25e^{-77s}}{s+0.41} & \frac{12.23(s+0.27)}{(s+0.19)(s+62.42)} \\ \frac{-0.97e^{-42s}}{(s+0.18)(s+3.00)} & \frac{0.024e^{-77s}}{s+0.40} & \frac{-0.011(s-0.006)}{(s+0.19)(s+2.33)} \\ \frac{4.85(s-0.73)e^{-42s}}{(s+0.11)(s+39.76)} & \frac{0.33e^{-77s}}{s+0.17} & \frac{0.49(s+0.067)}{(s+0.095)(s+19.69)} \end{bmatrix} \begin{bmatrix} \text{Throttle} \\ \% \text{O}_2 \\ \text{Power} \end{bmatrix}. \quad (5.9)$$

As shown in Figure 5.4, in this case the time delay from the throttle valve was found to be 0.42 seconds, as opposed to the 0.62 seconds in Chapter 3. It is unlikely that the addition of O₂ to the plasma chemistry would have such an effect on the delay in response to throttle changes. Instead, this difference might be accounted for by the fact that the models were developed over a year and a half apart.

5.4 Plasma Controller

A plasma generation process controller for the CF₄/O₂ chemistry was designed to meet the same performance objective and design constraints outlined in Section 4.1. The state

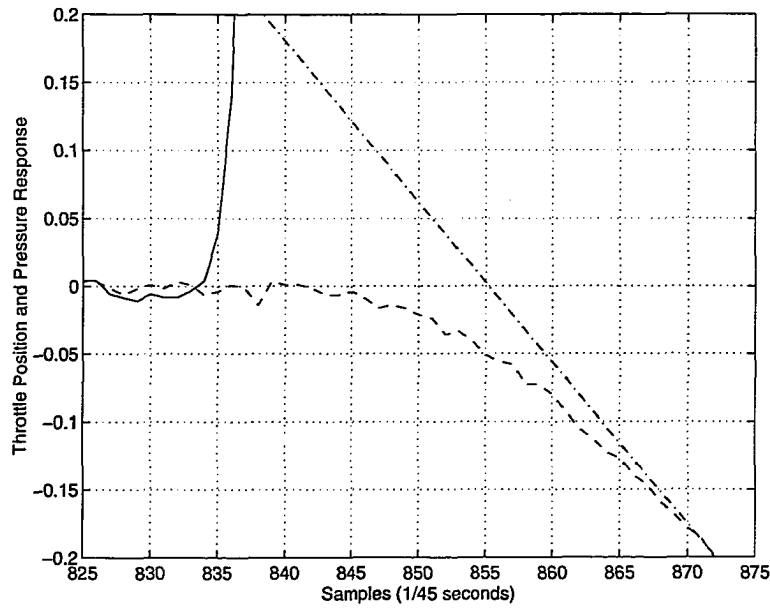


Figure 5.4: Delay in response of pressure to change in throttle position.

feedback and observer gains were found using the same design methodology with weights

$$\alpha = 3, \quad (5.10)$$

$$Q_q = \begin{bmatrix} 1.3 & 0 & 0 \\ 0 & 0.3 & 0 \\ 0 & 0 & 0.5 \end{bmatrix}, \quad (5.11)$$

$$R = \begin{bmatrix} 1.5 & 0 & 0 \\ 0 & 1.5 & 0 \\ 0 & 0 & 0.5 \end{bmatrix}, \quad (5.12)$$

and

$$\rho = 1. \quad (5.13)$$

As can be seen in Figures 5.5 through 5.10 the controller achieves its performance objectives.

The controller had 19 states, but was reduced to 8 states using the model reduction method

outlined in Section 4.1.1. Inspection of the Bode plots for the full and reduced order controllers (shown in Figures 5.11 through 5.13), shows that the controllers have similar responses in their crossover regions.

5.4.1 Anti-Windup Design

As was mentioned in Section 4.2.1, a large disturbance due to outgassing from the chamber walls was present during every etch performed on our AME-8300. This disturbance primarily effects the fluorine concentration. As can be seen from the dc gain matrix in Equation 5.6, the controller will respond to this disturbance by reducing the %O₂ in the feed gas. Because the gain from this actuator to fluorine concentration was not very large, there was the potential that %O₂ would saturate during the initial portion of an etch. Therefore, anti-windup logic was added to the controller to minimize the effect of this saturation.

The controller designed above had the form

$$\dot{x} = A_c x + B_c y + G_c r, \quad (5.14)$$

$$u = C_c x + D_c y. \quad (5.15)$$

Rather than let the actuators saturate, each input was software limited

$$\hat{u} = \begin{cases} u_{lower} & \text{if } u \leq u_{lower}, \\ u & \text{if } u_{lower} < u < u_{upper}, \\ u_{upper} & \text{if } u \geq u_{upper}, \end{cases} \quad (5.16)$$

as shown in Figure 5.14. These limits are shown in Table 5.2. The compensator was then modified by multiplying Equation 5.15 by the anti-windup gain K_u and subtracting it from Equation 5.14 [6]. This yields

$$\dot{x} = (A_c - K_u C_c)x + (B_c - K_u D_c)y + K_u \hat{u} + G_c r \quad (5.17)$$

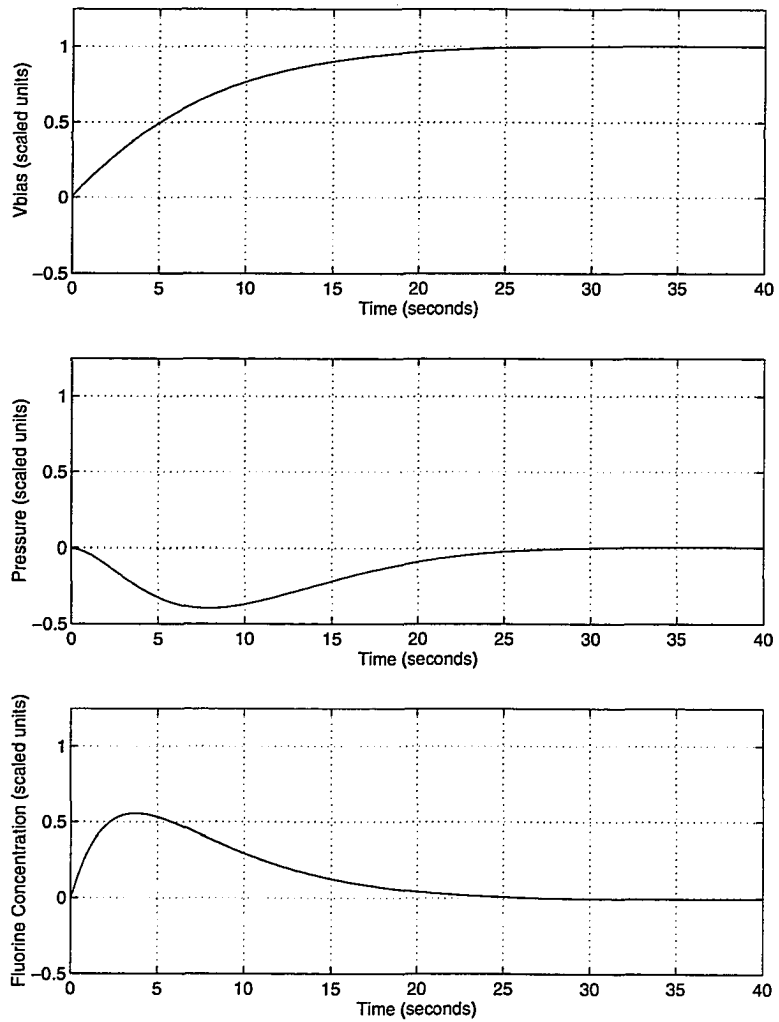


Figure 5.5: Simulated response of closed loop system to step in V_{bias} .

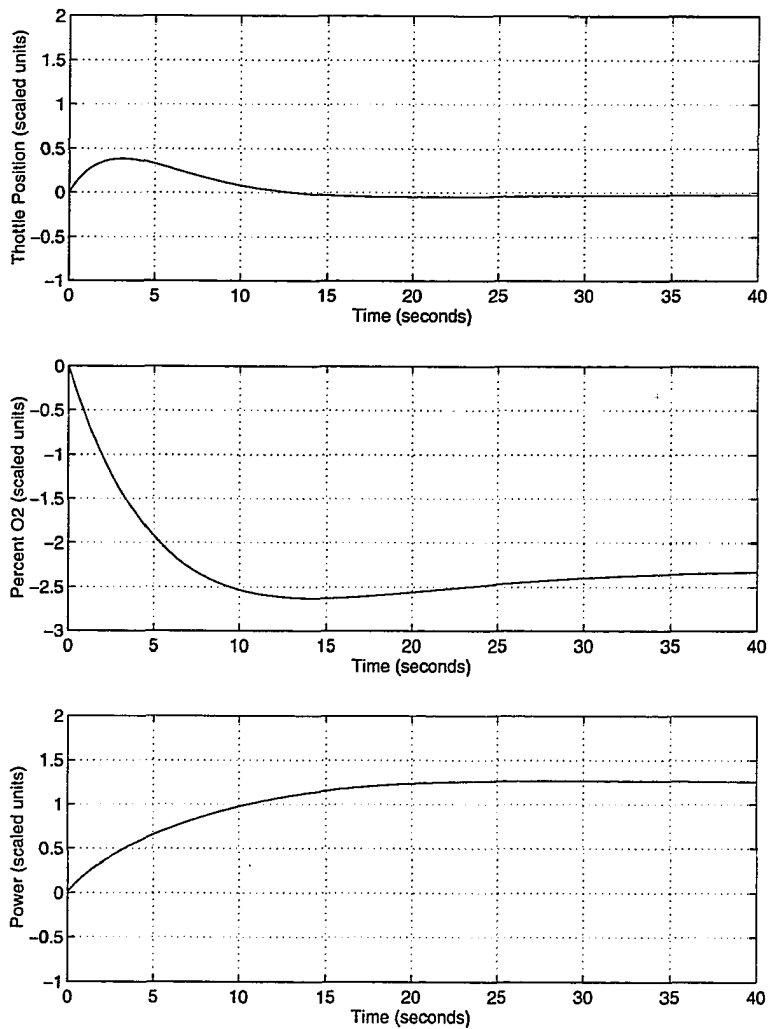


Figure 5.6: Simulated response of actuators to step in V_{bias} .

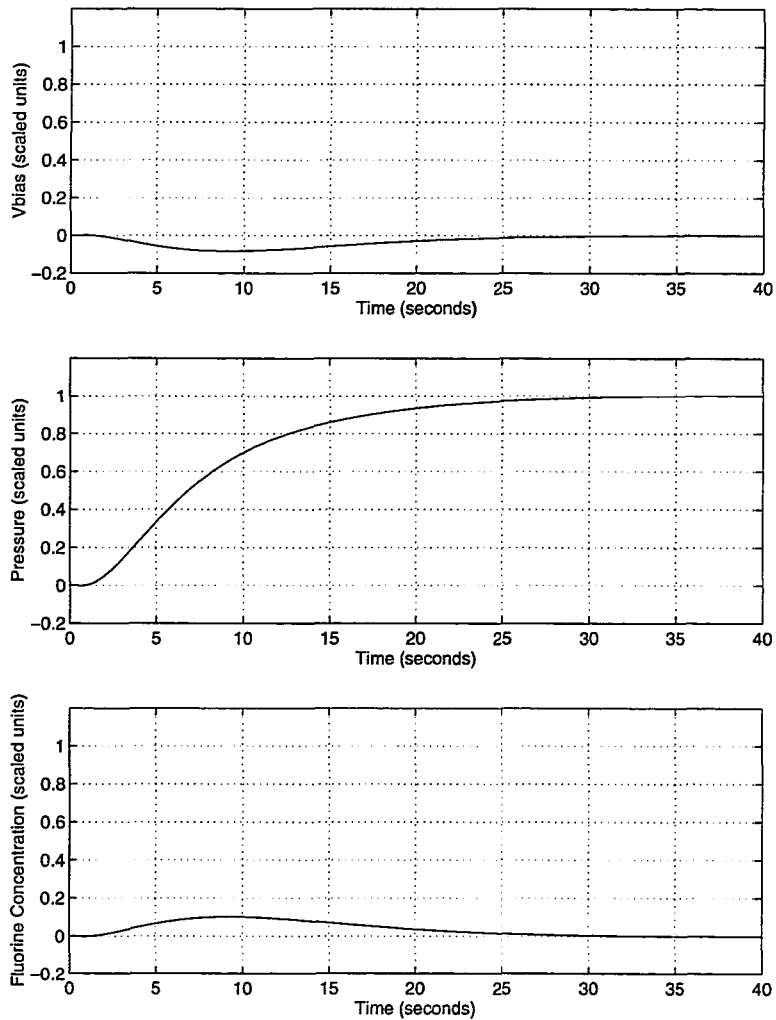


Figure 5.7: Simulated response of closed loop system to step in pressure.

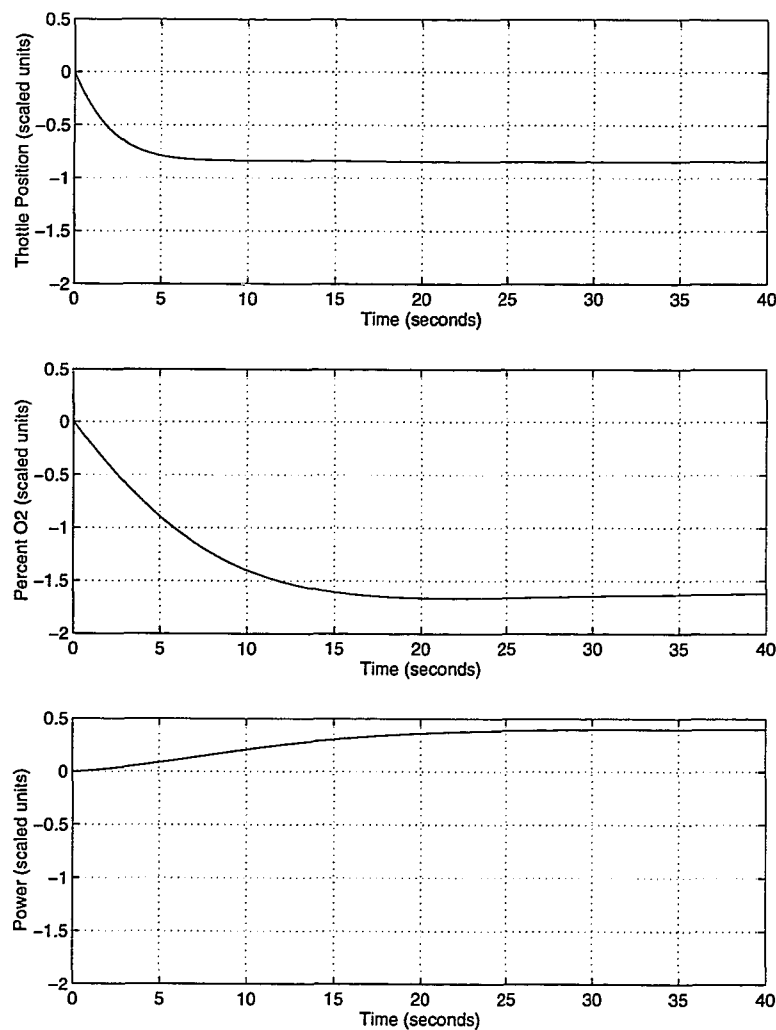


Figure 5.8: Simulated response of actuators to step in pressure.

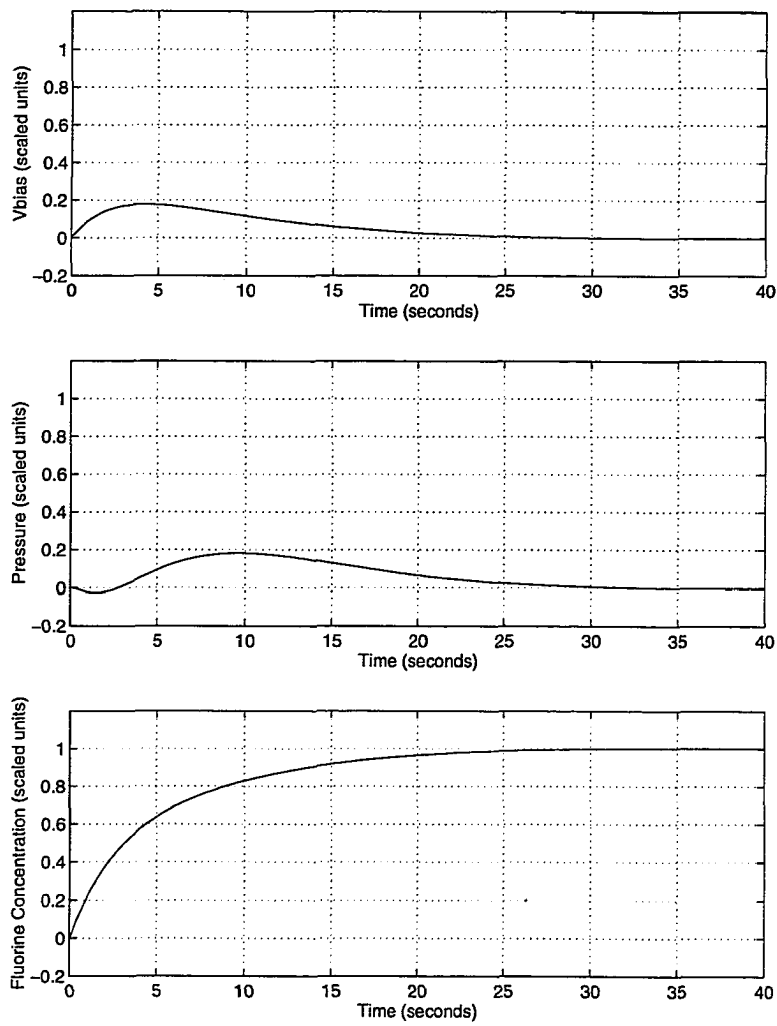


Figure 5.9: Simulated response of closed loop system to step in fluorine concentration.

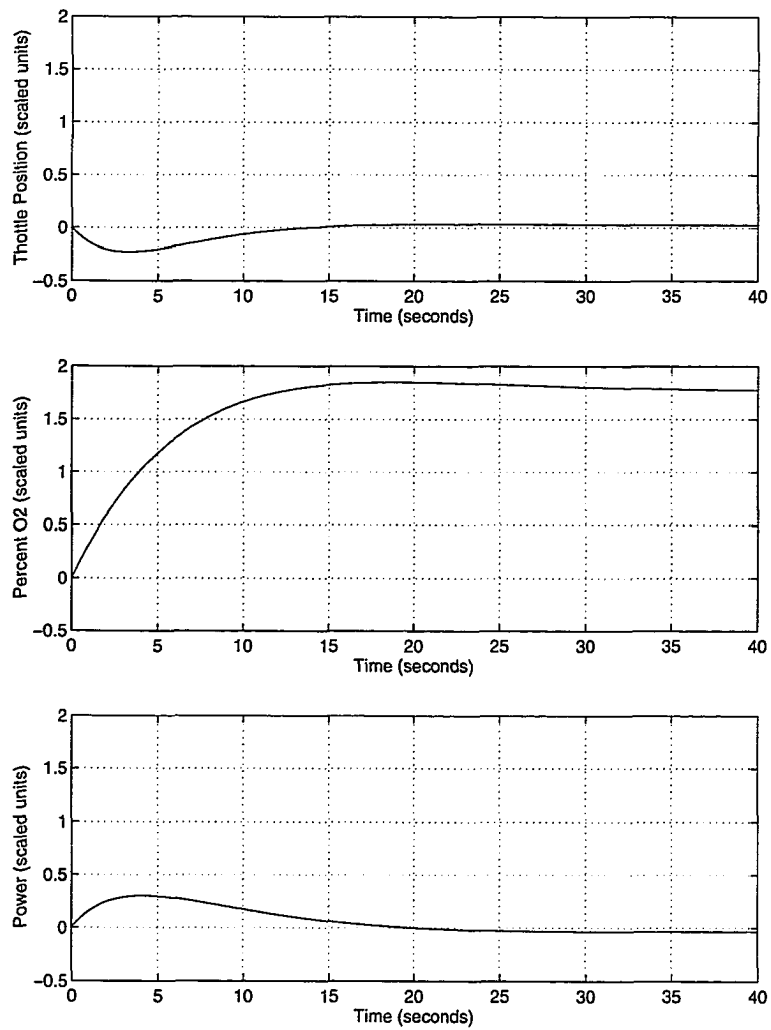


Figure 5.10: Simulated response of actuators to step in fluorine concentration.

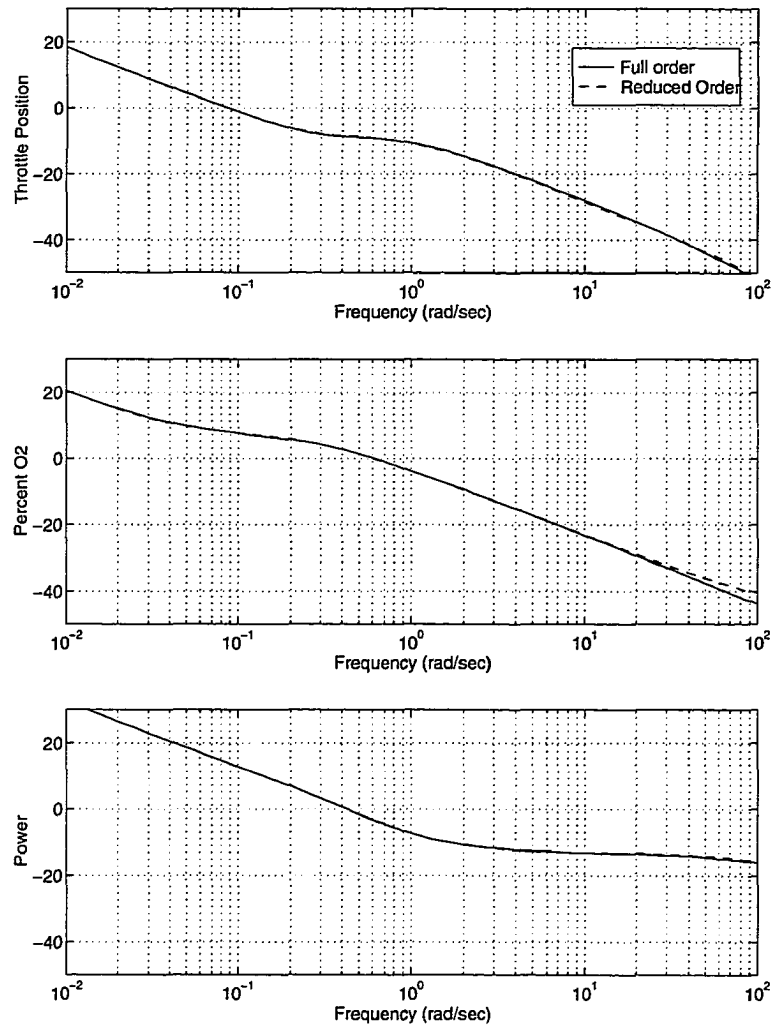


Figure 5.11: Bode plots of controller from V_{bias} to equipment inputs.

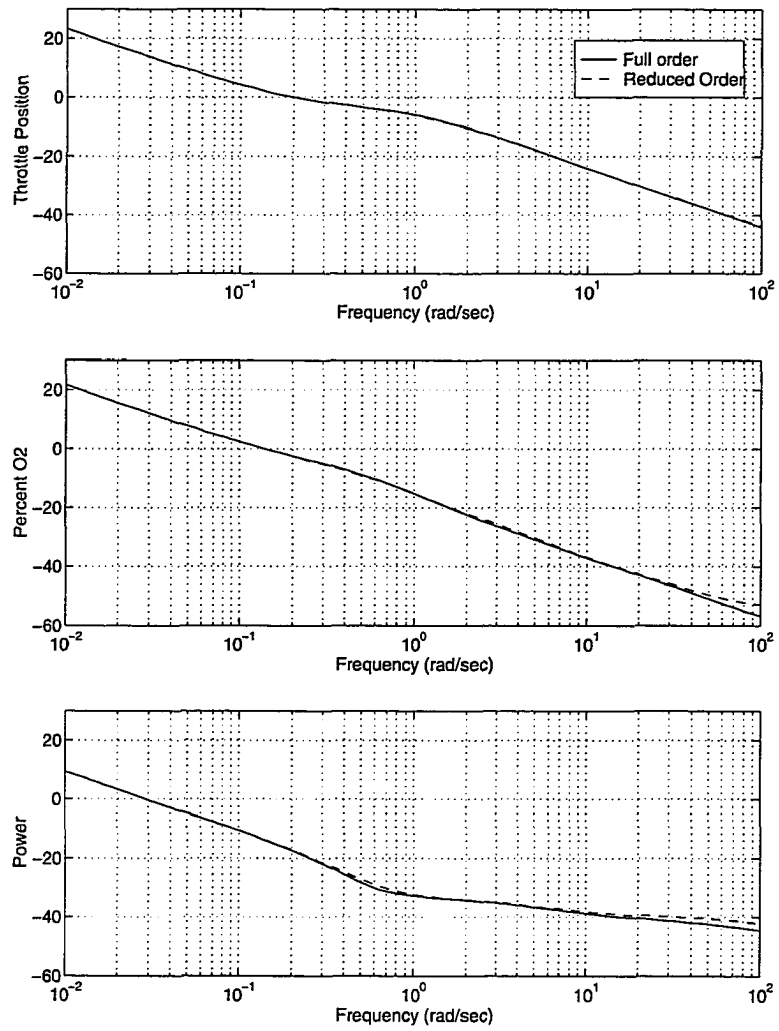


Figure 5.12: Bode plots of controller from pressure to equipment inputs.

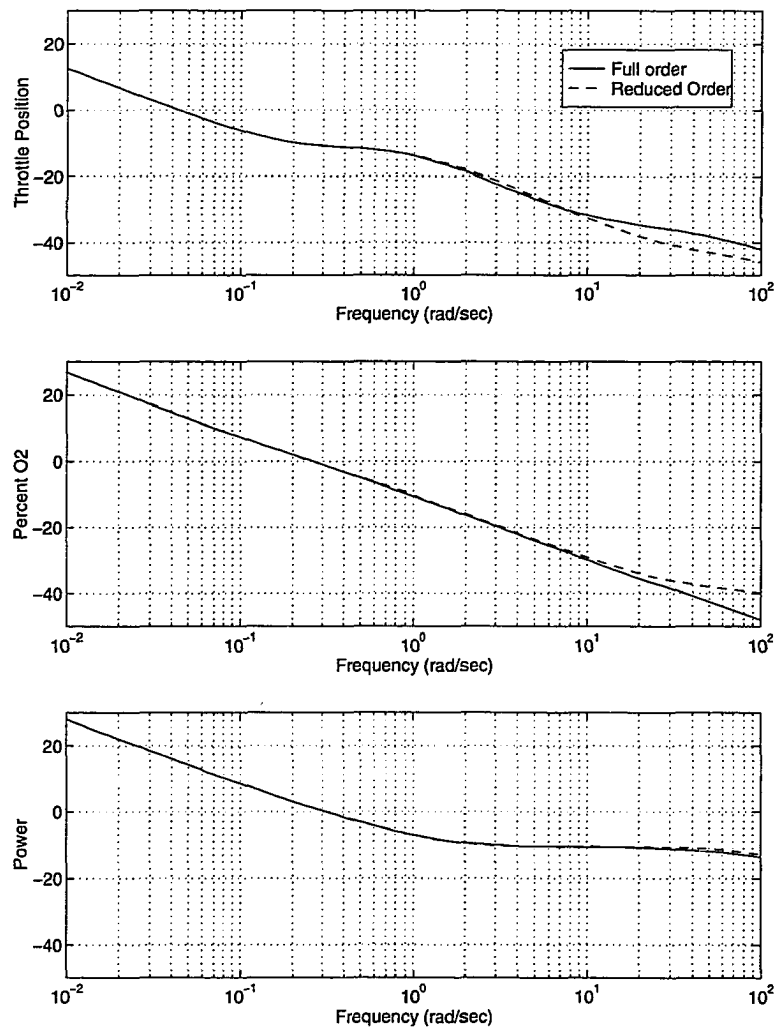


Figure 5.13: Bode plots of controller from fluorine concentration to equipment inputs.

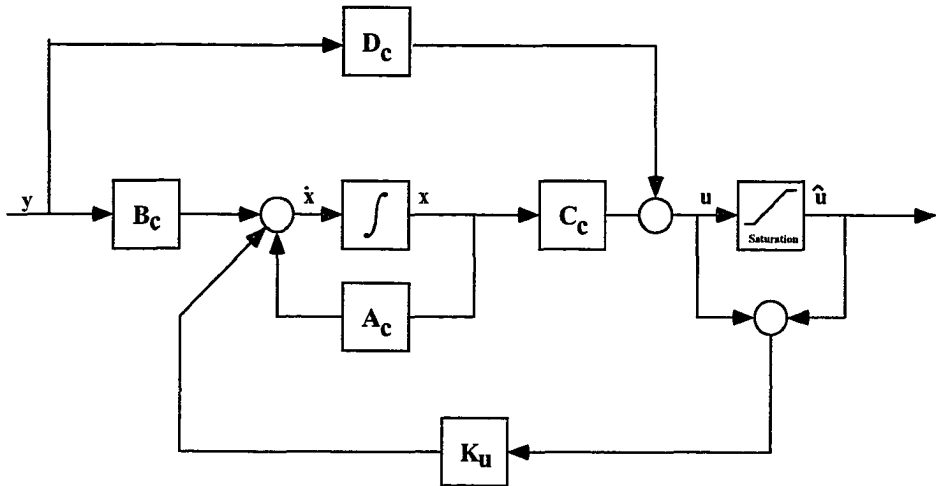


Figure 5.14: Controller with anti-windup logic.

When the actuators are not saturated ($\hat{u} = u$), Equation 5.17 reduces to Equation 5.14 and the anti-windup logic has no affect on the performance of the controller. When the actuators saturate, the anti-windup logic helps to keep the states of the controller from continuing to grow. The gain K_u was found by solving the linear quadratic regulator problem for (A'_c, C'_c) using weighting matrices

$$Q_u = 2 \times I_8 \quad (5.18)$$

and

$$R_u = I_3 \quad (5.19)$$

where I_n is the identity matrix of dimension n . This yielded an input feedback gain of

$$K_u = \begin{bmatrix} 0.107 & 0.049 & 0.161 & -0.094 & -0.128 & -0.457 & 1.262 & 0.445 \\ 0.031 & -0.016 & 0.082 & -0.072 & 0.048 & 0.918 & 0.638 & -0.867 \\ -0.181 & 0.011 & 0.267 & 0.145 & 0.051 & -0.974 & 0.009 & -1.025 \end{bmatrix}. \quad (5.20)$$

The ability of the controller, with and without anti-windup logic, to reject an exponentially decaying disturbance to fluorine concentration was simulated. As can be seen from Fig-

Actuator	Lower Limit	Upper Limit
Throttle Position	1 %Open	50 %Open
%O ₂	1%	12.5%
Applied Power	300	1500 W

Table 5.2: Software saturation limits.

ure 5.15, the controller with anti-windup logic comes off saturation more quickly than the one without the added logic.

5.4.2 Implementation

This controller was implemented using the LabVIEW data acquisition and control system. The actuator commands from the controller were software limited by the LabVIEW code and fed back to the controller as shown in Figure 5.16.

The %O₂ command from the controller must be converted to CF₄ /Ar and O₂ commands for the mass flow controllers. The total flow was held constant at 30 sccm and the percentage of oxygen was taken with respect only to the CF₄ flow. LabVIEW calculated the two flow commands as

$$CF_4/Ar = \frac{\text{Total Flow}}{1 + \%O_2(1 - \alpha)} \quad (5.21)$$

and

$$O_2 = \text{Total Flow} - CF_4/Ar, \quad (5.22)$$

where α is the percentage of argon in the premixed CF₄ /Ar bottle.

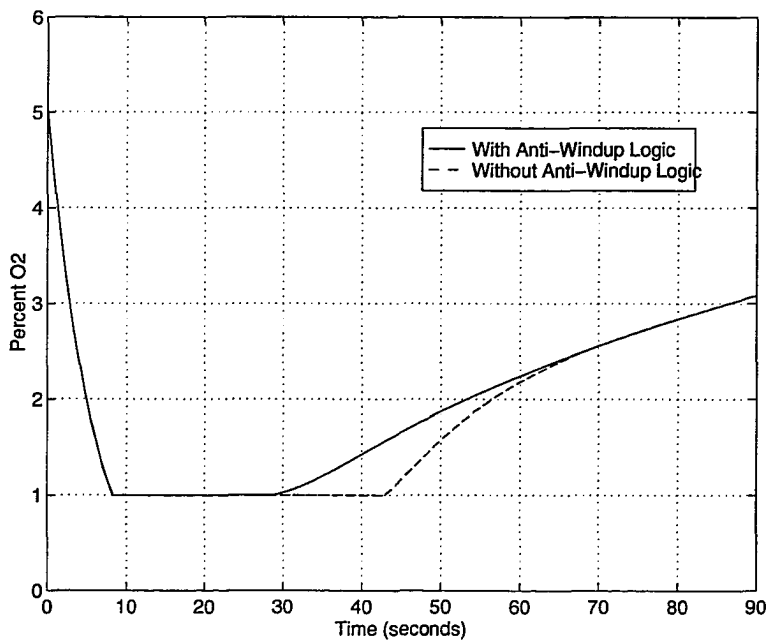


Figure 5.15: Simulated response of %O₂ to fluorine disturbance for controller with and without anti-windup logic.

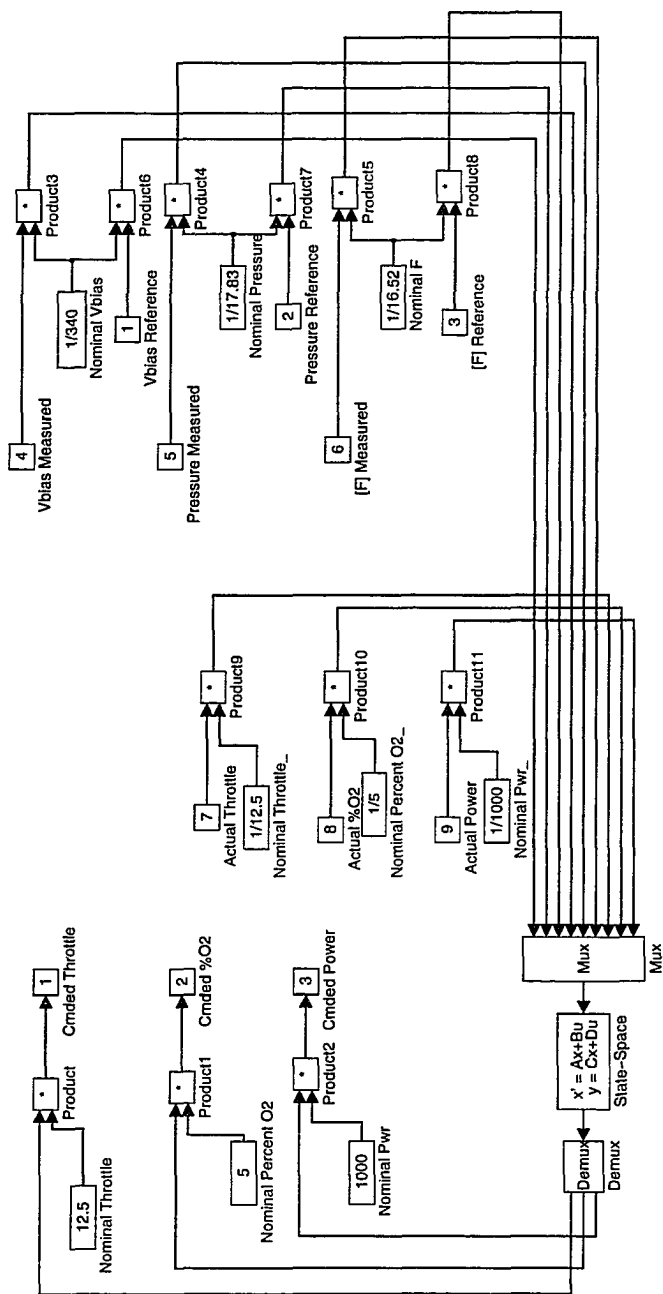


Figure 5.16: Controller structure with anti-windup.

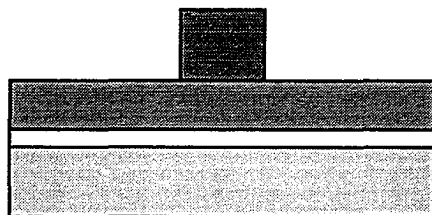
5.5 Etch Study

In the overall control strategy, a response surface will be used to map plasma characteristics to etch rate components. An etch study will be performed to obtain the sidewall profiles resulting from etches at a variety of plasma conditions. These profiles will then be analyzed to yield the associated etch rate components; thus allowing the construction of a model relating plasma properties to isotropic and anisotropic etch rates. In this section, the feasibility of this method is shown by performing these steps for a single set of operating conditions.

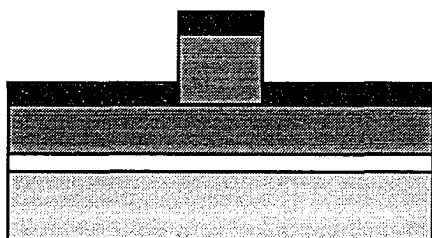
5.5.1 Wafer Preparation

In this etch study, the real-time feedback controller was used to control the etcher at constant plasma characteristics during the etching of a masked polysilicon/SiO₂/Si wafer. The selectivity of polysilicon to photoresist in a CF₄/O₂ plasma is very poor. Therefore, the features in a photoresist mask would change significantly during the etch. To focus this research, a metal mask, which will not etch in a CF₄ chemistry, was used. This mask allowed us to concentrate on modeling the effect that plasma properties have on etch rate components without having to account for the effects of mask erosion. A lift-off process [102] (shown in Figure 5.17) was used to define the metal mask, which contains 1 μm , 2 μm , and 5 μm linewidths with various spacings.

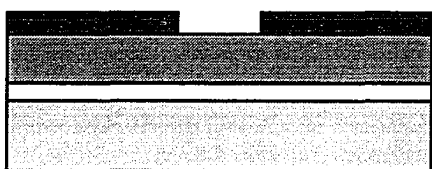
Nickel masks were initially used during this research. However, nickel masks have been shown to enhance etch rate, and thus affect sidewall profile, in a CF₄/O₂ chemistry [31]. It is suspected that this is due to nickel acting as a catalyst for the dissociation of CF_x. As an alternative, etches were performed using aluminum and chromium for the mask layer, since these two metals have less of a catalytic effect. With both of these etches, a large amount



Pattern Inverse Image



Directionally Deposit Metal



Remove Resist

Figure 5.17: The lift-off process.

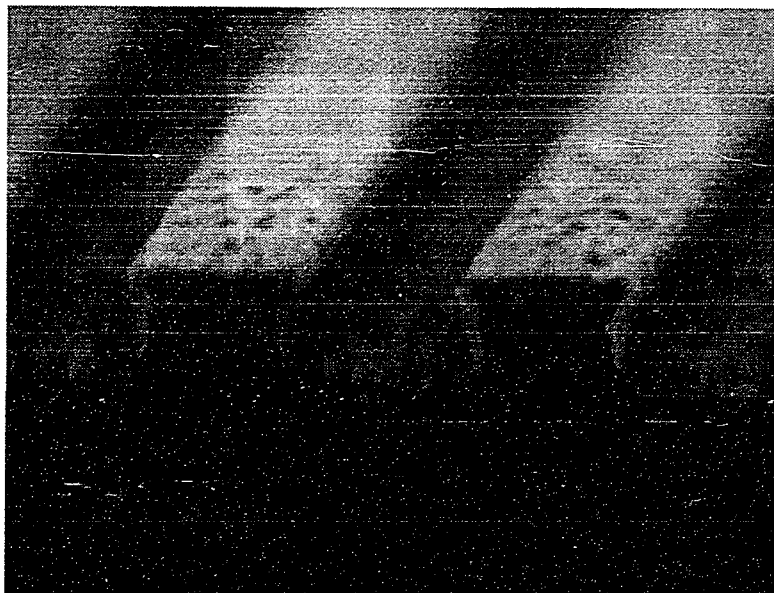


Figure 5.18: Polymer formation under a chromium mask.

of polymer was observed under the masks (see Figure 5.18). This amount of polymerization is not typical for a CF_4/O_2 plasma and the exact cause has not been determined. To limit the scope of this feasibility study, attempts were made to minimize polymer deposition, so we continued to use nickel masks.

The first step in the lift-off process is to make a photoresist mask layer with the inverse of the desired pattern. This was done using a Karl-Suss MA-6 contact aligner with an exposure wavelength of 350 nm. Initially, a clear field mask with the inverse pattern and Shipley Microposit S1822 photoresist were used. This led to the following problem. In order to define the smaller linewidths it was required that the aligner be in the hard-contact mode; however, in this mode, the wafers would adhere to the clear field mask after exposure. It is thought that some of the photoresist was vaporized during exposure and that after cooling it “glued” the wafer to the mask.

A dark field mask and Hoechst AZ 5214 image reversing photoresist [99] was used to

overcome the adhesion problem. Before patterning, the wafers were put through a dehydration bake at 110 °C to remove any moisture from their surfaces. Then the 5214 photoresist was spin-coated onto the surface at 4000 rpm for 30 seconds. After a soft bake for 30 minutes at 90 °C, this resulted in a 1.4 μm thick resist layer. The wafers were then exposed for 10.4 seconds with a light intensity of 5 mA. A 30 minute bake at 100 °C was used to cross link polymers in the exposed portion of the photoresist. Next, the wafers were flood exposed, with no mask, for 30 seconds. Finally, the wafers were developed for 1.0 minute with MF 312 developer.

The metal mask was defined by evaporating nickel onto the wafer surface. Prior to evaporation, the wafers were plasma ashed (at 80 W and 250 mTorr) to remove any photoresist residue. Next, 1000Å of nickel was deposited onto the wafer using a Denton SJ-20 e-beam evaporator. An SEM image of the wafer after nickel deposition is shown in Figure 5.19. Finally, the photoresist, and the nickel above it, was removed using heated XX 1112A developer and ultrasonic agitation.

5.5.2 Controlled Etch

As an initial starting point for the etch study, the plasma conditions associated with the nominal operating point for the system identification were used. These turned out to be a bias voltage of 361 V, a chamber pressure of 18.25 mTorr, and a fluorine concentration of 9.59 (arbitrary units). As can be seen in Figure 5.20, the controller compensates for the wall disturbance and drives all three plasma characteristics to their desired setpoints. The corresponding actuator commands are shown in Figure 5.21. After the etch, the wafer was cleaved and imaged using a Joel MSJ-6 scanning electron microscope.

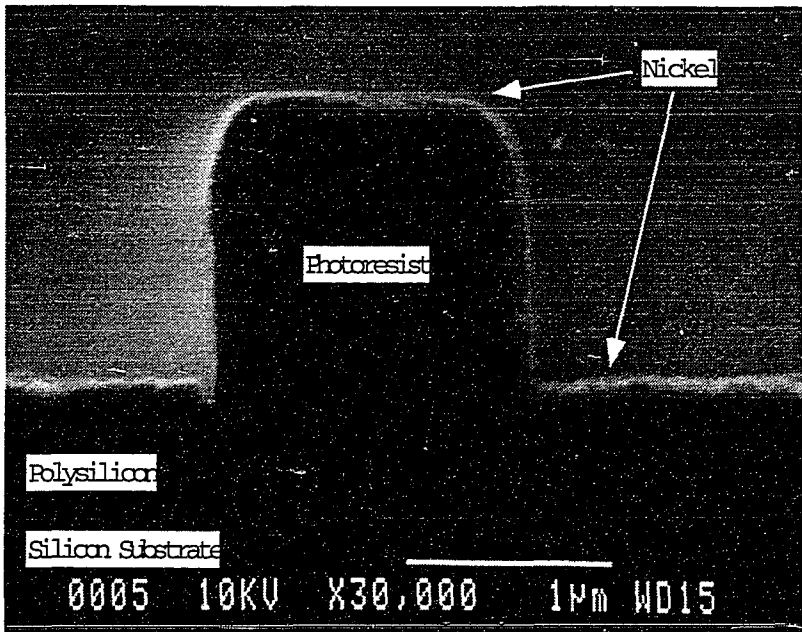


Figure 5.19: Wafer after nickel deposition.

5.5.3 String Model Simulation

The final step is to extract the isotropic and anisotropic etch rate components from the SEM image. This is done by using a string model [59] to obtain a simulated sidewall profile from specified etch rate components. In the string model, the exposed polysilicon surface is represented by a series of nodes connected by straight line segments. The progression of each node is determined by its local etch rate. This etch rate is the vector sum of an isotropic component along the angle bisector of the two adjacent segments and an anisotropic component in regions not masked by the nickel (see Figure 5.23). As the separation between points changes during the etch simulation, nodes are added and subtracted from the string to maintain sufficient resolution and relieve computational load. This model has been implemented in C and uses etch rate components and etch time to produce a profile. The source code is listed in Appendix B.

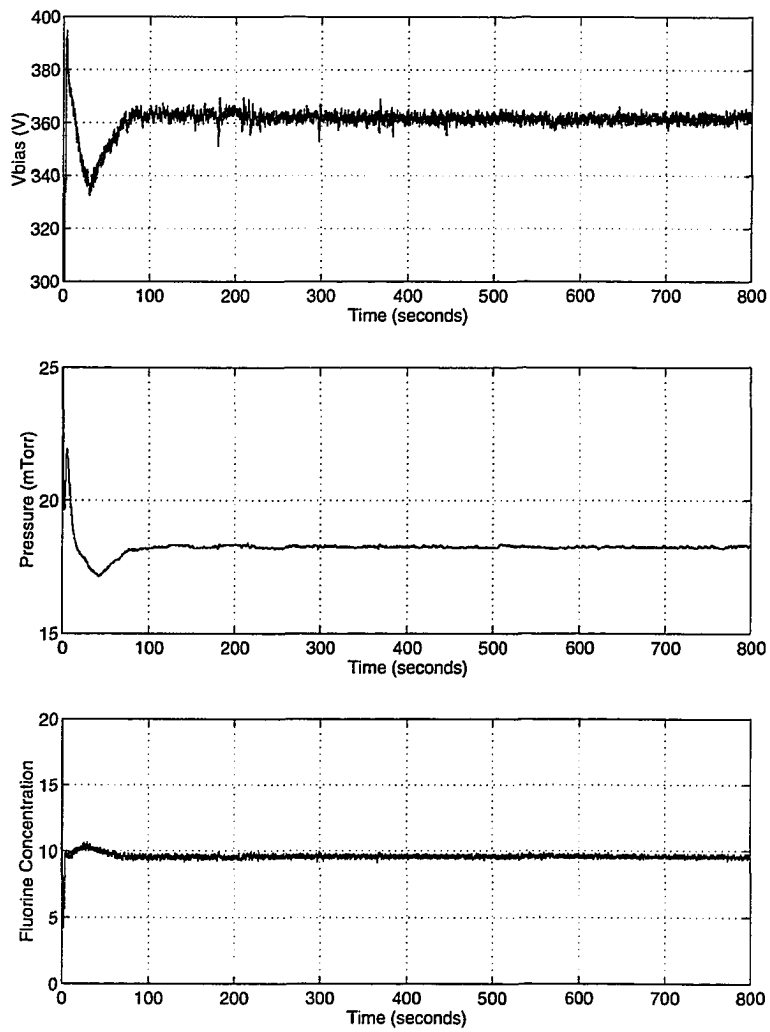


Figure 5.20: Plasma characteristics during feedback control of the plasma generation process.

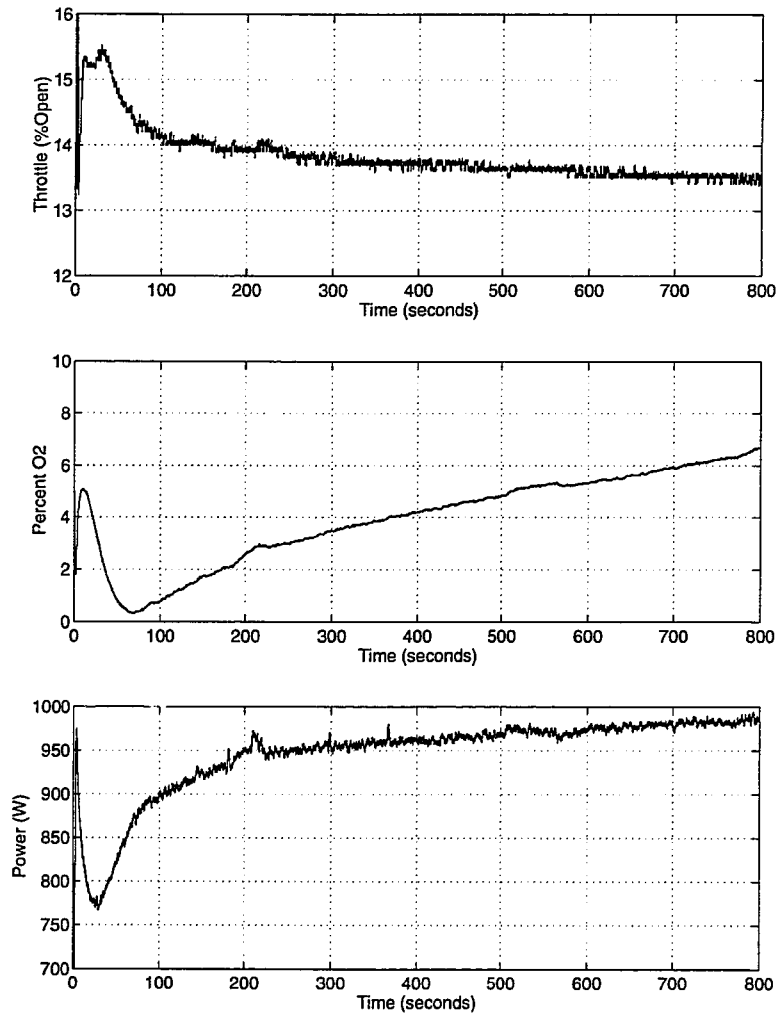


Figure 5.21: Corresponding actuator responses during feedback control.

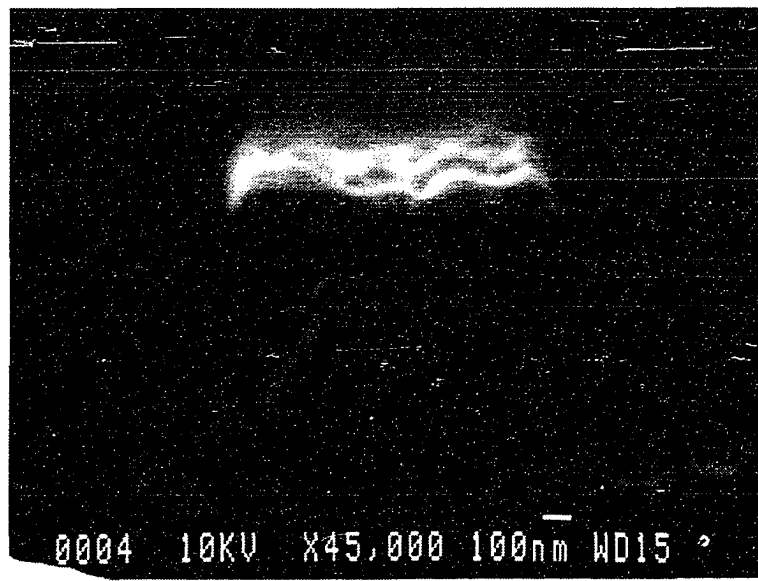


Figure 5.22: SEM image of resulting sidewall profile.

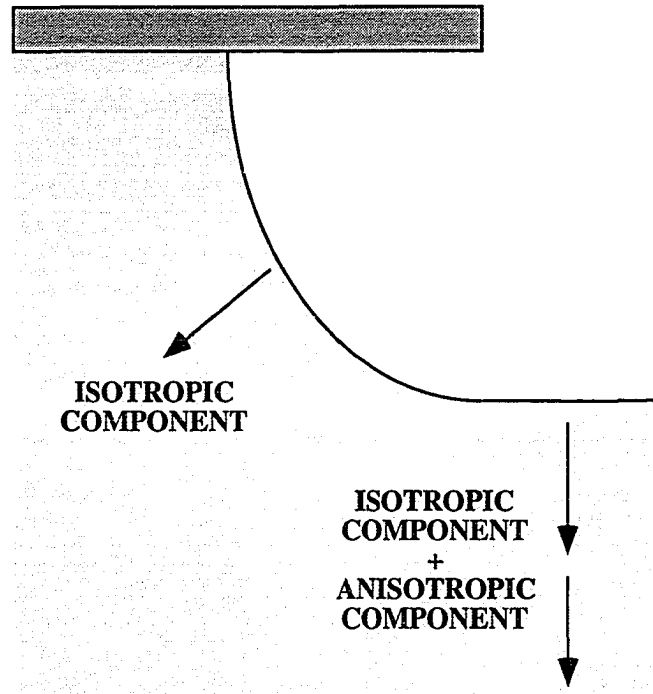


Figure 5.23: Isotropic and anisotropic etch rate components.

5.5.4 Determining Etch Rate from the SEM Image

The SEM image was captured on Polaroid 553 film and then scanned into a digital format. Edges were extracted from this image using the Matlab Image Processing Toolbox [103] to identify the regions of greatest intensity gradient. Then, using the m-files presented in Appendix A.2, the sidewall profile is extracted.

The string simulation is iterated to produce a good fit with the sidewall profile extracted from the SEM image. As can be seen in Figure 5.24, the simulation does an excellent job of capturing slope and shape of the sidewall profile. There is some mismatch between the two in the corners, likely due to the simulation not accounting for local diffusion effects of the reactive species. For this operating point, the etch rate components were found to be 6.0 Å/s isotropic and 6.5 Å/s anisotropic.

5.6 Implementation of the Sidewall Profile Control Strategy

This feasibility study has extended the RIE control work presented in Chapter 4 in two directions. First, it has been shown that, by using %O₂ as an actuator, it is possible to have independent control over the three plasma characteristics: V_{bias}, pressure, and fluorine concentration. Second, it has been shown that the sidewall profile resulting from a fixed set of plasma characteristics may be modeled by decomposing etch rate into isotropic and anisotropic components. The final portion of modeling that remains to be done is to relate the sidewall profile to etch rate components at a number of plasma operating conditions. This data can then be used to construct a response surface [10, 53] relating etch rate components to plasma characteristics.

Completion of the response surface model will allow the implementation of the sidewall

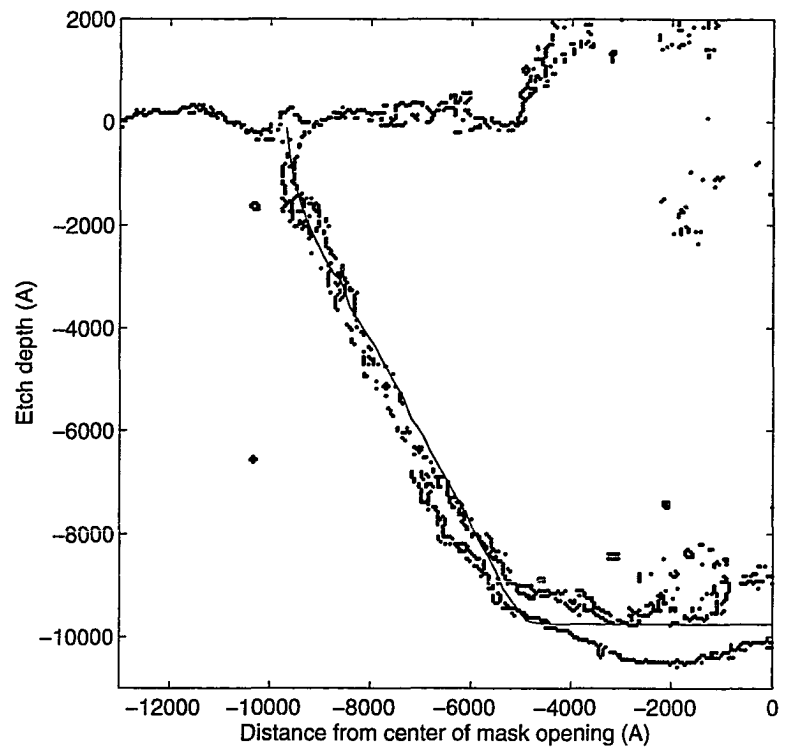


Figure 5.24: Comparison of extracted edge profile with results from string simulation (solid line).

control strategy presented in Section 5.1. First, the string model will be used to determine the etch rate trajectories that must be followed to achieve a desired sidewall profile. The response surface can then be used to translate these etch rate trajectories into the corresponding trajectories that must be followed by the plasma characteristics. Finally, the real-time controller can be used to force the plasma characteristics to follow these trajectories.

The implementation of this control strategy will provide a mechanism for translating desired sidewall profiles into specific etch recipes. Once it is shown that this is possible, the work can be extended to more complicated etch situations. This may include using a more industrially relevant masking layer, such as photoresist, and working with an etch process which takes advantage of sidewall passivation.

CHAPTER 6

Conclusion

From this dissertation, we have concluded that real-time feedback control does provide the potential ability to achieve tighter control over microelectronic fabrication processes. This has been shown by applying feedback control to the reactive ion etching process, an important fabrication step. Because *in situ* sensors were unavailable for measuring etch characteristics, we approached the control problem by regulating the plasma environment in which the etch is performed. The control strategy was based on the hypothesis that, by better regulating characteristics of the plasma, tighter control over the etch is obtained. The first phase of our work validated this approach. Feedback control was used to regulate the plasma properties, which in turn allowed us to reject the effects of disturbances upon the wafer etch process. This ability was demonstrated consistently over a period of several months. In the second phase of the work, this same strategy was applied to controlling sidewall profile. It was shown that sidewall profiles can be represented as etch rate components, which themselves can be related to plasma characteristics.

It was also concluded that the ability to obtain the benefits of feedback control depends strongly upon the control infrastructure: sensors, actuators, control-oriented models, and data acquisition/control software and hardware. The ability to achieve tighter process

control is dependent on the quality of this infrastructure. Only those disturbances which can be sensed or modeled and effected by the actuators can be attenuated by feedback control.

A detailed summary of the specific accomplishments of this dissertation is presented in the following section.

6.1 Summary of Work

The Applied Materials Precision Etch 8300 used in this research had to be modified for implementation of real-time feedback control. A number of actuators were upgraded to provide more control authority and better repeatability. In addition, two custom sensors were added to the system to allow the estimation of fluorine concentration and the measurement of *in situ* etch rate. The fluorine concentration estimate was based on optical emission spectroscopy using a technique known as actinometry. The etch rate was measured using laser interferometry; though this measurement was not available for feedback control, the data was post-processed to determine etch rate after the etch was completed.

Dynamic models of the plasma generation process were empirically determined. Step changes in the settings of each input were individually made and the effect on the plasma properties recorded. Transfer functions were then identified for each input-output pair. The fidelity of this model was investigated by simultaneously applying PRBS to both inputs. The identified model accurately predicted the response of the system to the PRBS inputs. These models were then used to design real-time feedback controller for the plasma generation process. This controller was used to regulate V_{bias} and fluorine concentration during etches.

The main goal of this dissertation was to show that real-time feedback control improved the quality of the reactive ion etching process. The plasma generation process controller was

compared to standard industrial practice (controlling only pressure) in its ability to reject disturbances to etch rate. Four types of disturbances were used for this comparison: 1) a wall disturbance, 2) the loading effect, 3) an oxygen disturbance, and 4) a power disturbance. In each of the cases, the plasma generation process controller was more effective in attenuating the affect of these disturbances on etch rate.

A strategy for sidewall profile control was then developed based on the etch decomposition. In this strategy, a string model simulation is used to determine the isotropic and anisotropic etch rate components that will produce a desired sidewall profile. The plasma characteristics necessary to generate these etch rate components are then determined using a response surface. Finally, the real-time feedback controller is used to regulate the plasma to these condition during an etch. In this dissertation, an etch study is performed to show the feasibility of this strategy. First, oxygen was added to the CF_4 chemistry to allow independent control of three plasma properties (V_{bias} , pressure, and fluorine concentration). Next, a real-time controller was designed based on an empirical model of the CF_4/O_2 plasma generation process. This controller was used to regulate the plasma properties to constant values during the etching of a polysilicon layer masked with nickel. Finally, it was shown how a string model simulation could be used to extract the isotropic and anisotropic etch rate components from the resulting sidewall profile.

6.2 Future Directions

This research has shown that the use of real-time feedback control has the potential for improving the quality of a reactive ion etching process. There are a number of directions in which this work can be extended. A few of these are suggested in the following sections.

6.2.1 Long Term Etch Study

Throughout this research, etch experiments were always performed in sets that spanned only a few days. This was because the ratio between the gains of each channel of the optical emission spectroscopy system varied with time; therefore making it difficult to compare fluorine concentration estimates taken even just weeks apart. Work is in progress towards developing a technique to calibrate the gain of the actinometry system and thus allow comparison of fluorine concentration measurements over time. This calibration procedure should allow a long term etch study to compare the variance of etches performed using our real-time control strategy to those performed using only pressure control. In addition, the open loop process has changed since our original work in ways that do not show up in our models or sensor measurements. This fact has caused the performance of the feedback controller to deteriorate. Work is currently in process to understand possible sources of this process change. This work, along with the optical calibration procedure, should allow an evaluation of the ability of real-time feedback control to decrease long term process variance.

6.2.2 Implementation of Sidewall Profile Control Strategy

There is still a significant amount of work that needs to be done towards implementing the sidewall profile control strategy presented in Chapter 5. The next step in the development of this strategy is to repeat the etch experiments at a range of different plasma conditions. The string model can then be used to determine the etch rate components corresponding to these conditions. From this data, a response surface can be developed to relate plasma characteristics to isotropic and anisotropic etch rate components. It remains to be seen how the string model simulation and response surface might be used to translated a desired sidewall profile into a set of plasma properties.

Once this strategy has been shown to work using a nickel masking layer, it will be important to extend it to a more industrially relevant mask, such as photoresist. In using photoresist, it will be important to understand polymerization mechanisms from the plasma, as photoresist erosion will be a source of carbon near the wafer surface. In addition, the string model simulation will need to be modified to account for mask erosion. This can be done by treating the photoresist as a separate string and simulating its evolution during the etch.

6.2.3 Additional Plasma Sensors

In Chapter 5, it was shown that a third plasma parameter could be independently controlled by adding oxygen to the gas chemistry. At this time, no attempts have been made to control, or even measure, the other two characteristics: ion flux and polymer precursor concentration. As was pointed out in Section 1.2.2, the ion enhanced etch rate is proportional to ion flux. An Advanced Energy RFZ 60 Plasma Impedance Probe will soon be installed on our AME-8300. It is possible that this probe will provide an estimate of ion flux. In addition to ion flux, polymer deposition has a strong influence on the net etch rate and is important in determining sidewall profile. It has been found that the polymer deposition rate can be related to optical emission from CF_2 [78]. It may be possible to develop an *in situ* sensor for polymerization based on the concentration of precursors such as CF_2 . Real-time measurement of both of these plasma characteristics will greatly improve our understanding of the etching process and possibly our ability to control it.

6.2.4 Other Etch Chemistries

This research has been performed using a CF_4 plasma chemistry. Though this chemistry has been the most thoroughly explored in the literature, there are other etch chemistries that might be better suited for real-time control. While F atoms readily etch Si at room temperature, Cl atoms are less reactive and Br atoms will not spontaneously etch silicon at all [21]. For chlorine and bromine chemistries ion bombardment has a stronger influence on the resulting etch characteristics than it does in fluorine etching. It might be possible to saturate the plasma with bromine radicals and control the etch exclusively through the ions. If the ion flux and energy can be electrically measured, this may simplify our control task by allowing us to avoid the uncertainty in the optical measurements, at the expense of uncertainty in the electrical measurements.

6.2.5 High Density Plasma Sources

In capacitively coupled plasmas, such as those used for reactive ion etching, the ion flux and energy can not be independently controlled [67]. Therefore, variations in both ion flux and energy may limit our ability to control the etching process. This may be overcome by using a high density plasma source, such as an ECR or an inductively coupled source. These sources use microwave or inductively coupled rf power to generate the radicals and ions in the bulk plasma, and a capacitively coupled rf source to control ion energy. This allows independent control of both ion flux and energy. However, the use of a high density plasma may complicate the wafer etch process. For example, while in low density plasmas ions do not significantly participate in chemical reactions on the surface, this is not the case for high density plasmas. In these plasmas the etch yield can be as low as 0.2 Si atoms/ion. This corresponds to a fluorine requirement of less than 1 F atom/ion [20], which can be

satisfied by the ions. Therefore, chemical reactions involving the ions become important. In addition, the estimate of reactive species by actinometry is complicated by the dilution of argon being dependent of plasma conditions [58].

APPENDICES

APPENDIX A

M-files Used in This Research

A.1 M-files for System Identification and Control Design

The empirical model building and controller design were done using Matlab. During this research, three Matlab m-files were used to automate the system identification and control design procedures. These m-file were

id_armax.m - Identifies various order ARMAX model based on input-output data.

ctrldsgn.m - Designs controllers based upon the LQG/LTR technique and performs model reduction.

ctrlsat.m - Adds anti-windup logic to a controller designed with **ctrldsgn**.

A.1.1 id_armax.m

```
function [th,simout]=id_armax(z,dt,order,delay,filename,plots,pauses);
%%%%%
%
% Description: id_armax takes input-output data and identifies various
%               order armax models and writes the results to filename.diary
%
% Parameter List:
%
```

```

% Inputs: z      the input/output data to be used for identification
%          in the form: z = [output, input]
%          dt      the sampling period for the data
%          order   vector containing the order models to be identified
%          delay   pure time delay, in samples, present in data
%          filename file name for diary and plots (id_armax will
%                      automatically add extension)
%          plots   0 - don't save plots to files
%                  1 - save plots to files
%          pauses  0 - no pause in program
%                  1 - pause after each plot
%
% Outputs: th     th-format model for last identified order
%           simpout matrix containing simulated output for each order
%
%%%%%%%%%%%%%%%
%
% set default arguments
%
if nargin < 7, pauses = 0; end;
if nargin < 6, plots = 0; end;
if nargin < 5, filename = 'junk'; end;
if nargin < 4, delay = 1; end;

%
% Plot Measured Response
%
y = z(:,1);
[xs,ys] = size(z);
t = dt*[0:xs-1]';
plot(t,z(:,1)),grid;
title(['Measured Response of System'])
xlabel('Time (seconds)')
ylabel('Output')

if plots == 1,
plotfile = [filename, '.actual.ps'];
diary on
disp(['Printing Plot of Measured Response in file ', plotfile])
diary off
eval(['print ', plotfile]);
end % End If - Print Plot

if pauses == 1, disp('Hit Any Key to Continue'), pause, end

%
% Start Identification

```

```

%
for j = 1:max(size(order)), % Loop through for each element in order

    i = order(j);
    th = armax(z,[i i i delay],50,-1,-1,-1,dt);

    eval(['diary ', filename,'.diary']);
    disp(['Theta - Armax Model - Order ',int2str(i)])
    disp(['-----'])
    disp([' '])
    present(th)
    diary off

% Evaluate System

na = [1:i];
nb = [i+1:2*i];
a = [1 th(3,na)];
b = [th(3,nb)];
[bc,fc] = contin(th,1,1);

diary on
disp(' ')
disp('Discrete G(z)')
disp('Numerator')
disp(b)
disp('Denominator')
disp(a)
disp('Zeros')
disp(roots(b))
disp('Poles')
disp(roots(a))
disp(' ')
disp('Continuous G(s)')
disp('Numerator')
disp(bc)
disp('Denominator')
disp(fc)
disp('DC gain')
disp(polyval(bc,0)/polyval(fc,0))
disp('Zeros')
disp(roots(bc))
disp('Poles')
disp(roots(fc))
disp(['delay = ', int2str(delay)])
disp(' ')
disp(' ')

```

```

diary off

[mag(:,i) phase(:,i)] = bode(bc,fc,logspace(-3,3,200));
loss(j) = th(1,1);

%
% Simulate System with Identified Theta
%
[ysim] = idsim(z(:,2),th);

plot(t,ysim,t,z(:,1),'y
:');
grid;
title(['Measured and Simulated Response of Order ',int2str(i), ...
    ' ARMAX Model'])
xlabel('Time (seconds)')
ylabel('Simulated Output')
legend('Simulated Response','Actual Response')
simout(:,j) = ysim;

if plots == 1,
    plotfile = [filename,'.sim',int2str(i),'.ps'];
    diary on
    disp(['Printing Simulated Response of Order ',int2str(i), ...
        ' in file ', plotfile])
    diary off
    eval(['print ', plotfile]);
end % End If - Print Plot

if pauses == 1, disp('Hit Any Key to Continue'), pause, end

%
% Find Residuals
%
titl = ['Correlation of Residuals for Order ',int2str(i), ' ARMAX Model'];
[e,r] = resid2(z,th,titl);

if plots == 1,
    plotfile = [filename,'.resid',int2str(i),'.ps'];
    diary on
    disp(['Printing resid for Order ',int2str(i), ' in file ', plotfile])
    disp(' ')
    diary off
    eval(['print ', plotfile]);
end % End If - Print Plots
end % End For Loop

```

```

if pauses == 1, disp('Hit Any Key to Continue'), pause, end

%
% bode
%

subplot([211])
loglog(logspace(-3,3,200),mag)
title(['Bode plots of orders [ ', int2str(order) , ']'])
ylabel('mag'), xlabel('rad/sec'), grid
subplot([212])
semilogx(logspace(-3,3,200),phase)
ylabel('phase'), xlabel('rad/sec'), grid

if plots == 1,
plotfile = [filename,'.bode.ps'];
diary on
disp(['Printing bode for Orders [',int2str(order), ...
'] in file ', plotfile])
disp(' ')
diary off
eval(['print ', plotfile]);
end % End If - Print Plots

%
% Log Loss Functions
%
format short e
diary on
disp([' Order Loss Function'])
disp([order',loss']);
diary off
format short

end;

```

A.1.2 ctrldsgn.m

```

function [Acr,Bcr,Ccr,Dcr] = ctrldsgn(Ap,Bp,Cp,Dp,alpha,Qq,Rr,rho)
%%%%%%%%%%%%%
%
% Description: LQG/LTR controller design with model reduction
%
% Parameter List:
%
% Inputs: [Ap,Bp,Cp,Dp] - state space representation of the plant

```

```

%
% LQR Design
% State Weights Q = [alpha*Cp'*Cp,zeros(ns,no);zeros(no,ns),Qq];
% Input Weights R = Ru;
%
% LQG/LTR Design
% W = Bp*Bp'
% V = rho*I
%
% Outputs: [Acr,Bcr,Ccr,Dcr] - state space representation of the reduced
% order controller
%
%%%%%%%%%%%%%%%
w = logspace(-2,2);
time = [0:1/20:40];

%
% Determine size of plant
%

[ns,ni] = size(Bp);
[no,ns] = size(Cp);

%
% Augment the plant with integrators
%
% \dot{x} = Ap x + Bp u
% \dot{q} = y - r
% y = Cp x
%

Am = [Ap, zeros(ns,no); Cp, zeros(no,no)];
Bm = [Bp; zeros(no,ni)];
Cm = [Cp, zeros(no,no)];
Dm = zeros(no,ni);

%
% LQR Design
%

Q = [alpha*Cp'*Cp, zeros(ns,no); zeros(no,ns), Qq];
R = Ru;
[K,S] = lqr(Am,Bm,Q,R);

%
% Analysis of LQR Design
%

```

```

% Loop Gain of State Feedback Design
%
for i = 1:ni,
    str = ['Loop Gain: Input ',num2str(i)];
    [mag,ph] = mbode(Am,Bm,-K,Dm,i,i,w,str);
    disp('Hit Any Key To Continue');
    pause;
end

%
% Step Response of Closed Loop System
%
Asf = [Am-Bm*K];
Bsfc = [zeros(ns,ni); -eye(ni)];
Csf = Cm;
Dsf = Dm;

for i=1:ni,
    y = step(Asf,Bsf,Csf,Dsf,i,time);
    titl = ['Response of outputs to a step in reference ',num2str(i)];
    for j = 1:no,
        subplot(no,1,j), plot(time,y(:,j)),grid
        if j == 1, title(titl), end
        xlabel('Time (seconds)');
        ylabel(['Output ',num2str(j)]);
    end
    keyboard
end

u = step(Asf,Bsf,-K,Dsf,i,time);
titl = ['Response of inputs to a step in reference ',num2str(i)];
for j = 1:ni,
    subplot(ni,1,j), plot(time,u(:,j)),grid
    if j == 1, title(titl), end
    xlabel('Time (seconds)');
    ylabel(['Input ',num2str(j)]);
end
keyboard
end

%
% Loop Transfer Recovery
%
[L,Y] = lqr(Ap',Cp',Bp*Bp',rho*eye(no));
nas = ns+no;

```

```

K1 = K(:,1:ns);
K2 = K(:,ns+1:nas);

Ac = [Ap-Bp*K1-L'*Cp, -Bp*K2; zeros(no,nas)];
Bc = [L', zeros(ns,no); eye(no), -eye(no)];
Cc = -K;
Dc = zeros(ni,2*no);

%
% Loop Gain at Output
%

Ao = [Ac, zeros(nas,ns); Bp*Cc, Ap];
Bo = [L';eye(no);zeros(ns,no)];
Co = [zeros(no,nas), Cp];
Do = zeros(no,no);

for i = 1:no,
    str = ['Loop Gain: Output ',num2str(i)];
    [mag,ph] = mbode(Ao,Bo,Co,Do,i,i,w,str);
    keyboard
    % disp('Hit Any Key To Continue');
    % pause;
end

%
% Closed Loop System
%

Acl = [Ac, [L';eye(no)]*Cp; Bp*Cc, Ap];
Bcl = [zeros(ns,no);-eye(no);zeros(ns,no)];
Ccl = [zeros(no,nas), Cp];
Dcl = zeros(no,no);

for i=1:ni,
    y = step(Acl,Bcl,Ccl,Dcl,i,time);
    titl = ['Response of outputs to a step in reference ',num2str(i)];
    for j = 1:no,
        subplot(no,1,j), plot(time,y(:,j)),grid
        if j == 1, title(titl), end
        xlabel('Time (seconds)');
        ylabel(['Output ',num2str(j)]);
    end
    disp('Keyboard Cmds - type return to continue')
    keyboard
    u = step(Acl,Bcl,[-K,zeros(ni,ns)],Dcl,i,time);

```

```

titl = ['Response of inputs to a step in reference ',num2str(i)];
for j = 1:ni,
    subplot(ni,1,j), plot(time,u(:,j)),grid
    if j == 1, title(titl), end
    xlabel('Time (seconds)');
    ylabel(['Input ',num2str(j)]);
end
disp('Keyboard Cmds - type return to continue')
keyboard

end

disp('Calculating BalReal');
%
% Balanced Realization
%

Ae = Ap-Bp*K1-L'*Cp;
Be = [Bp, L'];
Ce = -K1;
De = [eye(no), zeros(ni,no)];

Ai = zeros(no,no);
Bi = [eye(no), -eye(no)];
Ci = [-K2; zeros(no,no)];
Di = [zeros(no,2*no); eye(no), zeros(no,no)];

[Ab,Bb,Cb,G,T] = balreal(Ae,Be,Ce);
disp('Singular Values of (Ab,Bb,Cb)');
disp(G)
nsk = input('Enter number of states to keep: ','s');
nk = str2num(nsk);

%
% Controller Model Reduction
%

elim = [nk+1:length(G)];
[Ar,Br,Cr,Dr] = modred(Ab,Bb,Cb,De,elim);
[nsr,ni] = size(Br);

Acr = [Ar, Br*Ci; zeros(no,nsr), zeros(no,no)];
Bcr = [Br*Di; eye(no), -eye(no)];
Ccr = [Cr, Dr*Ci];
Dcr = [Dr*Di];

Aro = [Acr, zeros(nsr+no,ns); Bp*Ccr, Ap];

```

```

Bro = [Bcr(:,[1,no]);zeros(ns,no)];
Cro = [zeros(no,nsr+no), Cpl];
Dro = zeros(no,no);

for i = 1:no,
    clg;
    [mag,ph] = bode(Ac,Bc,Cc,Dc,i,w);
    [magr,phr] = bode(Acr,Bcr,Ccr,Dcr,i,w);
    mag = 20*log10(mag);
    magr = 20*log10(magr);

    for j = 1:no,
        subplot(no,1,j),semilogx(w,mag(:,j),'-',w,magr(:,j), '--'),grid
        if j==1,12=legend('Full order','Reduced Order'),end;
    end

    disp('Keyboard Cmds - type return to continue')
    keyboard

end

```

A.1.3 ctrlsat.m

```

function [au,bu,cu,du,ku] = ctrlsat(ac,bc,cc,dc,Qu,Ru);
%%%%%%%%%%%%%
%
% Description: Add anti-windup logic to controller
%
% Parameter List:
%
%   Inputs: [ac,bc,cc,dc] controller
%           Qu          state weights
%           Ru          command error weights
%   Outputs: [au,bu,cu,du] anti-windup controller
%            ku          anti-windup gain
%
%%%%%%%%%%%%%
ku = lqr(ac',cc',Qu,Ru);
ku = ku';

[ci,cj] = size(cc);

au = ac-ku*cc;
bu = [bc-ku*dc ku];
cu = cc;

```

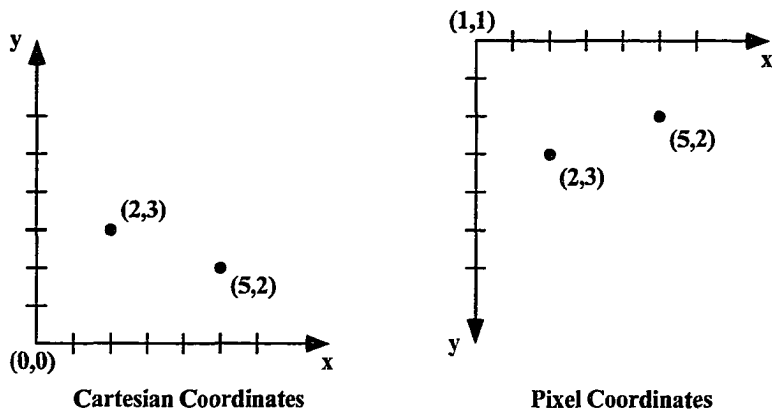


Figure A.1: Cartesian and pixel coordinate systems.

```

du = [dc 0*eye(ci)];
disp(ku)
end

```

A.2 M-files for Extraction of Sidewall Profile

The Matlab Image Processing Toolbox was used to analyze the SEM images. The first step was to extract the areas of greatest intensity gradient using the `edge` command. This command produces an binary image matrix (with element of either 0 or 1) with the edge denoted with 1's. This matrix used the pixel coordinate system shown in Figure A.1. A plot of the image matrix for the edge of the SEM image in Figure 5.22 is shown in Figure A.2. A series of custom m-files were used to extract the etch profile from the image matrix.

These m-files were

`clpt.m` - Returns the Cartesian coordinates of a point selected with the mouse.

`edfill.m` - Fills in gaps in the edge profile.

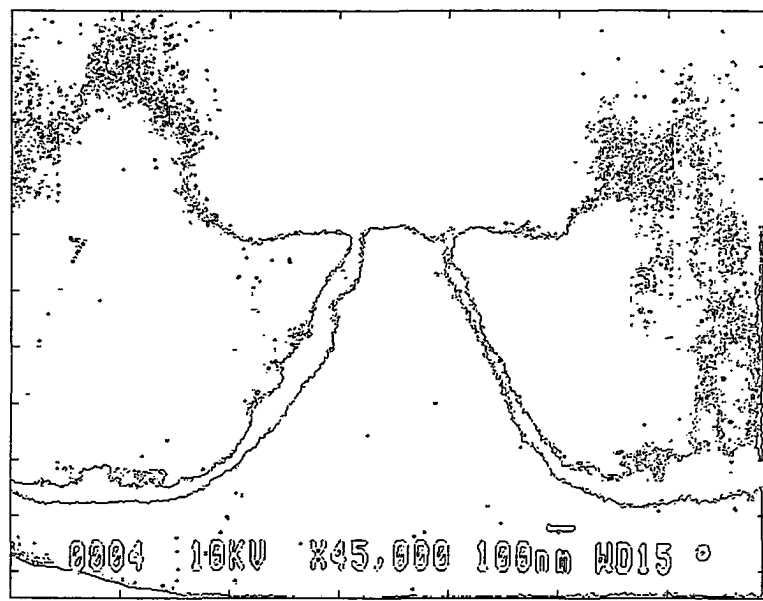


Figure A.2: Edge profile

edscale.m - Scales the image matrix from pixels to microns.

edshow.m - Returns Cartesian coordinates of edges from image matrix.

mat2pic.m - Converts from Cartesian coordinates to pixel coordinates.

pic2mat.m - Converts from pixel coordinates to Cartesian coordinates.

snake.m - Extracts specific edge profile from the image matrix.

A.2.1 clpt.m

```
function [i,j] = clpt(BW);
%%%%%
%
% Description: Return cartesian coordinates of points selected with mouse
%
% Parameter List:
%
% Inputs: BW = matrix containing edge image
%
% Outputs: [i,j] = selected points in cartesian coordinates
```

```

%
% Subfunctions: pic2mat.m
%                 mat2pic.m
%
%%%%%%%%%%%%%%%
[si,sj] = size(BW);
[gx,gy]=ginput(1);

gx = floor(gx);
gy = floor(gy);

[gi,gj] = pic2mat(gx,gy,si,sj);

found = 0;

if BW(gi,gj) == 1,
i=gi;
j=gj;
else
R = 1;
while found == 0,
theta = 0;
while (theta < 2*pi) & (found == 0),
i = round(gi + R*cos(theta));
j = round(gj - R*sin(theta));
[xtest,ytest] = mat2pic(i,j,si,sj);
if BW(i,j) == 1,
found = 1;
else
theta = theta+(pi/20);
end
end
R = R+1;
end
end

end

```

A.2.2 edfill.m

```

function [BW2] = edfill(BW);
%%%%%%%%%%%%%%%
%
% Description: Fill in gaps in the edge profile image
%

```

```

% Parameter List:
%
%   Inputs: BW = matrix containing edge image
%
%   Outputs: BW2 = new image matrix
%
% Subfunctions: clpt.m
%                 edshow.m
%
%%%%%%%%%%%%%%%
edshow(BW);

BW2 = BW;

disp('Select First Point')

[i1,j1] = clpt(BW);

disp('Select Second Point')

[i2,j2] = clpt(BW);

i2-i1
j2-j1

if abs(i2-i1) > abs(j2-j1),

    v = polyfit([i1,i2],[j1,j2],1);

    imin = min(i1,i2);
    imax = max(i1,i2);

    x = [imin:imax]';

    y = round(polyval(v,x));

    for k = 1:length(x);
        BW2(x(k),y(k))=1;
    end

else

    v = polyfit([j1,j2],[i1,i2],1);

    jmin = min(j1,j2);
    jmax = max(j1,j2);

```

```

y = [jmin:jmax]';

x = round(polyval(v,y));

for k = 1:length(x);
    BW2(x(k),y(k))=1;
end

end

edshow(BW2);

end

```

A.2.3 edsclae.m

```

function [cent,scale] = edsclae(BW);
%%%%%
%
% Description: Find scale factors from pixels to microns
%
% Parameter List:
%
%   Inputs: BW = matrix containing edge image
%
%   Outputs: cent = origin for scaled image
%             scale = scale factor from pixels to microns
%
% Subfunctions: edshow.m
%               clpt.m
%
%%%%%

function [cent,scale] = edsclae(BW);

edshow(BW);

disp('Select Center Point')
[ic,jc] = ginput(1);
cent = [ic,jc];

disp('Select First Point')
[i1,j1] = clpt(BW);

disp('Select Second Point')
[i2,j2] = clpt(BW);

```

```

sc = input('Enter distance between pts. 1 and 2: ','s');

dist = sqrt((i2-i1)^2 + (j2-j1)^2);
scale = str2num(sc)/dist;

end

```

A.2.4 edshow.m

```

function [x,y]=edshow(BW);
%%%%%
%
% Description: Plot a edge detection image in cartesian (pic) coordinates
%
% Parameter List:
%
%   Inputs: BW = matrix containing edge image
%
%   Outputs: [x,y] = coordinates (pic) of each pixel = 1 in matrix
%
% Subfunctions: mat2pic.m
%
%%%%%
%
[si,sj] = size(BW);
k = 0;

for i = 1:si-1,
    for j = 1:sj-1,
        if BW(i,j) == 1,
            k =k+1;
        [x(k),y(k)] = mat2pic(i,j,si,sj);
        end
    end
end
plot(x,y,'.')

```

A.2.5 mat2pic.m

```

function [x,y] = mat2pic(i,j,si,sj);
%%%%%
%
% Description: Convert between matrix coordinates of a BW file

```

```

%           to plot (pic) coordinates
%
% Parameter List:
%
%   Inputs: i = row number in matrix
%   j = column number in matrix
%   si = total number of rows of matrix
%           sj = total number of columns of matrix
%
%   Outputs: x = x-coordinate corresponding to column
%   y = y-coordinate corresponding to row
%
%%%%%%%%%%%%%%%
x = j;
y = si-i;

end

```

A.2.6 pic2mat.m

```

function [i,j] = pic2mat(x,y,sx,sy);
%%%%%%%%%%%%%%
%
% Description: Convert between matrix coordinates of a BW file
%           to plot (pic) coordinates
%
% Parameter List:
%
%   Inputs: x = x-coordinate
%   y = y-coordinate
%   sx = size in x direction
%           sy = size in y direction
%
%   Outputs: i = column corresponding to x-coordinate
%   j = row corresponding to y-coordinate
%
%%%%%%%%%%%%%%
j = x;
i = sx-y;

end

```

A.2.7 snake.m

```
function [x,y] = snake(BW,Nmax);
%%%%%
%
% Description: Extract a specific edge profile from the image matrix
%
% Parameter List:
%
%   Inputs: BW      = matrix containing edge image
%          Nmax    = number of points to find along the edge
%
%   Outputs: [x,y] = coordinates of the edge
%
%%%%%
if nargin < 2, Nmax = 100; end

[si,sj]=size(BW);

disp('Displaying Edge Profile - Please Be Patient')
edshow(BW);

disp(' ');
disp('Select Starting Point With Mouse')
disp(' ');

[gx,gy]=ginput(1);

gx = floor(gx);
gy = floor(gy);

[gi,gj] = pic2mat(gx,gy,si,sj);

% find nearest point

found = 0;

if BW(gi,gj) == 1,
i=gi;
j=gj;
else
R = 1;
while found == 0,
theta = 0;
        while (theta < 2*pi) & (found == 0),
i = round(gi + R*cos(theta));
                j = round(gj - R*sin(theta));
```

```

[xtest,ytest] = mat2pic(i,j,si,sj);
if BW(i,j) == 1,
found = 1;
else
theta = theta+(pi/20);
end
end
R = R+1;
end
end

[x,y] = mat2pic(i,j,si,sj);

hold on
plot([gx x],[gy y],'r')
hold off

%
% Move along edge
%

disp(' ');
disp('Starting to move along edge')
disp(' ');

ep = 1E-10;

j_old = j;
i_old = i-1;
thold = 0;

hold on

for n = 2:Nmax
found = 0;
thold = (atan2((j_old-j),(i-i_old+ep))+thold)/2;
i_old = i;
j_old = j;
R = 1;
d = 1;
while found == 0,
theta = thold;
dtheta = pi/20;
d = 1;
if R <= 2,
thmax = 5*pi/8;
else
thmax = 3*pi/4;

```

```

end
while (abs(dtheta) < thmax) & (found == 0),
i = round(i_old + R*cos(theta));
j = round(j_old - R*sin(theta));
if BW(i,j) == 1,
found = 1;
else
theta = thold + (d*dtheta);
dtheta = dtheta+(pi/20);
d = -1*d;
end
end
R = R+1;
end
th(n) = theta;
[x(n),y(n)] = mat2pic(i,j,si,sj);
plot(x(n-1:n),y(n-1:n),'w');
end

x = x';
y = y';
th = th';
end

```

APPENDIX B

Surface Evolution Simulation

The evolution of the surface during an etch was simulated by using a string model. The following is the C implementation string model used in this research. The header file is presented first followed by the main program.

B.0.8 string.h

```
/* Header File for String Model */

/* Globally Defined Constants */

#define PI      3.14159

/* Define Global Variables */

int    NODES,ITERATIONS,NNODE;
float WIDTH,TIME,ISO,ANISO,DMIN,DMAX;
float PR_HEIGHT,PR_WIDTH,PR_ISO,PR_ANISO;

/* Define Structures */

struct position
{
    float x,y;
};

struct node
{
```

```

    struct node *prev;
    struct position last;
    float theta;
    int nodenum;
    struct position new;
    struct node *next;
};

/* Declare Functions */

void initialize(struct node *pntr);
void angle(struct node *pntr);
void iso_evolve(struct node *pntr);
void aniso_evolve(struct node *pntr);
void evolve(struct node *pntr);
void update(struct node *pntr);
void addnode(struct node *pntr);
void remnode(struct node *pntr);
float dist(struct node *pntr);
int leftbound(struct node *pntr);
int rightbound(struct node *pntr);
void PRinitialize(struct node *pntr);

```

B.0.9 string.c

```

/* String Model Programs      */
/*                           */
/* Created By: Brian Rashap */
/* Date:       6/20/94        */

#include <stdio.h>
#include <math.h>
#include "string.h"

main()
{
    struct node first,*point;
    int i,k,numofnodes,*nnum;
    float distance,timestep;

    char *calloc ();

    /* Scan in Simulation Data      */

```

```

/*  WIDTH = mask linewidth (um)          */
/*  NODES = initial number of nodes      */
/*  ITERATIONS = iterations of evolution */
/*  TIME = etch length (seconds)        */
/*  ISO = isotropic etch rate (A/sec)   */
/*  ANISO = anisotropic etch rate (A/sec)*/
/*  DMAX = max. distance between nodes */
/*  DMIN = min. distance between nodes */

scanf("%f %d %d",&WIDTH, &NODES, &ITERATIONS);
scanf("%f %f %f",&TIME,&ISO,&ANISO);
scanf("%f %f",&DMAX, &DMIN);

timestep = TIME/ITERATIONS;    /* Time step in seconds      */
ISO = ISO * timestep;         /* Isotropic ER in A/step   */
ANISO = ANISO * timestep;     /* Anisotropic ER in A/step */

/* Initialize First Node */

point = (struct node *) malloc (sizeof (struct node));
first.theta = -PI/2;
first.next = point;
first.last.x = -(WIDTH/2.0);
first.last.y = 0.0;
first.prev = &first;
first.nodenum = 1;

/* Initialize Rest of Starting String */

initialize(first.next);
(first.next)->prev = &first;
angle(first.next);

NNODE = NODES+1;

/* Surface Evolution */

for (k = 1; k < ITERATIONS; k++)
{
/*      printf("Calculating Iteration %d \n",k); */
point = &first;
evolve(point);
update(point);
}

/* Display final surface */

```

```

while ( point != (struct node *) 0 )
{
    distance = dist(point);
    printf("%d %.4f %.4f %.4f %4.3f %d %d \n",(*point).nodenum, \
           (*point).last.x,(*point).last.y,(*point).theta,distance, \
           leftbound(point),rightbound(point));
    point = (*point).next;
}
}

/* Subroutine - initialize string */

void initialize(struct node *pntr)
{
    int i;

    for (i = 2; i < NODES; i++)
    {
        (*pntr).last.x = -(WIDTH/2.0)+(i-1)*(WIDTH/(NODES-1));
        (*pntr).last.y = 0.0;
        (*pntr).theta = 0.0;
        (*pntr).nodenum = i;
        (*pntr).next = (struct node *) malloc (sizeof (struct node));
        (*pntr->next).prev = pntr;
        pntr = (*pntr).next;
    }
    (*pntr).theta = i;
    (*pntr).nodenum = i;
    (*pntr).last.x = (WIDTH/2.0);
    (*pntr).last.y = 0.0;

    (*pntr).next = (struct node *) 0;
}

/* Subroutine - Determine surface normals */

void angle(struct node *pntr)
{
    double x1,y1,x2,y2,x3,y3;
    float a12,a23;

    while ( (*pntr).next != (struct node *) 0 )
    {
        x1 = (*pntr->prev).last.x;
        y1 = (*pntr->prev).last.y;

```

```

x2 = (*pntr).last.x;
y2 = (*pntr).last.y;
x3 = (*pntr->next).last.x;
y3 = (*pntr->next).last.y;
a12 = atan2((y2-y1),(x2-x1));
a23 = atan2((y3-y2),(x3-x2));
(*pntr).theta = (a12+a23)/2;
pntr = (*pntr).next;
}
(*pntr).theta = PI/2;
}

/* Isotropic surface evolution */

void iso_evolve(struct node *pntr)
{
    float th;

    th = (*pntr).theta;
    (*pntr).new.x = (*pntr).last.x + ISO*sin(th);
    (*pntr).new.y = (*pntr).last.y - ISO*cos(th);
}

/* Anisotropic surface evolution */

void aniso_evolve(struct node *pntr)
{
    (*pntr).new.y = (*pntr).new.y - ANISO;
}

/* Evolve surface one iteration */

void evolve(struct node *pntr)
{
    float th;

    while ( pntr != (struct node *) 0 )
    {
        iso_evolve(pntr);
        if (leftbound(pntr) == 0 && rightbound(pntr) == 0)
aniso_evolve(pntr);
        if (dist(pntr) > DMAX)
addnode(pntr);
        if (dist(pntr) < DMIN)
remnode(pntr);
    }
}

```

```

        pptr = (*pptr).next;
    }
}

/* Update nodes to reflect current positions */

void update(struct node *pptr)
{
    struct node *first;

    first = pptr;
    while ( pptr != (struct node *) 0 )
    {
        (*pptr).last.x = (*pptr).new.x;
        (*pptr).last.y = (*pptr).new.y;
        pptr = (*pptr).next;
    }
    angle((*first).next);
}

/* Determine distance between adjacent nodes */

float dist(struct node *pptr)
{
    float distance;
    float x1,y1,x2,y2;

    x1 = (*pptr->prev).new.x;
    y1 = (*pptr->prev).new.y;
    x2 = (*pptr).new.x;
    y2 = (*pptr).new.y;

    distance = sqrt(pow(y2-y1,2) + pow(x2-x1,2));
    return(distance);
}

/* Add a node to surface string */

void addnode(struct node *pptr)
{
    struct node *newnode;
    float x1,y1,x2,y2,th;

    newnode = (struct node *) malloc (sizeof (struct node));

```

```

x1 = (*pntr->prev).last.x;
y1 = (*pntr->prev).last.y;
x2 = (*pntr).last.x;
y2 = (*pntr).last.y;

(*newnode).last.x = (x1+x2)/2;
(*newnode).last.y = (y1+y2)/2;
(*newnode).theta = atan2((y2-y1),(x2-x1));

(*newnode).prev = (*pntr).prev;
(*newnode).next = pntr;
(*newnode).nodenum = NNODE;
(*pntr->prev).next = newnode;
(*pntr).prev = newnode;

(NNODE)++;

iso_evolve(newnode);
if (leftbound(newnode) == 0 && rightbound(newnode) == 0)
    aniso_evolve(newnode);
}

/* Remove a node from surface string */

void remmcde(struct node *pntr)
{
    (*pntr->next).prev = (*pntr).prev;
    (*pntr->prev).next = (*pntr).next;
}

/* Determine if node is shadowed on left */

int leftbound(struct node *pntr)
{
    int isleft;

    isleft = 0;
    if ((*pntr).last.x < -WIDTH/2)
        isleft = 1;

    return(isleft);
}

/* Determine if node is shadowed on right */

```

```
int rightbound(struct node *pnter)
{
    int isright;

    isright = 0;
    if ((*pnter).last.x > WIDTH/2)
        isright = 1;

    return(isright);
}
```

BIBLIOGRAPHY

BIBLIOGRAPHY

- [1] A.C. Adams and C.D. Capio. Edge profiles in the plasma etching of polycrystalline silicon. *Journal of the Electrochemical Society*, 128(2):366–370, February 1981.
- [2] K.D. Allen and H.H. Sawin. The plasma etching of polysilicon with CF₃Cl/Ar discharges. II. Modeling of ion bombardment energy distributions. *Journal of the Electrochemical Society*, 133(11):2326–2338, November 1986.
- [3] K.D. Allen, H.H. Sawin, M.T. Mocella, and M.W. Jenkins. The plasma etching of polysilicon with CF₃Cl/Ar discharges. I. Parametric modeling and impedance analysis. *Journal of the Electrochemical Society*, 133(11):2315–2325, November 1986.
- [4] B.D.O. Anderson and J.B. Moore. *Optimal Control: Linear Quadratic Methods*. Prentice Hall, 1990.
- [5] J.C. Arnold. *Material Transport and Reaction Effects on Surface Topography Evolution During Plasma Etching*. Ph.D. Dissertation, Massachusetts Institute of Technology, 1994.
- [6] K.J. Astrom and B. Wittenmark. *Computer-Controlled Systems: Theory and Design*. Prentice Hall, 1990.
- [7] D.M. Auslander and C.H. Tham. *Real Time Software for Control: Program Examples in C*. Prentice-Hall, 1990.
- [8] A.J. Bariya, C.W. Frank, and J.P. McVittie. A surface kinetic model for plasma polymerization with application to plasma etching. *Journal of the Electrochemical Society*, 137(8):2575–2581, August 1990.
- [9] T.E. Benson, P.D. Hanish C.K. Hanish, L.I. Kamlet, P. Klimecky, B.A. Rashap, S.M. Ruegsegger, J.S. Freudenberg, J.W. Grizzle, P.P. Khargonekar, F.L. Terry, Jr., and B. Barney. Sensor systems for real-time feedback control of reactive ion etching. In *Proceedings of the NCCAVS Advanced Plasma Tools Workshop*, 1995.
- [10] G.E.P. Box and N.R. Draper. *Empirical Model-Building and Response Surfaces*. John Wiley & Sons, 1987.
- [11] T. Breedijk. *Model Identification and Nonlinear Predictive Control of Rapid Thermal Processing Systems*. Ph.D. Dissertation, University of Texas at Austin, 1994.
- [12] S.W. Butler. *Etching and Polymerization in Fluorocarbon-Hydrogen Plasma: Mathematical Modeling and Experimental Investigation*. Ph.D. Dissertation, University of Texas at Austin, 1991.

- [13] S.W. Butler, K.J. McLaughlin, T.F. Edgar, and I. Trachtenberg. Development of techniques for real-time monitoring and control in plasma etching: II. Multivariable control system analysis of manipulated, measured, and performance variables. *Journal of the Electrochemical Society*, 138(9):2727–2735, September 1991.
- [14] F.G. Celii, T.-C. Kao, A.J. Katz, T.S. Moise, M. Woolsey, and B. Johs. Ellipsometry-based control for III-V MBE growth. In *Extended Abstracts: 187th Meeting of the Electrochemical Society*, pages 203–204, May 1995.
- [15] M. Chandhok, P.D. Hanish, and J.W. Grizzle. Phenomenological modeling for real-time control of RIE. In *Extended Abstracts: 187th Meeting of the Electrochemical Society*, pages 162–164, May 1995.
- [16] B. Chapman. *Glow Discharge Processes: Sputtering and Plasma Etching*. John Wiley & Sons, 1980.
- [17] C.T. Chen. *Linear Systems Theory and Design*. Harcourt Brace Jovanovich, 1984.
- [18] X. Cheng, T.J. Knight, B.H. Krogh, D.W. Greve, and M.A. Gibson. Application of sampling quadrupole mass spectrometry to multivariable process control. In *Extended Abstracts: 187th Meeting of the Electrochemical Society*, pages 201–202, May 1995.
- [19] Y.M. Cho and T. Kailath. Model identification in rapid thermal processing systems. *IEEE Transactions on Semiconductor Manufacturing*, 6(3):233–245, August 1993.
- [20] J.W. Coburn. Role of ions in reactive ion etching. *Journal of Vacuum Science and Technology A*, 12(4):1417–1424, July/August 1994.
- [21] J.W. Coburn. Surface-science aspects of plasma-assisted etching. *Applied Physics A*, 59:451–458, November 1994.
- [22] J.W. Coburn and M. Chen. Optical emission spectroscopy of reactive plasmas: A method for correlating emission intensities to reactive particle density. *Journal of Applied Physics*, 51(6):3134–3136, June 1980.
- [23] J.W. Coburn and H.F. Winters. Plasma etching - A discussion of mechanisms. *Journal of Vacuum Science and Technology A*, 16(2):391–403, March/April 1979.
- [24] T.J. Dalton. *Pattern Dependencies in the Plasma Etching of Polysilicon*. Ph.D. Dissertation, Massachusetts Institute of Technology, 1994.
- [25] R.C. Dorf. *Modern Control Systems*. Addison-Wesley, 1989.
- [26] J. C. Doyle and G. Stein. Multivariable feedback design: Concepts for classical/modern synthesis. *IEEE Transactions on Automatic Control*, 26(1):4–16, February 1981.
- [27] D. Edelson and D.L. Flamm. Computer simulation of a CF₄ plasma etching silicon. *Journal of Applied Physics*, 56(5):1522–1531, September 1984.
- [28] T.F. Edgar. Model-based control of rapid thermal processes. In *Extended Abstracts: 187th Meeting of the Electrochemical Society*, page 198, May 1995.

- [29] M. Elta, H. Etemad, J.S. Freudenberg, M.D. Giles, J.W. Grizzle, P.T. Kabamba, P.P. Khargonekar, S. Lafortune, S.M. Meerkov, J.R. Moyne, B.A. Rashap, D. Teneketzis, and F.L. Terry, Jr. Applications of real-time feedback control to semiconductor manufacturing: Reactive ion etching. In *Proceedings of the 1993 American Controls Conference*, pages 2990–2995, June 1993.
- [30] M. Elta, J. Fournier, J.S. Freudenberg, M.D. Giles, J.W. Grizzle, P.T. Kabamba, P.P. Khargonekar, S. Lafortune, S.M. Meerkov, B.A. Rashap, F. L. Terry, Jr., and T. Vincent. Real-time feedback control of reactive ion etching. In *Proceedings of the 1993 SPIE Symposium on Microelectronic Processing*, pages 438–451, September 1993.
- [31] T.H. Fedynyshyn, G.W. Gryniewich, and B.A. Chen T.P. Ma. The effect of metal masks on the plasma etch rate of silicon. *Journal of the Electrochemical Society*, 136(6):1799–1804, June 1989.
- [32] T.H. Fedynyshyn, G.W. Gryniewich, and R.H. Dumas. Mask dependent etch rates: III. the effect of a silver etch masking on the plasma etch rate of silicon. *Journal of the Electrochemical Society*, 135(1):228–269, January 1988.
- [33] T.H. Fedynyshyn, G.W. Gryniewich, T.B. Hook, M.D. Liu, and T.P. Ma. The effect of aluminum vs. photoresist masking on the etching rates of silicon and silicon dioxide in CF_4/O_2 plasmas. *Journal of the Electrochemical Society*, 134(1):206–209, January 1987.
- [34] T.H. Fedynyshyn, G.W. Gryniewich, and T.P. Ma. Mask dependent etch rates: II. The effect of aluminum vs. photoresist masking on the etching rates of silicon and silicon dioxide in CF_4/O_2 plasmas. *Journal of the Electrochemical Society*, 134(10):2580–2585, October 1987.
- [35] D.L. Flamm and V.M. Donnelly. The design of plasma etchants. *Plasma Chemistry and Plasma Processing*, 1(4):317–363, December 1981.
- [36] J.P. Fournier, M.L. Passow, T.J. Cotler, and M.E. Elta. A solution for pressure variations in vacuum process tools due to pressure regulator fluctuations. *Journal of Vacuum Science and Technology A*, 9(2):358–359, March/April 1991.
- [37] J.S. Freudenberg, J.W. Grizzle, and B.A. Rashap. A feedback limitation of decentralized controllers for tito systems, with application to a reactive ion etcher. In *Proceedings of the 33rd IEEE Conference on Decision and Control*, pages 2312–2317, December 1994.
- [38] U. Gerlach-Meyer, J.W. Coburn, and E. Kay. Ion-enhanced gas-surface chemistry: the influence of the mass of the incident ion. *Surface Science*, 103:177–188, 1981.
- [39] R. Gottscho and V. Donnelly. Optical emission actinometry and spectral line shapes in rf glow discharges. *Journal of Applied Physics*, 56(2):245–250, July 1984.
- [40] A. Grace, A.J. Laub, J.N. Little, and C.M. Thompson. *Control System Toolbox: For Use with MATLAB*. The MathWorks, 1992.
- [41] D.B. Graves. Plasma processing in microelectronics manufacturing. *AICHE Journal*, 35(1):1–29, January 1989.

- [42] D.B. Graves. Plasma processing. *IEEE Transactions on Plasma Science*, 22(1):31–42, February 1994.
- [43] D.C. Gray, I. Tepermeister, and H.H. Sawin. Phenomenological modeling of ion-enhanced surface kinetics in fluorine-based plasma etching. *Journal of Vacuum Science and Technology B*, 11(4):1243–1257, July/August 1993.
- [44] A. Grill. *Cold Plasma in Materials Fabrication: From Fundamentals to Applications*. IEEE Press, 1994.
- [45] D.S. Grimard. *Utilizing Diffraction for Real-Time In Situ Wafer Monitoring*. Ph.D. Dissertation, University of Michigan, 1990.
- [46] J.W. Grizzle, M.E. Elta, J.S. Freudenberg, P.P. Khargonekar, and F.L. Terry, Jr. Improving rie process robustness via real-time feedback control. In *Extended Abstracts: 187th Meeting of the Electrochemical Society*, pages 199–200, May 1995.
- [47] P.D. Hanish, J.W. Grizzle, M.D. Giles, and F.L. Terry, Jr. A model-based technique for real-time estimation of absolute fluorine concentration in a CF₄/Ar plasma. *Journal of Vacuum Science and Technology A*, 13(3):1802–1807, May/June 1995.
- [48] W.R. Harshbarger, R.A. Porter, T.A. Miller, and P. Norton. A study of the optical emission from an rf plasma during semiconductor etching. *Applied Spectroscopy*, 31(3):201–207, March 1977.
- [49] O. S. Heavens. *Optical Properties of Thin Solid Films*. Dover Publications, 1965.
- [50] E. Hecht. *Optics*. Addison-Wesley, 1987.
- [51] J.S. Herman, T.E. Benson, O.D. Patterson, C.Y. Chen, A.T. Demos, P.P. Khargonekar, F.L. Terry, Jr., and M.E. Elta. Real-time control of reactive ion etching of amorphous silicon for thin film transistor applications. In *Proceedings of the 186th Meeting of the Electrochemical Society*, October 1994.
- [52] N. Hershkowitz. How does the potential get from a to b in a plasma? *IEEE Transactions on Plasma Science*, 22(1):11–21, February 1994.
- [53] W. J. Hill and W. G. Hunter. A review of response surface methodology: A literature survey. *Technometrics*, 8(4):571–590, November 1966.
- [54] R.A. Horn and C.R. Johnson. *Matrix Analysis*. Cambridge University Press, 1985.
- [55] P. Horowitz and W. Hill. *The Art of Electronics*. Cambridge University Press, 1989.
- [56] I. H. Hutchinson. *Principles of Plasma Diagnostics*. Cambridge University Press, 1987.
- [57] M.W. Jenkins, M.T. Mocella, K.D. Allen, and H.H. Sawin. The modeling of plasma etching processes using response surface methodologies. *Solid State Technology*, 29(4):175–182, April 1986.
- [58] J. Jenq, J. Ding, J.W. Taylor, and N. Hershkowitz. Absolute fluorine concentrations in RIE and ECR CF₄ plasmas measured by actinometry. *Plasma Sources for Science and Technology*, 3:154–161, 1994.

- [59] R.E. Jewett, P.I. Hagouel, A.R. Neureuther, and T. van Duzer. Line-profile resist development simulation techniques. *Polymer Engineering and Science*, 17(6):381–384, June 1977.
- [60] T. Kailath. *Linear Systems*. Prentice-Hall, 1980.
- [61] M. Kimizuka and K. Hirata. Pattern profile control of polysilicon etching. *Journal of Vacuum Science and Technology B*, 3(1):16–19, January/February 1985.
- [62] T.J. Knight, X. Cheng, D.W. Greve, B.H. Krogh, and M.A. Gibson. Multivariable control of plasma enhanced chemical vapor deposition using real-time mass spectroscopy. In *Proceeding of the Thirty-Second Annual Allerton Conference on Communication, Control, and Computing*, pages 765–773, September 1994.
- [63] H.R. Koenig and L.I. Maissel. Application of rf discharges to sputtering. *IBM Journal of research and development*, 14(2):168–171, March 1970.
- [64] M.J. Kushner. Monte-carlo simulation of electron properties in rf parallel plate capacitively coupled discharges. *Journal of Applied Physics*, 54(9):4958–4965, September 1983.
- [65] H.H. Lee. *Fundamentals of Microelectronic Processing*. McGraw-Hill, 1990.
- [66] Y.H. Lee and M. Chen. Silicon etching mechanisms and anisotropy in $\text{CF}_4 + \text{O}_2$ plasma. *Journal of Applied Physics*, 54(10):5966–5973, October 1983.
- [67] M.A. Lieberman and A.J. Lichtenberg. *Principles of Plasma Discharges and Materials Processing*. John Wiley & Sons, 1994.
- [68] L. Ljung. *System Identification Toolbox: For Use with MATLAB*. The MathWorks, 1991.
- [69] L. Ljung. *System Identification: Theory for the User*. Prentice-Hall, 1987.
- [70] D.P. Looze, F. Azad, B. Bernstein, and T. Collins. Control analysis and design for Czochralski growth of GaAs. In *Proceeding of the Thirty-Second Annual Allerton Conference on Communication, Control, and Computing*, pages 794–803, September 1994.
- [71] D.P. Looze, F. Azad, B. Bernstein, and T. Collins. Modeling and identification of the liquid encapsulated Czochralski GaAs process for control. *Journal of Crystal Growth*, 148(1-2):79–95, 1995.
- [72] D.M. Manos and D.L. Flamm, editors. *Plasma Etching*. Academic Press, 1989.
- [73] The Mathworks. *Simulink User's Guide*, 1993.
- [74] J.L. Mauer, J.S. Logan, L.B. Zielinski, and G.C. Schwartz. Mechanism of silicon etching by a CF_4 plasma. *Journal of Vacuum Science and Technology*, 15(5):1734–1738, September/October 1978.
- [75] K.J. McLaughlin. *Development of techniques for real-time monitoring and control in plasma etching*. Ph.D. Dissertation, University of Texas at Austin, 1989.

- [76] K.J. McLaughlin, S.W. Butler, T.F. Edgar, and I. Trachtenberg. Development of techniques for real-time monitoring and control in plasma etching: I. Response surface modeling of CF_4/O_2 and CF_4/H_2 etching of silicon and silicon dioxide. *Journal of the Electrochemical Society*, 138:789–799, March 1991.
- [77] R.H. Middleton and G.C. Goodwin. *Digital Control and Estimation: A Unified Approach*. Prentice Hall, 1990.
- [78] M.M Millard and E. Kay. Difluorocarbene emission spectra from fluorocarbon plasmas and its relationship to fluorocarbon polymer formation. *Journal of Electrochemical Society*, 129(1):160–165, January 1982.
- [79] C.J. Mogab, A.C. Adams, and D.L. Flamm. Plasma etching of Si and SiO_2 - The effect of oxygen additions to CF_4 plasma. *J. Appl. Phys.*, 49(7):3796–3803, July 1978.
- [80] T.M. Morris, D.S. Grimard, C.S. Shu, F.L. Terry, Jr., M.E. Elta, and R.C. Jain. Utilizing diffraction imaging for non destructive wafer topography measurements. In *Proceedings of the 1993 SPIE Symposium on Integrated Circuit Metrology, Inspection, and Process Control*, pages 27–32, March 1993.
- [81] M.R. Murnane, C.J. Raymond, S.L. Prins, S.S.H. Naqvi, and J.R. McNeil. Scatterometry for $0.24 \mu\text{m}$ - $0.70 \mu\text{m}$ developed photoresist metrology. In *Proceedings of the 1995 SPIE Symposium on Integrated Circuit Metrology, Inspection, and Process Control*, pages 427–436, February 1995.
- [82] N. Mutsukura, Y. Fukasawa, Y. Machi, and T. Kubota. Diagnostics and control of radio-frequency discharge. *Journal of Applied Physics*, 72:3126–3130, December 1994.
- [83] National Research Council. *Plasma Processing of Materials: Scientific Opportunities and Technology Challenges*, 1991.
- [84] M.L. Passow. *Microwave, RF and Hybrid Reactor Generated Discharges for Semiconductor Processing*. Ph.D. Dissertation, University of Michigan, 1991.
- [85] I.C. Plumb and K.R. Ryan. A model of the chemical processes occurring in CF_4/O_2 discharges used in plasma etching. *Plasma Chemistry and Plasma Processing*, 6(3):205–230, September 1986.
- [86] B.A. Rashap, M. Elta, H. Etemad, J.S. Freudenberg, J.P. Fournier, M.D. Giles, J.W. Grizzle, P.T. Kabamba, P.P. Khargonekar, S. Lafortune, J.R. Moyne, D. Teneketzis, and F.L. Terry, Jr. Control of semiconductor manufacturing equipment: Real-time feedback control of a reactive ion etcher. *IEEE Transactions on Semiconductor Manufacturing*, 8(3):286–297, August 1995.
- [87] B.A. Rashap, J.S. Freudenberg, and M. Elta. Real-time feedback for sidewall profile control in reactive ion etching. *Journal of Vacuum Science and Technology A*, 13(3):1792–1796, May/June 1995.
- [88] B.A. Rashap, P.P. Khargonekar, M.E. Elta, J.S. Freudenberg, and F.L. Terry, Jr. Real-time control of reactive ion etching: Identification and disturbance rejection. In *Proc. 1993 IEEE Conference on Decision and Control*, pages 3379–3385, December 1993.

- [89] A.D. Richards, B.E. Thompson, K.D. Allen, and H.H. Sawin. Atomic chlorine concentration measurements in a plasma reactor. I. A comparison of infrared absorption and optical emission actinometry. *Journal of Applied Physics*, 3(1):792–807, August 1987.
- [90] K.R. Ryan and I.C. Plumb. Kinetics of the reactions of CF_3 with $\text{O}({}^3\text{P})$ and O_2 at 295k. *The Journal of Physical Chemistry*, 86(24):4678–4683, 1982.
- [91] K.R. Ryan and I.C. Plumb. Gas-phase of the reactions of CF_2 with $\text{O}({}^3\text{P})$ to produce COF: Their significance in plasma processing. *Plasma Chemistry and Plasma Processing*, 4(4):271–284, December 1984.
- [92] K.R. Ryan and I.C. Plumb. A model for the etching of Si in CF_4 plasmas: Comparison with experimental measurements. *Plasma Chemistry and Plasma Processing*, 6(3):231–245, 1986.
- [93] H.H. Sawin. Challenges in dry etching: uniformity, selectivity, pattern dependencies, damage, and cleaning. *Microelectronic Engineering*, 23:15–21, 1994.
- [94] C. Schaper, Y. Cho, and T. Kailath. Low-order modeling and dynamic characterization of rapid thermal processing. *Applied Physics A*, 54:317–326, April 1992.
- [95] C. Schaper, M. Moslehi, K. Saraswat, and T. Kailath. Control of MMST RTP: Repeatability, uniformity, and integration for flexible manufacturing. *IEEE Transactions on Semiconductor Manufacturing*, 7(2):202–219, May 1994.
- [96] C. Schaper, M. Moslehi, K. Saraswat, and T. Kailath. Modeling, identification, and control of rapid thermal processing systems. *Journal of the Electrochemical Society*, 141(11):3200–3209, November 1994.
- [97] Semiconductor Industry Association. *The National Technology Roadmap for Semiconductors*, 1994.
- [98] T. Soderstrom and P. Stoica. *System Identification*. Prentice Hall, 1989.
- [99] M. Spak, D. Mammato, S. Jain, and D. Durham. Mechanism and lithographic evaluation of image reversal in AZ 5214 photoresist. In *Proceedings of the Seventh International Technical Conference on Photopolymers*.
- [100] A.R. Striganov and N.S. Sventitskii. *Tables of Spectral Lines of Neutral and Ionized Atoms*. IFI/Plenum, 1968.
- [101] J.D. Stuber, I. Trachtenberg, T.F. Edgar, J.K. Elliott, and T. Breedijk. Model-based control of rapid thermal processes. In *Proceedings of the 33rd Conference on Decision and Control*, pages 79–85, December 1994.
- [102] S.M. Sze, editor. *VLSI Technology*. McGraw-Hill, 1983.
- [103] C.M. Thompson and L Shure. *Image Processing Toolbox: For Use with MATLAB*. The MathWorks, 1993.
- [104] Y.Y. Tu, T.J. Chuang, and H.F. Winters. Chemical sputtering of fluorinated silicon. *Physical Review B*, 23(2):823–835, January 1981.

- [105] T.L. Vincent, P.P. Khargonekar, and F.L. Terry, Jr. A fast algorithm for real time etch rate measurement using single or multiple wavelength reflectometry. *Submitted to 1995 Materials Research Society Fall Meeting*, 1995.
- [106] T.L. Vincent, P.P. Khargonekar, B.A. Rashap, F.L. Terry, Jr., and M.E. Elta. Non-linear system identification and control of a reactive ion etcher. In *Proceedings of the 1994 American Control Conference*, pages 902–905, 1994.
- [107] H.F. Winters and J.W. Coburn. Surface science aspects of etching reactions. *Surface Science Reports*, 14(4-6):165–269, February 1992.
- [108] S. Wolf. *Silicon Processing for the VLSI Era: Volume 2 - Process Integration*. Lattice Press, 1990.
- [109] S. Wolf and R.N. Tauber. *Silicon Processing for the VLSI Era: Volume 1 - Process Technology*. Lattice Press, 1986.
- [110] M.J. Zucrow. *Gas Dynamics*. John Wiley & Sons, 1976.